PARSEC-SCALE STRUCTURE IN THE NUCLEI OF DOUBLE-LOBED RADIO QUASARS

Thesis by

David Hans Hough

In Partial Fulfillment of the Requirements
for the Degree of Doctor of Philosophy

California Institute of Technology
Pasadena, California
1986
(Submitted March 31, 1986)

© 1986

David Hans Hough

All Rights Reserved

To my parents

Acknowledgments

It is a great pleasure to thank Tony Readhead for suggesting the topic of this thesis and serving as my advisor. There is no doubt that I would have been unable to endure five years of graduate study without his frequent injections of enthusiasm.

I am grateful to Marshall Cohen for words of wisdom at various stages during my stay at Caltech, and for funding my first vacation to Europe virtually without hesitation.

Roger Blandford and Maarten Schmidt have expressed interest and offered support at key times.

It is not possible to list everyone who has added something special to my time at Caltech. But I am particularly indebted to Fred, Marcus, and Toni for engaging conversations and enlightenment on a wide range of matters. Of course, I have also enjoyed the company of many of the staff, postdocs, and my fellow students.

The backpacking trips organized by Helen and George were delightful. Larry was always sure to check that I was getting into trouble. I thank Jill for being the person most appreciative of my pumpkin head. JoAnn, Leona, and Gloria have been very kind and supportive.

Charlie, Dayton, Peter, Steve U., and Tim (especially Tim for all his computing assistance!) have offered much friendly advice.

I shall long remember sharing the lower levels of Robinson with Abi, Alain P. No. 1, Alain P. No. 2 (whose courage, determination, and oblique humor are unsurpassed), Alex, Blaise ("Who's that redhead across the room?"), Bruce, Chris, Chuck, Dean, Don, Fernando, Hai Min, Jim, John, Kevin, Kwok-Wai, Mike, Pawan ("The Calculator"), Rich R., Richard S., Roger, Steve L., and Steve M. (for putting up with my questionable habits).

Erich, Dan, and the whole softball crew helped me to pass many a dreamy summer afternoon as I played out my Phil Niekro fantasies.

I would like to make particular mention of Jay Johovich, to whom I had promised to give a copy of this thesis. I had numerous delightful times shooting the breeze with him at Owens Valley, and I don't think he ever yelled at me once when I called him at home at 3 AM to pull me out of a jam at the telescope. I was greatly saddened to learn of his untimely passing last year.

I am happy to express great thanks to everyone at Owens Valley who has made my observing trips there very pleasant and successful, with special mention for Harry, Mark, and Curt.

The staff at Haystack Observatory is to be thanked for unlimited assistance in scheduling, observing, and data processing. Bob Phillips, Alan Rogers, Alan Whitney, and Roger Cappallo were always ready and willing to help.

Richard Porcas at Effelsberg and Franco Mantovani at Medicina made sure that I always got my transatlantic baselines. The staffs of the National Radio Astronomy Observatory (Green Bank) and the George R. Agassiz Station

of Harvard College Observatory (Fort Davis), both working with the support of the National Science Foundation, have kindly supported the observations.

Special thanks go to J. Wardle, R. Laing, A. Foley, R. Davis, C. Lonsdale, I. Morison, and D. Shone for permission to include various radio maps. I. Browne, P. Scheuer, and P. Wilkinson offered many useful comments on Chapter 1. J. Marcaide provided software support at the start of this project. G. Seielstad helped lead a largely successful investigation to unravel the calibration history at Green Bank. F. Seward provided Einstein Observatory X-ray data.

I am grateful to the California Institute of Technology, the National Science Foundation, Haystack Observatory, and the Max-Planck- Institut für Radioastronomie for financial support.

The staff of the Young Health Center has tended to my needs during my entire stay at Caltech with great care and cheer.

Bob C. Goode first inspired me to study physics, and H. Terry Fortune encouraged me to keep on going. I thank Jack Burns for introducing me to radio astronomy in spectacular fashion at the Very Large Array.

I would never have been able to pursue study in astronomy if it had not been for my parents. I cannot stress enough how much I valued their willingness to support me in whatever I chose to do, as long as it kept me out of trouble! I wish my Dad could still be here to see how it

has all turned out. To my Mom, thanks for never complaining about me moving to California, even though I said shortly before deciding to come here that I'd probably never do it!

Finally, I would like to say a very special thanks to someone who has been supportive and understanding during the trying times of completing this thesis. Without her love and reassurance in these past few months, I really doubt that I could have finished the task. Gina, I thank you with all my heart.

P.S.: To the unknown person responsible for the still unsolved Famous Amos Cookie mystery, THANK YOU!

ABSTRACT

A complete sample of double-lobed quasars is defined, which is believed to be randomly oriented and which contains many objects with central components accessible to very-long-baseline interferometry (VLBI). The purpose of defining the sample in this way is to facilitate tests of physical models proposed to explain both the compact and extended structures in extragalactic radio sources. Statistical studies of the properties of these objects on the >~ kiloparsec scale are consistent with the assumption of random orientations and the simple relativistic beaming theory.

The central components of six double-lobed quasars have been mapped at high resolution and high sensitivity with VLBI. Each object exhibits a double or extended structure on the the ~parsec scale. This structure can be interpreted as a "core-jet," the same morphology found in the dominant cores of powerful flat-spectrum sources, thus indicating a relation between the two classes of compact radio source. The presumed VLBI jets are all fairly well aligned with >~kiloparsec-scale, one-sided jets. The fact that the VLBI and large-scale jets always lie on the same side of the compact core suggests the same cause for the asymmetric structure on both scales.

The central components of 3C245 and 3C263 have been mapped at three epochs. We find superluminal expansion in

3C263 with an apparent velocity of ~1.5c, and argue that there is evidence that 3C245 will also be found to be superluminal. These results are consistent with the simple beaming theory. It is thus clear that we will be able to measure component motion in many of these objects, which will permit us to distinguish among alternative theories of parsec-scale structure and motion.

The future study of these compact central components will benefit greatly from the increased resolution afforded by both higher frequency, ground-based VLBI and VLBI using a radio telescope in Earth orbit.

TABLE OF CONTENTS

INTRODUCTION

One of the outstanding problems in astrophysics is that of understanding the mechanism which powers active galactic nuclei and quasars. The only present means of directly probing the most compact regions in these objects on the parsec scale is by very-long-baseline interferometry (VLBI). By our studying the physics of the compact radio sources associated with the "central engine," it should be possible to place constraints on the nature of the nuclear activity, which must originate in the vicinity of a supermassive object.

A simple physical model which can account for the "core-jet" morphology and superluminal motion in many compact sources is the relativistic beaming model (Scheuer and Readhead 1979; Blandford and Königl 1979). While beaming clearly plays some part in these objects, observational selection effects have hindered rigorous, quantitative tests of its precise role. A sample of objects free of orientation bias, however, is ideal for tests of beaming, a theory for which the observed effects are strongly dependent upon orientation.

It is with these thoughts in mind that we define a complete sample of double-lobed quasars in Chapter 1. Statistical tests are conducted to check for consistency with the beaming hypothesis. Predictions of the simple beaming model testable by VLBI are discussed. In Chapter 2, Mark III VLBI observations (Rogers, et al. 1983) of the central components of six double-lobed quasars are presented. The parsec-scale morphology, and its relation to $\gtrsim$kiloparsec-scale structure, are described. In Chapter 3, multiple-epoch VLBI maps of the central components in 3C245 and 3C263 are presented. Apparent superluminal expansion is detected in 3C263, and 3C245 is most probably also superluminal. Finally, in Chapter 4, estimates are made of the physical conditions in the compact VLBI components.

References

Blandford, R.D., and Königl, A. 1979, *Ap.J.*, **232**, 34.

Rogers, A.E.E., et al. 1983, *Science*, **219**, 51.

Scheuer, P.A.G., and Readhead, A.C.S. 1979, *Nature*, **277**, 182.

CHAPTER 1

STATISTICS OF A COMPLETE SAMPLE OF DOUBLE-LOBED QUASARS FOR VLBI OBSERVATIONS

Summary

A complete, flux density-limited sample of double-lobed radio quasars with central components (CCs) bright enough to be mapped with the Mark III VLBI system is defined. Statistical tests performed on the sample are consistent with the assumption of random source orientations and the simple relativistic beaming model for the CCs. There is marginal evidence that ~20 per cent of the total CC radio emission may be isotropic.

I. Introduction

In order to test physical models which have been proposed to explain both the compact and extended structures of extragalactic radio sources, a study of the central components (CCs) of a complete sample of double-lobed radio quasars by very-long-baseline interferometry (VLBI) has been undertaken. A "double-lobed" quasar is defined here as one in which two roughly symmetrical lobes are found straddling the optical object. This definition therefore includes not only "classical doubles," but also triple sources. A sample has been chosen for which selection effects are minimal and which contains a reasonable number of objects that can be mapped with existing VLBI networks. Thus, the relationships between the nuclear and extended structures can be established for these quasars, and it should be possible to determine the role of relativistic beaming (Scheuer and Readhead 1979; Blandford and Königl 1979; Orr and Browne 1982) in these objects.

Most previous studies of double-lobed extragalactic objects have concentrated on selected objects rather than complete samples. Linfield (1981) has mapped the nuclear radio structure of four radio galaxies. Porcas (1981) was the first to observe superluminal motion in the CC of a double-lobed quasar, 3C179. Barthel (1984) has made short observations of a number of extended quasar CCs selected from the Burbidge, Crowne, and Smith (1977) compilation.

Zensus and Porcas (1984) have worked on a complete sample (the Jodrell Bank 966 MHz survey) similar to the one we are studying, and these two studies complement each other in view of the small number of objects in both samples. The present work is based on a complete sample of double-lobed quasars believed to be free from orientation bias (unlike other large VLBI surveys like that of Pearson and Readhead (1984)). The statistics of apparent transverse velocities, overall sizes, relative brightness of cores and outer components, and overall morphology in this sample will provide a crucial test of simple relativistic beaming models.

There is clearly a connection between the small- and large-scale one-sided jets in extragalactic radio sources (e.g., Jones, et al. 1986), since in all cases (about twenty thus far) in which there is both a nuclear and a large-scale jet, the two jets are on the same side of the compact core in the nucleus (see Chapter 2). This shows that the small- and large-scale asymmetries have the same cause. Thus, relativistic beaming could be responsible for the asymmetries on both scales.

In this chapter, a carefully selected complete sample of sources is defined. We perform a statistical analysis of information from conventional interferometry to check for consistency with the beaming hypothesis in the central components. Such analyses have been made in the past by Kapahi and Saikia (1982; hereafter KS) and Orr and Browne (1982; hereafter OB) on larger samples. Nevertheless, it is worth performing the analysis on this sample since it is complete (not true of KS), and since we study the details of correlations of various observable properties (not done by OB).

For the future an intensive study of this sample is planned to the limits of present VLBI capabilities, which will eventually involve obtaining multifrequency VLBI maps with the VLBA. In addition, extremely sensitive observations with the VLA will be performed on all the objects. These observations will provide a large sample for direct tests of beaming in the CCs by looking for component motion, and also for thorough statistical tests of beaming in the outer jets and lobes.

II. The Selection of the Sample of Quasars

A. The Parent Sample

Relativistic beaming has been invoked to explain superluminal motion, "core-jet" morphology, and other features of strong, compact extragalactic radio sources (Readhead et al., 1978). A strong observational selection effect may exist, however, due to Doppler boosting. If the bulk flow is confined to a narrow range of angles ($< 1/\gamma$, where γ is the bulk Lorentz factor), then sources with their axes at a small angle, θ, to the line-of-sight are strongly favored. Since, on the beaming model, many of the observable quantities depend upon orientation, a sample is required for which the distribution in θ is known.

A sample of sources with randomly oriented axes is the ideal starting point for our study. We have therefore selected a complete low-frequency, flux density-limited sample of double-lobed quasars in which the outer, presumably unbeamed, lobes dominate. The parent sample is the complete sample of 173 3CR sources defined in Jenkins, Pooley, and Riley (1977), and revised by Laing, Riley, and Longair (1983). This parent sample is chosen for the following reasons:

(1) the optical identifications are nearly complete;

(2) the survey was made at a low frequency (178 MHz), and thus the sample contains many steep-spectrum, double-lobed sources which are thought to be free of orientation bias selection effects;

(3) high-quality 5 GHz maps of all the objects in the sample have been made with the Cambridge 5 km telescope and/or the VLA;

(4) it is very well studied, so that in general there is more information about these objects in other wavebands than there is for other samples of radio sources.

There are forty-three quasars in this parent sample (see Table 1). We select quasars because they have brighter CCs, on average, than do radio galaxies. Thus, a larger fraction of quasars in a complete sample can be studied by VLBI. Furthermore, no systematic study of the CCs of a complete sample of quasars has yet been done.

In Table 1, the columns are as follows:

(1) 3C designation;

(2) morphological class, as described in notes to the table;

(3) redshift, z;

(4) visual magnitude, m_V;

(5) CC flux density at 5 GHz, S_{CC}, in mJy;

(6) total flux density at 5 GHz, S_T, in mJy;

(7) largest angular size, ψ, in arcseconds, defined along the largest axis through the source;

(8) references, with key in notes to table.

B. The Complete Sample of Double-lobed Quasars

There are forty-three quasars in the parent sample defined above, of which we classify twenty-six as double-lobed quasars (see below). Of these twenty-six objects, seventeen have bright enough central components for mapping with VLBI. As the brighter CCs of the compact triples are already being mapped by others, we have selected the eight brightest CCs in "classical doubles" for VLBI study here. We shall now describe the details of the selection of the sample of double-lobed quasars and a complete VLBI subsample.

There are twenty-one quasars with clear double-lobed structure, i.e., "classical doubles." The source 3C245 was originally classified as a D2 object (Miley 1971), but it was later found to have a weak third component (Laing 1981a), and has therefore been included. Five objects with largest angular size <~5" (3C43, 3C190, 3C191, 3C216, and 3C309.1, Fanti, et al. 1985; Pearson, Perley, and Readhead 1985) could be extended double-lobed sources seen nearly end-on, or simply of small intrinsic linear size. Since it is not clear, on the basis of morphology alone, if these compact triples belong to a class of object physically distinct from the "classical doubles," we have done separate analyses with and without these objects in the sample (see Section III). When these compact triples (CTs) are included in the sample of double-lobed sources, the total number of objects is twenty-six (see Table 2).

In Table 2, the columns are as follows:

(1) 3C designation (In cases where the individual spectra of the CC and outer lobes are unknown, a note explains spectral requirements which would place each source in the complete sample);

(2) ratio of S_{CC} to $S_{outer}=S_T-S_{CC}$ at 5 GHz emitted, R;

(3) projected linear size, L, in kpc;

(4) curvature, defined as the supplement of the angle between the lines joining the peaks of the outer emission to the CC, C, in degrees;

(5) large-scale jet?

The twenty-six sources in this group all meet the criterion of S > 10 Jy at 178 MHz in the outer, steep-spectrum components, with the possible exception of 3C43 (see Section III, part D). In addition, the large-scale jets contribute too little flux density to affect this selection, with the possible exceptions of 3C207 and 3C245. We assumed that any beaming of outer lobe "hot spots" is insignificant. Therefore, these objects should form a complete sample with random orientations.

The other seventeen quasars in the original parent sample of forty-three objects have been excluded from the double-lobed sample for the following reasons:

(1) Ten objects with $\psi <\sim 5''$ do not look like double-lobed objects seen in projection. Eight of these (3C48, 3C138, 3C147, 3C286, 3C287, 3C343, 3C380, and 3C454) have steep spectra which turn over in the range 10 MHz-300 MHz, unlike the typical double-lobed objects. These compact, steep-spectrum sources may be intrinsically different to the extended doubles (e.g., 3C380, Wilkinson 1985). Two sources (3C345 and 3C454.3) have flat spectra ($\alpha < 0.2$) and are excluded because the flux density in the extended steep-spectrum emission is probably below the sample cutoff. Such objects are considered as end-on double sources in the OB "unified scheme," however, and therefore we do consider them in estimates of the bulk Lorentz factor below (see Section III).

(2) Three objects (3C186, 3C254, and 3C455) have peculiar morphology. A distant component associated with the core of 3C186 may or may not be physically related; Cawthorne (1984) has resolved the core with the VLA and found it to be a compact triple. Recent observations by Owen and Puschell (1984) have demonstrated the existence of a weak CC far off center in 3C254, making this object most unusual. 3C455 has

not been observed at high enough resolution and sensitivity to distinguish fully its structure, although Schilizzi, Kapahi, and Neff (1982) suggest that it should be classified as a D2 object.

(3) 3C196 has a morphology which suggests it may be a precessing source (Lonsdale and Morison 1983). Strong precession effects will confuse tests of beaming (e.g., the small- to large-scale jet apparent curvature), and so this object has been excluded.

(4) Three objects identified as quasars have no spectroscopic confirmation (3C14, 3C325, and 4C16.49). (We intend to make Palomar 5-meter telescope observations to confirm the identifications.) Even if these objects should be confirmed as QSOs, it is likely that they will all be found to lie at high redshift, and their omission will not affect the bulk of the analysis below, which deals predominantly with objects at $z < 1.3$ (see Section III).

In the sample of twenty-six double-lobed quasars, there are seventeen with $S_{CC} > 30$ mJy at 5 GHz. This is the limiting flux density which can be mapped with reasonable dynamic range (say ~20:1) with existing or planned VLBI arrays. The central components of all seventeen of these quasars will therefore eventually be mapped by VLBI. Given the present limits of sensitivity of VLBI observations, the bias introduced by selecting relatively strong CCs is unavoidable. This can be allowed for in terms of specific beaming models (see Section IV). Most of the objects are at $z < 1$, which makes them suitable to monitor for superluminal motion.

Of these seventeen objects, four have been mapped by others (see Table 3). There are eight "classical double" quasars--3C207, 3C212, 3C245, 3C249.1, 3C263, 3C270.1, 3C275.1, and 3C334--with $S_{CC} > 75$ mJy at 5 GHz. We select these as our prime sample for study, since they are all well-defined "classical doubles" and are much easier to map with VLBI than the fainter objects.

The best combination of resolution and sensitivity for studying this group is given by the VLBI network at 10.7 GHz using the Mark III recording system (Rogers, et al. 1983). We choose the highest practical frequency for studying a reasonably large sample in order to increase our chances of measuring proper motion in these objects. Further discussion of the VLBI study of these specific objects begins in Chapter 2.

C. Source Parameters

Before proceeding with the analysis below, several points should be made here about the body of data in Table 2. The measure of CC strength used here is the ratio, R, defined as the ratio of CC flux density to that of the outer emission (i.e., all emission except the CC) at an emitted frequency of 5 GHz. As pointed out by Hine and Scheuer (1980), normalizing the CC emission to that of the outer structure reduces the scatter due to the correlation of CC power and extended power (Hine and Longair 1979). R depends on frequency, and we chose a selection frequency of 5 GHz because there are high-quality Cambridge 5 km telescope maps or VLA maps of most of the objects in our sample at 5 GHz. For the purpose of analysis, R has been set equal to the quoted upper limit in the cases where no CC has yet been detected. Some of the CCs in the sample are known to be variable (see Chapter 2), but long-term monitoring of most of them has been very irregular. The flux densities used to derive R were measured at random times, and some may therefore represent extreme values.

In order to derive R from the observed flux density ratio, a K-correction $(1+z)^{\Delta\alpha}$ has been applied, where $\Delta\alpha$ is the difference between the spectral indices of the CC and extended emission, respectively ($S_\nu \propto \nu^{-\alpha}$). The CC spectra are not well known, and the values used here are sometimes poorly determined. A value of $\alpha=0.2$ has often been assumed, since this is about the average value for "classical doubles" in this sample for which the CC spectra are well known.

It is not clear what spectral index to apply to the CC for the five compact triples in Table 2 (3C43, 3C190, 3C191, 3C216, and 3C309.1). 3C309.1 has a steep-spectrum CC ($\alpha=0.7$), and we have assumed that 3C43 also has a similar spectral index. We have further assumed both $\alpha=0.2$ and 0.7 for 3C190, 3C191, and 3C216 in calculating R.

The ~1" CC flux density and spectrum in several sources may be contaminated by some large-scale jet structure. We checked for this by examining the available maps, and estimate that confusing contributions from the jets are generally < 10 per cent of the CC flux density.

The curvature, C, is defined as the supplement of the angle between the lines joining the outer lobe peaks to the CC. Sometimes this requires choosing a mean position between two comparable "hot spots" in the same lobe. Also, C is not defined for the sources without a detected radio CC; this is because a positional offset of the optical identification from the unobserved radio CC can lead, especially in objects of small angular size, to large errors in C. The curvature is always determined through the outermost compact features. For 3C190, 3C249.1, and 3C334, we ignored outer, diffuse, off-axis emission. 3C215 is very much distorted, and the mean C given should be treated with caution (see Table 1 for references to large-scale maps).

Throughout these calculations we assumed an Einstein-deSitter universe with H_o=75 km/sec/Mpc and q_o=0.5.

III. Statistics of Beaming for the Complete Sample

A statistical analysis of the complete sample of twenty-six double-lobed quasars is presented in this section. Before launching into our own analysis it is useful to mention the findings of KS in their study of an incomplete sample. These authors studied a sample of 78 double-lobed quasars. They investigated correlations between various physical properties and concluded that the statistics of their sample are consistent with relativistic beaming in the CCs, but with little constraint on the bulk Lorentz factor.

There are some minor technical differences between the analysis here and that of KS. They applied the Kolmogorov-Smirnov two-sample test to obtain confidence levels for the correlations, whereas here the linear-correlation coefficient test is employed. KS used the fraction of the total flux density in the CC, f_c, at 8 GHz emitted as a measure of CC strength; here, the ratio of CC to outer flux density, R, at 5 GHz emitted is used ($f_c = R/(1+R)$).

In both analyses, CC strength, normalized to the extended emission, is used as a measure of orientation, Θ, assuming the simple beaming model. While there may be other effects at work which make CC strength less than ideal as a measure of Θ (see part C.4.a), it is difficult to imagine a better means of estimating source orientation for the purpose of these tests.

A. Statistical Methods

Throughout this analysis, significance levels for correlations are derived simply from linear-correlation coefficient tests. The linear-correlation coefficient, r, and the probability, P, that a value of $\geq$ r would result randomly for two uncorrelated variables with N samples, are listed for all tests in Tables 4, 5, and 6. Only when a significance level of $1-P \geq 0.90$ is reached for at least one of the two trials (with and without the compact triples) on a given pair of observables is the possibility of a true correlation entertained. All data points were given equal weight in these tests, and the probabilities are quoted to the nearest ~0.05.

For comparing observed distributions with predictions of models, we use the chi-square test. $P(\chi^2)$ gives the probability that discrepancies between the observed and predicted distributions could have arisen randomly. Because of the small sample size, these tests have been done with both three and four bins; the re-binning was done as a check that the chi-square results were independent of bin selection. $P(\chi^2)$ was arbitrarily required to be > 0.20 in at least one trial for it to be considered reasonable that the discrepancies between the observed and predicted distributions could have arisen by chance. Probability values are quoted to the nearest ~0.05. Continuous distributions for model predictions were actually calculated assuming closely spaced discrete values of the variable in question.

The results are presented for both the sample of "classical double" quasars and the larger sample of double-lobed quasars, which includes the compact triples (CTs) discussed in Section II.

B. Redshift Dependence

In order to see whether the twenty-six quasars form a uniform sample of objects from a single population, the dependence of physical properties on redshift was first considered. The three key observable quantities to be used in the tests of beaming are the projected linear size, L, the CC strength, R, and the curvature, C. It is desirable to study a sample in which evolutionary effects on any of these physical properties will not confuse tests of random orientation and beaming.

The projected linear size, L, is plotted against redshift in Figure 1. This shows a fairly uniform spread in L out to approximately z=1.3. At higher redshift, there is a distinct drop in L, such that the anti-correlation of L with z over the entire redshift range is highly significant (see Table 4). Legg (1970) and Miley (1971) first noted the decrease in the upper envelope of angular size with redshift. Wardle and Miley (1974) claimed to find the additional effect of a decrease in projected linear size with redshift. Hooley, Longair, and Riley (1978) and Masson (1980), however, argued that there is little or no evolution in physical size for luminous quasars. Instead, they pointed to a possible anti-correlation of luminosity and linear size, which would lead to a smaller range of observed sizes at high redshift for a flux density-limited sample.

Whatever the actual explanation of this effect, the observational fact is that there exists a deficit of large quasars at high redshift in our flux density-limited sample. This drop in the upper envelope of the L-z diagram is visible at roughly the same redshift in the data of Stannard and Neal (1977). Barthel (1984) also noted a deficit of large sources at high redshift, although it is less pronounced and does not appear appreciable until $z > 2$. In order to minimize possible effects of evolution, the sample has been divided into two groups: the "low z" sample, with those objects at $z < 1.3$; and the "high z" sample, with those objects at $z > 1.3$. While the drop in linear size is undoubtedly not as sharp as it appears in Figure 1, this provides a convenient means of dividing the sample into two parts. Further analysis will concentrate on the low z sample, which contains eighteen objects. Tests of the low z sample show no significant correlation of L with z (see Table 5).

The dependence of CC strength, R, on redshift has also been tested. There is only a marginal correlation between R and z for the entire redshift range, and no correlation for the low z sample. KS found no correlation of CC strength with redshift in their larger sample. This is discussed further in parts C.4.b and D below.

A check was made for any correlation of curvature with redshift. There is no evidence for a correlation of C with z for the low z or combined samples from the linear-correlation coefficient tests. This is in agreement with the results of Hintzen, Ulvestad, and Owen (1983), who found no dependence of C on z for a very large, but incomplete, sample.

C. The Low Redshift Sample

From now on we concentrate on this low z group of eighteen objects, for which L, R, and C show no z dependence. Fifteen of these sources are "classical doubles." This group includes the CTs 3C216 and 3C309.1, which may exhibit beaming on the ~kiloparsec scale away from the arcsecond core (Readhead 1986). These two objects are to be noted particularly because they are very compact, and it has not been possible yet to distinguish contributions to the outer flux density from jets versus those from diffuse structures in the compact lobes. However, assuming typical spectral indices for the diffuse portions of the outer lobes (Pearson, Perley, and Readhead 1985), these would be in the sample based on the unbeamed component of their outer emission.

1. Radio Luminosity in the Extended Structure

We have checked the range of radio luminosity in the extended structure for this low z sample. The radio luminosity is calculated using 5 GHz flux densities and assuming power-law spectra between 10 MHz and 100 GHz. Because the sample is flux density-limited, the minimum observed power in the extended structure of course increases with redshift. Coupled with the strong evolution of the comoving density of powerful steep-spectrum sources first noted by Longair (1966) and more recently confirmed in detail by Peacock and Gull (1981), there is naturally a strong correlation of luminosity with redshift in this sample. The spread in radio luminosity is a factor ~30. Fifteen of the sources are luminous Fanaroff and Riley (1974) class II doubles, with the weakest source ~10 times the cutoff (~3 x 10^{26} W/Hz at 178 MHz) between class I and class II. (The other three objects are luminous compact triples.) It is true, however, that the two lowest luminosity objects (3C215 and 3C249.1), which are nearby, show strong deviations from "classical double" structure (Hintzen, Ulvestad, and Owen 1983; Lonsdale and Morison 1983).

2. Luminosity Dependence

A test has been made for any correlation between luminosity and other morphological radio properties in the low z sample. This was done to ensure that the large spread of power in the extended structure, P_e, over a range of ~30 did not introduce any correlations which would confuse tests of beaming. Plots of P_e against R, C, and L show no evidence of luminosity correlations apart from a possible marginal anti-correlation between P_e and L when the CTs are included (see Table 5, Figure 2). The lack of correlation between power and CC strength had been noted earlier by KS; this is discussed further in part C.4.b below. For completeness, it should be mentioned here that disregarding 3C215, $C > 10^o$ occurs only for $P_e > 2 \times 10^{37}$ W, but this is not statistically significant.

The marginal trend for outer lobe power to be anti-correlated with projected linear size could be interesting, since it might indicate that there is some beaming on large scales. Therefore, as mentioned above, high-quality VLA maps of all the objects will be obtained in the future. This will permit an estimate of the contributions to the large-scale emission from jets. An alternative explanation for the P_e-L trend is simply the evolutionary effect in which higher redshift, more luminous objects are smaller. Wardle and Miley (1974) saw no P_e-L anti-correlation, but Stannard and Neal (1977), Hooley, Longair, and Riley (1978), Masson (1980), and Barthel (1984) all suggested a marginal P_e-L anti-correlation.

3. Orientation Tests

The results of these checks of redshift and luminosity dependence affirm the uniformity of the sample for $z < 1.3$. Henceforth we concentrate on tests of source orientation and correlations relevant to beaming for the low z sample. First, we must ascertain whether or not the sample is consistent with random orientations. To begin, consider the distribution of projected linear size, L. The predicted distribution of L for a set of sources of fixed intrinsic linear size, L_{90}, can be calculated from the probability of observing a source at $L = L_{90}\sin\theta$ between L_1 and L_2:

$$P(L_1, L_2) = \cos\theta_2 - \cos\theta_1 \ . \qquad (1)$$

If it is simply assumed that all sources have the same intrinsic linear size L_{90} = 330 kpc (case A), the predicted distribution is in poor agreement with the observed distribution, as expected ($P(\chi^2) < 0.01$ in all cases; see Figure 3). A uniform distribution in L_{90} from 0-330 kpc (case B), however, gives an acceptable fit to the data ($P(\chi^2) = 0.25$ without the CTs, 0.30 with them). Legg (1970) was the first to show that a uniform distribution in L_{90} could explain the L histogram for the larger of the 3C sources. An even better fit is obtained using a continuous distribution of L_{90}, in which the larger values of L_{90} are given more weight (case C); e.g., assigning L_{90}=165-330 kpc twice the weight of L_{90}=0-165 kpc, $P(\chi^2) = 0.50$ without the CTs and 0.25 with them. (It should be noted that in rebinning from four to three bins, $P(\chi^2) > 0.20$ for case C without the CTs, but drops to between 0.10 and 0.20 for the other L_{90} distributions.)

Thus, a plausible distribution of L_{90} gives good agreement between the predicted and observed n vs. L, assuming random orientations. This holds true whether or not the three compact triples (3C190, 3C216, and 3C309.1) are included, although the optimum fit, which favors larger L_{90} sources, is obtained when they are omitted. We note that the lobes are usually well separated from the CC, so that their finite sizes do not significantly blur the definition of the largest angular size.

4. Tests of Beaming in the Central Components

a. Distribution of CC Strength

We next examine the distribution of CC strength, R. On the twin-jet model, the beaming effect on flux density may be calculated from the relation

$$R = \frac{R_{90}}{2}\left\{ [1-\beta\cos\theta]^{-(n+\alpha)} + [1+\beta\cos\theta]^{-(n+\alpha)} \right\}, \qquad (2)$$

where R_{90} is the ratio of CC to outer flux density for the two jets moving at $\theta=90^\circ$, $\gamma=(1-\beta^2)^{-1/2}$ is the bulk Lorentz factor, n=2 for a continuous jet, and α is the spectral index (Scheuer and Readhead 1979, OB). This expression gives the observed R at the same frequency at which the unboosted CC strength would be observed in the comoving frame. This is true, of course, only for very simple, non-evolving models; Lind and Blandford (1985) have clearly demonstrated that it is not possible to make meaningful deductions about the bulk flow velocity without a detailed knowledge of the source structure. However, for the purpose of testing whether or not the observations are at least consistent with the relativistic beaming hypothesis in one of its most elementary forms, the simple twin-jet model will be assumed here.

The observed distribution in R is shown in Figure 4. Note that the observed range in R is ~100 (~200 when the CTs are included). It is possible, of course, that the R_{90} covers a range of ~200 and that γ approaches 1. If that were the case, there would be no hope of distinguishing between the effects of the spread in R_{90} and

Doppler boosting on the R distribution, the latter of which would be small, anyway, due to the small γ. However, as we show below, for values of γ ~2–5, a modest range of R_{90} leads to a good fit to the observed R distribution (see Figure 4). These results are entirely consistent with those of OB and KS.

For a randomly oriented sample, the distribution in R can be calculated for given n, α, γ and R_{90}. A continuous jet with n=2 and α=0.2 is assumed. Unfortunately, the R distribution is sensitive to γ only at large R, where the observed number of sources is very small (OB). Distributions have been calculated with several γ factors. Scheuer and Readhead (1979) found γ ~2, while OB included "end-on" flat-spectrum, compact objects in their sample and found γ ~5. The OB value is entirely consistent with the γ needed to explain superluminal motion in compact, core-dominated sources and in the CC of 3C179.

The parameter that can best be constrained is R_{90}. The simple case where a single R_{90}, equal to the smallest observed R (0.01), and γ=5 are assumed does not fit the observations ($P(\chi^2)$ < ~0.05 in all trials, see Figure 4a). A uniform distribution in R_{90} from 0.01 to 0.03 provides an acceptable fit when the CTs are omitted (e.g., for γ=2, $P(\chi^2)$ ~0.40). The fit is optimized with a uniform distribution in R_{90} from 0.01 to 0.055 (e.g., for γ=5, $P(\chi^2)$ ~0.85), again omitting the CTs. The only case in which an acceptable $P(\chi^2)$ is obtained including the CTs is for γ=5 ($P(\chi^2)$ ~0.20) and a continuous distribution in R_{90} from 0.01

to 0.07, with the central values weighted more heavily. For larger ranges of R_{90}, $P(\chi^2)$ is still quite acceptable, but begins to drop; using R_{90}=0.01–0.10 and omitting the CTs, $P(\chi^2)$ ~0.60 for γ=2 and $P(\chi^2)$ ~0.45 for γ=5. (Only in the last case did rebinning from four to three bins lower an acceptable $P(\chi^2)$ below the threshold of 0.20, to 0.15.) The difficulty of obtaining a good fit with the CTs may be due to the problems of binning with small numbers. If 3C309.1, at the upper edge of the highest bin used, were moved to the next highest bin, $P(\chi^2)$ would rise well above 0.20. But it is still true that the inclusion of this object and 3C216 disturbs the high R end of the distribution, lowering $P(\chi^2)$, and these objects can just be accommodated.

The fact that an acceptable fit can be obtained with a spread in R_{90} of only a factor of ~3 indicates that a much narrower range is sufficient than the order-of-magnitude dispersion given in OB, but their mean value of 0.024 fits comfortably into the range given here. The mean value of R_{90} for the optimum fit, 0.033, is precisely the value given by Swarup, Sinha, and Hilldrup (1984) for a sample of extended quasars of large angular size. Therefore, the observed range of R can be explained by a small spread in R_{90} (a factor of >~3) and beaming with γ >~2 (giving an additional factor of >~40 in R between sources at $\theta = 90^\circ$ and 0°).

A rough estimate to the upper limit on γ can be made by calculating the value required to reproduce the observed range of R, assuming that the large L source 3C351, with the minimum observed R (0.01), is oriented at $\theta=90^{\circ}$, and that all objects have the same intrinsic CC strength. It shall be assumed that the object with the largest observed R in a sample of N objects is oriented at an angle determined by $1 - \cos\theta = 1/N$. The sample including the compact triple 3C309.1, which has the largest observed R (2.00), requires $\gamma=4.2$. Similarly, $\gamma=3.8$ is needed for 3C245 (R=1.06) when the CTs are omitted. (The individual spectral indices for each source have been used in these calculations.) If an attempt is made to account for the compact, flat-spectrum objects 3C345 and 3C454.3 (R~25) as end-on doubles at $\theta\sim0^{\circ}$, then $\gamma\sim5$ would be necessary, as both KS and OB found in their tests which include core-dominated sources. Setting $\theta=10^{\circ}$ for 3C345, a plausible value considering the work of Biretta (1985) on superluminal expansion in the VLBI core, requires $\gamma\sim10$. This value of γ is, interestingly enough, the same as the minimum γ given by Biretta to explain the fastest apparent motion observed in 3C345. Thus, even in this last case, there is no compelling evidence for extreme values of γ, although the n vs. R histograms cannot help in ruling out very large values.

The spread in R_{90} could be due to several factors. R_{90} must vary over the lifetime of a source; because we have a sample of objects with a range of intrinsic linear size, and therefore with different ages, we expect to find a spread in R_{90}. This point is addressed further in the discussion of the R-L anti-correlation below (see part C.4.b.). Short-term variability on time scales of a few years could also contribute to this spread, although only one of the objects monitored to date shows variations as large as a factor of ~2 (see Chapter 2). There could be a modest range in the overall level of nuclear activity in sources of the same age, intrinsic to the objects, which leads to a spread in the strength of radio emission from the CCs. It could also be that, tied to the level of nuclear activity, there is a dispersion in γ that results in a range of transverse jet powers; more generally active objects could produce jets which are correspondingly more relativistic.

b. CC Strength vs. Projected Linear Size

Given the acceptable ranges of L_{90} and R_{90}, a correlation between R and L might be expected. There should be a tendency for large R to occur in small L sources at small angles to the line-of-sight, although some small R, small L sources would also be expected, given a continuous spread in intrinsic linear size. This effect is indeed seen in Figure 5, which shows a highly significant correlation. Hine and Scheuer (1980) and KS have noted this previously.

Several alternative explanations of the R-L anti-correlation are possible, but good arguments can be offered against them. These arguments are presented in KS and are not original, but we include them here for completeness. First, it is important to make certain that the CC strength-projected linear size anti-correlation is not due to a hypothetical CC strength-redshift correlation

(CCs stronger at earlier epochs) coupled with a possible projected linear size-redshift anti-correlation. As we have shown, there is no R-z correlation. Second, the fact that there is no R-P_e correlation shows that that the anti-correlation of CC strength and projected linear size is not just due to the combined effect of a hypothetical CC strength-luminosity correlation and a possible luminosity-projected linear size anti-correlation.

Third, the R-L anti-correlation might be explained as being due to stronger CCs residing in young, small sources, with the CC decaying as the source expands. It is not known very well from theory what the precise course of nuclear activity will be over the lifetime of a source; but one could imagine nuclear activity diminishing as a source ages if the surrounding "fuel supply" is all eventually consumed by the "central engine." But the presence of small R, small L sources argues against this scenario, although it is true that these sources tend to have slightly larger R than the small R, large L objects. Thus there could well be young sources (if L is positively correlated with age) with relatively weak CC activity.

With these alternative explanations dismissed, we note that the R-L anti-correlation is readily accounted for by CC beaming and randomly oriented sources with a continuous distribution of intrinsic linear size.

Deviations from the mean R-L anti-correlation could be explained by the spread in R_{90} and variations in the density of the surrounding medium. It is also possible that an intrinsic bend in a jet could lead to the VLBI-scale jet pointing a bit more toward or away from the angle to the line-of-sight defined by the source axis through the outer jet and lobes. The CC would correspondingly be brightened or dimmed for a given large-scale Θ and L_{90}. This is probably not a strong effect, since in most objects studied thus far, the VLBI structures are fairly well aligned with the outer structures, although there are indications of possible misalignments of up to ~ 10° in some objects (see Chapter 2).

The small L, large R sources (most likely to be Doppler-boosted) do not have larger extended structure powers than the small L, small R sources or than many of the large L, small R sources. This suggests that large-scale beaming may have only a small effect on P_e, and thus supports the argument that there is little orientation bias in the sample.

If it is assumed then that the R-L anti-correlation is dominated by orientation and Doppler-beaming effects, and that the bulk velocity of matter along the jets is the same in all objects, then it is possible to estimate the bulk Lorentz factor from the available statistics. To quantify the R-L anti-correlation, it is useful to take the mean values of R for the small R sources in the bin with largest L, $R_1 = 0.058$, and the larger R (> 0.2) sources in the bin with smallest L, $R_2 = 0.84$ (or 1.20 with the CTs); see Figures 3 and 5. This will permit a comparison of CC strength between the sources which most likely have the largest and smallest median θ, respectively. Note that all of the sources in the bin with largest L have been included. However, only the larger R sources have been used from the bin with smallest L, because the smaller R sources in this bin could well be intrinsically small objects oriented at large θ. Thus, only those objects with $R > 0.2$, which stand out from all other objects over the entire range of L, have been included.

The best estimate of θ_1 is based on the assumptions of random orientations and a uniform L_{90} distribution; the median value of θ for sources which would fall in the bin with largest L is $\theta_1 = 73^\circ$. A similar estimate cannot easily be made for θ_2, because of the presence of some sources with small R in the bin with smallest L mentioned above. Instead, a reasonable estimate of θ_2 is obtained by assuming that the n sources with largest R in a sample of N objects are those aligned within $\theta_{max} = \arccos(1 - n/N)$ to the line-of-sight; the median value of θ between 0° and θ_{max} is then $\theta_2 = 21^\circ$ (or 27° with the CTs). A calculation of the predicted ratio R_2/R_1, using θ_1, θ_2, and the average spectral indices for the two groups of objects requires $\gamma = 1.9$ (or 2.6 with the CTs) to reproduce the observed ratio for

$$R_i \propto \{\gamma[1-\beta\cos\theta]\}^{-(2+\alpha)} + \{\gamma[1+\beta\cos\theta]\}^{-(2+\alpha)}, \qquad (3)$$
$$i = 1, 2$$

with β replaced by $-\beta$ for a receding jet. This is approximately the value of γ which Scheuer and Readhead (1979) found appropriate for the CCs of "classical doubles" based on the distribution of CC strength in 3C quasars; they also argued against $\gamma \sim 5$, since in that case there should be many more sources without detectable CCs than are observed.

Values of γ much larger than 2 pose only slight difficulties within the framework of the simple beaming model for the sample of "classical doubles." For instance, if $\gamma=5$, the median angle of the large R objects would have to be increased to $\theta_2 = 34^o$ in order to reproduce the observed ratio R_2/R_1, which in turn implies that five of the fifteen objects should be in the large R group ($R > 0.2$) instead of the two objects observed. When the compact triples are included, doubling the number of large R objects, the shift in median angle is small for $\gamma=5$ or even 10, and the discrepancy in the number of large R objects does not occur. Thus, the simple beaming model weakly favors $\gamma \sim 2$ over $\gamma \sim 5$ for the "classical doubles" alone; no such distinction can be made when the compact triples are included and treated as nearly end-on doubles. It is interesting to note that if the OB "unified scheme" is adopted, and 3C345 and 3C454.3 could be included in the sample on the basis of their extended emission, then the above discrepancy for $\gamma=5$ vanishes. In fact, $\gamma=5$ or 10 is then required to explain the high R values for these objects.

This hint of a mild difficulty with the $\gamma=5$ case suggests that a slight departure from the simple model, in which some fraction of the CC flux density is assumed to be isotropic, may more easily admit $\gamma > 2$ for the "classical doubles." For instance, if $\gamma=5$, the observed ratio R_2/R_1 can be matched if ~ 20 per cent of the total flux density which would be observed for a stationary source is unbeamed; the other ~ 80 per cent is contained in beamed jets. In terms of R values, this corresponds to an unbeamed component with $R_u=0.049$ and a beamed component with $R_b(90^\circ) = 0.007$; thus, the total R_{90} would be 0.056. No problems arise as to the number of sources expected at large R. Thus, a modest amount of isotropic, or perhaps only mildly beamed, radiation allows $\gamma=5$ while still correctly predicting the observed ratio R_2/R_1. This obviates the difficulty with $\gamma=5$ encountered by Scheuer and Readhead (1979), since the unbeamed radiation would make most CCs detectable, whatever their orientations. This could also account for the significant flux density variations in some strong CCs and lack thereof in weak CCs monitored to date, if the variable component is identified with the beamed component (see Chapter 2). Clearly, other values of γ are possible with this additional free parameter. In fact, the fraction of unbeamed radiation is a maximum at ~0.2 for γ~3-5. For higher values of γ, the radiation becomes beamed within such a narrow cone that the strongest flux boosting occurs at angles very close to the line-of-sight; in addition, the fraction of beamed emission must increase to compensate for the severe Doppler diminution at larger angles to the line-of-sight. Hence, the fraction of unbeamed radiation required in this model decreases for $\gamma > 5$; it is ~0.05 for $\gamma=10$, and only ~0.02 for $\gamma=20$.

c. Distribution of CC Strength Including Isotropic Emission

To support the marginal result from the R-L anti-correlation, indicating that some fraction of unbeamed emission is required for the "classical doubles" if $\gamma=5$, the distribution of R for the whole sample discussed in part C.4.b must be reconsidered. For $\gamma=5$, there is clearly no need to add any unbeamed radiation for the optimum range of $R_{90}=0.01-0.055$, since the fit is excellent ($P(\chi^2) \sim 0.85$). In fact, if the distribution is recalculated with 20 per cent unbeamed emission, the fit is degraded to an unacceptable degree ($P(\chi^2) \sim 0.10$).

For $\gamma=5$ and the larger range of $R_{90}=0.01-0.10$, however, it is possible to increase $P(\chi^2)$ somewhat by including some fraction of unbeamed flux density, F_u. For $F_u=0.0$, $P(\chi^2) \sim 0.45$ as given above. For $F_u=0.2$, $P(\chi^2)$ improves to 0.60, but a further increase to $F_u=0.4$ lowers $P(\chi^2)$ to 0.30. The fact that $F_u=0.2$ optimizes $P(\chi^2)$ for this large range of R_{90}, centered on $R_{90}=0.055$, is consistent with the suggested need for 20 per cent unbeamed emission from the R-L analysis, where the average value of R_{90} for the large L sources is predicted to be 0.056. But, of course, the fit with $R_{90}=0.01-0.055$ and $F_u=0.0$ is still better than the one with $R_{90}=0.01-0.10$ and $F_u=0.2$. Therefore, there is no reason to invoke any isotropic emission based on the available statistics, even for the $\gamma=5$ case, although it cannot be ruled out.

While this result favoring $F_u=0.2$ for $\gamma=5$ is of marginal significance, it is possible to obtain a rough upper limit to F_u. As the range of R_{90} increases, so does the permissible value of F_u; this is because the total range of R can be accounted for more by the intrinsic spread in R_{90} and less by Doppler flux boosting, with γ held fixed. If an order-of-magnitude spread in R_{90} is assumed (0.01–0.10), which is about as large a range as one might expect from inspection of the R–L diagram in Figure 5, then $F_u=0.5$ yields $P(\chi^2)$ of only ~0.15. Thus, if γ is typically 5 and if there is isotropic emission, no more than about half of the total emission which would be observed for a stationary source may be unbeamed.

d. Optical Luminosity vs. CC Strength

The optical luminosity of these objects may well undergo modest or even no enhancement due to beaming. It is certain that the line emission is unbeamed, and recent estimates of the degree of continuum beaming in different samples suggest possible boosting by a factor of ~3–5 (Browne and Wright 1985, Hutchings and Gower 1985). It is true that if there is significant optical beaming, then there may be an orientation bias introduced by selecting double-lobed quasars over radio galaxies. But the optical luminosity may provide an independent observable free from orientation bias. To calculate specific luminosities, visual magnitudes were taken from the compilation in Laing, Riley, and Longair (1983), with no attempt to correct for galactic obscuration (all objects are at least 10° from the galactic plane). The flux calibration of Oke and Schild (1970) was used, and an optical spectral index of 0.5 was assumed. No correlation is found between the optical luminosity and R, even over the entire redshift range (see Figure 6, Table 4). This result is consistent with beaming of central radio components and isotropic radiation from the optical components. In fact, the CTs 3C43 and 3C216, among the sources with the largest R values, are among the objects with the smallest optical luminosities. This suggests that differences in R due to orientation effects may be greater than those due to the level of nuclear activity, in agreement with the small intrinsic range of R_{90} needed on the beaming theory to explain the large observed range of R.

e. Curvature vs. Projected Linear Size and CC Strength

A further check of the Doppler-boosting effect in a randomly oriented sample is provided by considering the correlation of curvature, C, with L and R. If a source has a typical intrinsic misalignment of a few degrees or less between the lines joining the CC to either outer "hot spot," then large C can occur only in a source with its axis at a small angle to the line-of-sight (i.e., one with small projected linear size). KS have noted this effect. A plot of C vs. L in Figure 7 demonstrates that this C-L anti-correlation exists here when the three compact triples are included, although it is not statistically significant if they are omitted. Still, in the latter case, $C > 10^{\circ}$ occurs only for $L < 100$ kpc, if 3C215 is disregarded. There are also many small C, small L sources, which can be explained by the population of intrinsically small sources at large angles to the line-of-sight. An alternative explanation (Readhead et al., 1978) for this anti-correlation is that sources become large and remain straight only when the beams are able to plow undeflected through the surrounding medium. Variations in local conditions near the nucleus could be such that beams are often impeded and experience varying amounts of deflection. Some beams, however, can escape undisturbed through openings in an inhomogeneous medium.

We have shown that there is an anti-correlation between R and L. Thus, there will be a tendency for large C to be associated with large R, as shown in Figure 8. KS have also found this correlation in their sample. Again, this trend is significant with the three compact triples included, but loses its significance when they are excluded. Still, in the latter case, $C > 10^{\circ}$ occurs only for $R > 0.1$, if 3C215 is disregarded. This correlation conforms with the beaming model--strong CC sources often have large apparent curvature. The alternative explanation mentioned above might also account for this trend, however, if some sources are misaligned because the jets encounter infalling matter in a very active core; only in the weak cores do the jets move outward undeflected.

Thus, while not as convincing as the R-L anti-correlation, the trends for C to be correlated with R and anti-correlated with L are nonetheless consistent with CC beaming in a randomly oriented sample.

D. The High Redshift Sample

The above correlation tests were conducted for the high redshift sample, but with a total of only eight objects it is not surprising that no significant trends were found (except possibly when 3C43 is included; see Table 6). Because of the very small number of objects, no chi-square tests were performed on the distributions. The results are nevertheless consistent with beaming and the range of parameters which fit the low redshift sample, with both L_{90} and R_{90} scaled down by a factor ~3. The higher density of the surrounding medium at large z may confine the sources more effectively, if indeed linear size does decrease with z despite any selection effects in the sample. It also appears that R may be smaller at higher redshift; a marginal log R-z anti-correlation across all redshifts has been noted above. Swarup, Sinha, and Hilldrup (1984) found the opposite trend, but they did not correct their normalized CC strengths to a standard emitted frequency, which thus will make the CCs appear stronger relative to the outer lobes at high redshift because of the much steeper spectral index of the extended emission. Again, there may be effects due to the flux density selection criterion which are responsible for the observed marginal anti-correlation. It will ultimately be very interesting to see, however, if there is any dependence of R on z, since this would have implications for compact radio core evolution.

There are some indications of similar trends for R vs. L and C vs. R when 3C43 is included, but it is not clear whether or not this object satisfies the flux density criterion of the sample. This source has been indicated in parentheses when included on the correlation plots. Note that the compact triple 3C191 has been included in all tests.

It is of interest to look at the number distribution with curvature for the low and high redshift samples separately. While there is no evidence for a C−z correlation for the low z, high z, or combined redshift ranges, it is true that the high redshift sample, including 3C43, exhibits a larger range of curvature than the low redshift sample (see Figure 9). Even omitting 3C43, the high z sample is not peaked at small curvatures ($< 15^{\circ}$) as the low z sample. This is consistent with the result first emphasized by Barthel (1984), for a sample which contains over half of the sources in our sample, that high redshift quasars exhibit more convoluted structure than those at low redshift. Barthel's dividing line in redshift is not too different from z=1.3 used here. He found that this effect is independent of luminosity. The results presented here must be regarded with caution, however, because of the small number statistics. It should be emphasized that these objects are not being compared with the compact, steep-spectrum sources, some of which lie at low redshift and show very distorted structures (e.g., 3C48; Wilkinson 1985).

E. Tests of Beaming in the Extended Structure

The simplest test of large-scale beaming using the ratio of outer lobe flux densities is not very useful, as discussed by KS. There are contributions from beamed and unbeamed components which must be sorted out carefully from detailed, high-resolution maps. The existing maps for this sample do not permit this test to be done at present. The velocity of advance of the outer "hot spots" has been shown to be < ~0.2c by Longair and Riley (1979) by analysis of the ratio of distances from the CC to either "hot spot," so we need not consider this test here.

Perhaps a more useful diagnostic of the degree of large-scale beaming is the connection between CC strength and the presence of a large-scale jet. Saikia (1984) found that large-scale jets occur more often in sources with prominent CCs, and that sources without jets almost never display a prominent CC. This result is expected if beaming occurs on both the small and large scales; those objects at small angles to the line-of-sight have both Doppler-boosted CCs and jets, with the jets becoming visible (at the current observational limits) only in such favorably oriented sources. A similar result is found for this sample. The "classical doubles" with the six strongest CCs all have one-sided large-scale jets, which tend to be quite prominent; about one-third of the remaining objects with weaker CCs are known to have jets and, when present, the jets tend to be relatively weak (see Table 1 and references therein).

Owen and Puschell (1984) suggested that $\gamma < \sim 2$ for large-scale jets, based on the statistics of jet detection in a complete sample of quasars from the Jodrell Bank 966 MHz survey (the same sample being used in the Zensus and Porcas (1984) VLBI study). A Lorentz factor greater than this is certainly not needed to conceal any counterjets that might be present, although the maps are made with ~20 minute integrations and are of limited sensitivity. Yet they argued that, for example, $\gamma=5$ would lead to a few very luminous jets (> 1 Jy) in their sample, which are not observed. Given the quality of the available maps in the present sample of 3C sources, a similar, tentative conclusion can be drawn that the large-scale bulk Lorentz factor need not exceed ~2 (again, see Table 1 and references therein), but a firm upper limit on γ awaits high-sensitivity VLA maps of the complete sample.

IV. Discussion

The observed (anti-)correlations involving central component strength, curvature, and projected linear size are all consistent with the relativistic beaming theory for the CCs. A plausible range of intrinsic linear size and a modest range of intrinsic CC strength serve to explain the observed distributions of L and R. The CC strength histogram can be explained with only modest γ (~2-5), but it is not possible to establish a firm upper limit to γ based on the present statistics. The anti-correlation between R and L is precisely what one expects if large R is due to Doppler boosting at a small angle to the line-of-sight, which results in foreshortening of the apparent linear size. Sources do exist with small R and small L, and these can be explained naturally as objects which are just intrinsically small, lying toward the plane of the sky. There is weak evidence from the R-L anti-correlation and the distribution of R that perhaps ~20 per cent of the total emission is unbeamed, if γ is typically ~5 rather than ~2 and if the intrinsic CC strength ranges over an order-of-magnitude. This isotropic emission could arise in a stationary central source and/or cocoons surrounding the jets.

There may also well be a real tendency for the curvature to be correlated with CC strength and anti-correlated with projected linear size. These trends are statistically significant only when treating the compact triples as small double-lobed sources, but are suggested by the data even when these sources are excluded. These relationships can also be understood in terms of random orientations and beaming. Given a small typical intrinsic misalignment in each jet, only those sources oriented in the correct geometry toward the line-of-sight will exhibit large apparent curvatures. From the discussion above, these are precisely the sources which have large R and small L. The trend for a larger mean curvature at high z could be explained, as Barthel (1984) suggested, by a density increase in the surrounding medium with redshift or by precession/rotation of the "central engine."

Although included from the outset, it is not clear after this analysis that the compact triples should be treated as nearly end-on double sources. The reasons to doubt this treatment are as follows:

(1) there are difficulties in fitting the L and R distributions with these objects;

(2) the very large bends (~90°) between the VLBI and outer structures in 3C216 (Pearson and Readhead 1984) and in 3C309.1 (Kus, Wilkinson, and Booth 1981) are atypical of "classical doubles" (see Chapter 2), and the probability of a source with an intrinsic bend of ~5° to exhibit an apparent bend of ~90° is ~10^{-4};

(3) the CCs seem to have very steep spectra (α=0.7 for 3C309.1);

(4) there is significant variability on ~1-year time scales in the "classical doubles" with strong CCs (e.g., 3C207 and 3C245, see Chapter 2), yet the CCs of the compact triples 3C216 and 3C309.1 display mild, if any, variability on ~10-year time scales (Andrew, et al. 1978; Seielstad, Readhead, and Pearson 1983).

There is some indication of a link between CC and large-scale beaming, based on the tendency for the more prominent CCs to reside in sources with strong large-scale jets. In order to quantify this trend and establish an upper limit on the large-scale γ, further work obtaining high-sensitivity maps with the VLA will be required.

While it is undoubtedly true that different levels of nuclear activity, different environments surrounding the sources, and other effects can lead to deviations from predictions of beaming in a given individual source, it is striking how well the simple beaming model applied to the central components can account for the various observed relationships. OB and KS, among others, have noted this previously, that while beaming is not the sole effect, the source statistics are consistent with its playing a large role. While all of these statistical tests of beaming have been performed before, most thoroughly by OB and KS and with similar results, it is of key importance to demonstrate that all the known correlations hold for the particular complete sample defined herein for the purpose of an intensive VLBI study of CC structures, alignments, and motion.

Proposed VLBI Tests Based on Compact Structure

The direct tests will now come with the VLBI maps, which will allow a comparison of the morphology and alignment of the CC and outer structures in detail, and will most importantly permit tracking components at multiple epochs to search for superluminal motion. The orientation bias introduced into the VLBI subsample by observing only the relatively strong CCs will have to be accounted for.

This bias will alter the predicted distributions of apparent transverse velocity, β_{app}, and position angle difference between the small- and large-scale structures, ΔPA, from those of the case of random orientations, as discussed below. Since the distribution of β_{app} for the simple beaming model will in principle allow a determination of γ, this could have important implications for theories of jet production in terms of the acceleration mechanism and the identity of the particles in the jet (i.e., electron-proton versus electron-positron plasma). Together with a knowledge of γ, finding the typical intrinsic jet bending angle from the distribution of ΔPA should help to discriminate among different proposed mechanisms for bending relativistic jets (Begelman, Blandford, and Rees 1984).

The distribution of β_{app}, $P(\beta_{app})$, is calculated simply from

$$\beta_{app} = \frac{\beta \sin \theta}{1 - \beta \cos \theta} \qquad (4)$$

and the fact that $P(\theta)=\sin\theta\Delta\theta$. For the total sample with random orientations, θ ranges from 0° to 90°. As an example of how the selection effect favoring strong CCs in the VLBI subsample can be accounted for, $P(\beta_{app})$ is also calculated for $\theta=0^\circ$ to 60°; this would be appropriate if, for instance, the VLBI subsample contained the half of the total sample with the strongest CCs, which would then all be expected to be aligned within ~60° of the line-of-sight. Observations of a sample approaching ~10 objects would permit making a distinction between γ~1-3 and γ~4-6; see Figure 10. At z=1,

β_{app}=2 would produce a readily detectable angular displacement of ~0.1 millarcsecond in ~2 years. Thus, there is hope of determining whether γ is more typically ~2 or > ~5; it would be difficult to rule out γ >5, because the number of objects predicted to have exceedingly large β_{app} is very small. If the dispersion in γ is much larger than this (e.g., $\Delta\gamma$ = +/- 2), it then becomes difficult to distinguish between a range of γ from 1 to ~5 and a distribution of γ centered on ~5. It should always be kept in mind that the discovery of large superluminal motion in even a few of these quasar CCs would spell trouble for simple beaming theories. If the sample is truly randomly oriented, only a small fraction of the objects should exhibit strong superluminal motion. If many objects are found to be strongly superluminal, even in a slightly biassed subsample, theories which can predict such motion over a wide range of orientations will be required (e.g., Blandford 1984; Scheuer 1984).

The distribution of ΔPA can be calculated by assuming that each jet has an intrinsic bend, ξ, between the initial and "final" jet directions. This "final" direction can be chosen at the physical size scale of interest; e.g., for focusing on bending close to the core, one might choose to ignore bends and wiggles in the far reaches of the outer lobes and define the "end" of the jet at an inner knot. The apparent bend, observed as ΔPA, is given by

$$\Delta PA = \arctan\left[\frac{\sin\xi\sin\phi}{\sin\theta\cos\xi + \cos\theta\sin\xi\cos\phi}\right], \qquad (5)$$

where Θ is the angle between the initial jet direction and the line-of-sight and ϕ is the angle between the plane containing Θ and the plane of the jet (Readhead, Napier, and Bignell 1980; Readhead, et al. 1983). For a given ξ, the distribution of ΔPA at fixed Θ is calculated using the fact that all values of ϕ between 0° and 180° are equally probable. The total probability distribution, P(ΔPA), is found by multiplying by $P(\Theta)=\sin\Theta\Delta\Theta$ and summing over the appropriate range of Θ. P(ΔPA) is calculated again for the two ranges of Θ, 0° to 90° and 0° to 60°. The distributions for both the unbiassed and biassed samples, assuming $\xi=2^\circ$, 5°, and 10°, are shown in Figure 11. For a given ξ, the probability of observing large ΔPA is greater for the biassed sample, as expected. It is also clear that for a sample approaching ~10 objects, it should be possible to determine the typical value of ξ to within $\sim 2^\circ$. However, it may not be possible to determine the range of ξ since, for example, the distributions for $\xi= 5^\circ$ and a range of ξ from 0° to 10° are very similar.

Clearly, large apparent velocity and large apparent curvature should tend to occur in the large R, small L sources argued herein to be aligned closest to the line-of-sight. Furthermore, ΔPA provides a probe of jet curvature down to the ~parsec scale, and, in conjunction with the misalignment angle, C, should indicate the physical size scale on which the most significant bending occurs.

In principle, the distribution of VLBI jet/counterjet brightness ratios could be used to determine γ, or, inverting the problem, lower limits to jet/counterjet brightness ratios could be used to address the issue of one-sided versus two-sided jets, given a knowledge of γ. But because the CC jets are definitely going to be weak and the sensitivity of VLBI is limited, there is not much promise of settling the sidedness debate unless, of course, two-sided VLBI jets are discovered in at least some of the objects.

Proposed VLA Tests Based on Large-scale Jets

There is hope, however, that high-sensitivity VLA maps will provide a definitive answer to the sidedness question on the large scale. Assuming that the true jet/counterjet brightness ratios can at least be roughly approximated by the predictions of the simple beaming model, both jets and counterjets should reveal themselves on very sensitive maps of the sources of largest angular size. Wardle and Potash (1984) have found that the eight largest sources in their 4C sample all have one-sided jets, and they use this observation and limits on jet/counterjet brightness ratios to argue against beaming and in favor of a flip-flop mechanism (e.g. Rudnick 1982). The quality of the available maps for the eight largest 3C sources is not uniform, but at least two of them have VLA maps which reveal no jet at all (3C47 and 3C263; see Table 2). Only two of the five objects with available VLA maps clearly contain visible jets (3C204 and 3C334; see Table 2). It will be necessary now to examine the occurrence of large-scale jets and the distribution of jet/counterjet brightness ratios in the 3C sample, and to determine if this difference between the 3C and 4C samples can be accounted for by any selection effects.

V. Conclusions

A complete sample of double-lobed quasars has been defined, which is argued to be largely free of orientation bias. The statistical tests performed above are consistent with random source orientations and relativistic beaming in the central components. These tests provide no real constraint on the maximum bulk Lorentz factor, γ, although there is no evidence that $\gamma > \sim 5$ is necessary, and $\gamma \sim 2$ is clearly sufficient. If γ is typically ~5, and if the intrinsic CC strength spans an order-of-magnitude, weak evidence exists that ~20 per cent of the total CC emission may be unbeamed. Mark III VLBI maps of these CCs are being made. The distribution of apparent velocity from the VLBI studies will permit a direct test of beaming in the CCs, including the possible determination of the typical bulk Lorentz factor. The distribution of apparent curvature between ~parsec- and >~kiloparsec-scale structures will allow determination of typical intrinsic jet bending angles. The occurrence of large-scale jets preferentially in sources with prominent CCs suggests a connection between small- and large-scale beaming. Further intensive VLA observations are required to assess the degree of large-scale beaming and study the question of one-sided versus two-sided ejection from the "central engine."

NOTES ADDED IN PROOF

(1) It has come to our attention that confirmation of the optical identification of 3C14 as a quasar was given by Perryman, et al. (1984), with z=1.469. Thus, as expected, this object does not belong to the low redshift sample. It has not been added to the high redshift sample.

(2) We should also note that it belatedly came to our attention that a central component has been detected in 3C336 by Swarup, Sinha, and Hilldrup (1984). The measured flux density is only slightly below the previous upper limit (29 mJy vs. <40 mJy). The analysis of the R histogram takes this small change into account, but the other tests do not.

References

Andrew, B.H., MacLeod, J.M., Harvey, G.A., and Medd, W.J. 1978, *A.J.*, **83**, 863.

Baars, J.W.M., Genzel, R., Pauliny-Toth, I.I.K., and Witzel, A. 1977, *Astr.Ap.*, **61**, 99.

Barthel, P.D. 1984, Ph.D. dissertation, Leiden.

Begelman, M.C., Blandford, R.D., and Rees, M.J. 1984, *Rev.Mod.Phys.*, **56**, 255.

Bentley, M., Haves, P., Spencer, R.E., and Stannard, D. 1975, *M.N.R.A.S.*, **173**, 93P.

Biretta, J.A. 1985, Ph.D. dissertation, California Institute of Technology.

Blandford, R.D. 1984, in IAU Symposium 110, *VLBI and Compact Radio Sources*, ed. R. Fanti, K. Kellermann, and G. Setti (Dordrecht:Reidel), p.215.

Blandford, R.D., and Königl, A. 1979, *Ap.J.*, **232**, 34.

Bridle, A.H., and Perley, R.A. 1984, *Ann.Rev.Astr.Ap.*, **22**, 319.

Browne, I.W.A., and Wright, A.E. 1985, *M.N.R.A.S.*, **213**, 97.

Burbidge, G.R., Crowne, A.H., and Smith, H.E. 1977, *Ap.J. Suppl.*, **33**, 113.

Burch, S.F. 1979, *M.N.R.A.S.*, **186**, 293.

Burns, J.O., Basart, J.P., DeYoung, D.S., and Ghiglia, D.C. 1984, *Ap.J.*, **283**, 515.

Cawthorne, T.V.C. 1984, Ph.D. dissertation, Cambridge.

Fanaroff, B.L. and Riley, J.M. 1974, *M.N.R.A.S.*, **167**, 31P.

Fanti, C., Fanti, R., Parma, P., and Schilizzi, R.T. 1984, in IAU Symposium 110, *VLBI and Compact Radio Sources*, ed. R. Fanti, K. Kellermann, and G. Setti (Dordrecht: Reidel), p.57.

Fanti, C., Fanti, R., Parma, P., Schilizzi, R.T., and van Breugel, W.J.M. 1985, *Astr.Ap.*, **143**, 292.

Foley, A.R. 1982, Ph.D. dissertation, Manchester.

Hine, R.G., and Longair, M.S. 1979, *M.N.R.A.S.*, **188**, 111.

Hine, R.G., and Scheuer, P.A.G. 1980, *M.N.R.A.S.*, **193**, 285.

Hintzen, P., Ulvestad, J., and Owen, F. 1983, *A.J.*, **88**, 709.

Hooley, A., Longair, M.S., and Riley, J.M. 1978, *M.N.R.A.S.*, **182**, 127.

Hutchings, J.B., and Gower, A.C. 1985, *A.J.*, **90**, 405.

Jenkins, C.J., Pooley, G.G., and Riley, J.M. 1977, *Mem.R.A.S.*, **84**, 61.

Jones, D.L., et al. 1986, *Ap.J.*, **305**, in press.

Kapahi, V.K., and Saikia, D.J. 1982, *J.Astr.Ap.*, **3**, 465.

Kus, A.J., Wilkinson, P.N., and Booth, R.S. 1981, *M.N.R.A.S.*, **194**, 527.

Laing, R.A. 1981a, *M.N.R.A.S.*, **194**, 301.

Laing, R.A. 1981b, *M.N.R.A.S.*, **195**, 261.

Laing, R.A., and Peacock, J.A. 1980, *M.N.R.A.S.*, **190**, 903.

Laing, R.A., Riley, J.M., and Longair, M.S. 1983, *M.N.R.A.S.*, **204**, 151.

Legg, T.H. 1970, *Nature*, **226**, 65.

Lind, K.R., and Blandford, R.D. 1985, *Ap.J.*, **295**, 358.

Linfield, R.P. 1981, *Ap.J.*, **244**, 436.

Longair, M.S. 1966, *M.N.R.A.S.*, **133**, 421.

Longair, M.S., and Riley, J.M. 1979, *M.N.R.A.S.*, **188**, 625.

Lonsdale, C.J., and Morison, I. 1983, *M.N.R.A.S.*, **203**, 833.

Masson, C.R. 1980, *Ap.J.*, **242**, 8.

Menon, T.K. 1976, *Ap.J.*, **204**, 717.

Miley, G.K. 1971, *M.N.R.A.S.*, **152**, 477.

Miley, G.K., and Hartsuijker, A.P. 1978, *Astr.Ap.Suppl.*, **34**, 129.

Oke, J.B., and Schild, R.E. 1970, *Ap.J.*, **161**, 1015.

Orr, M.J.L., and Browne, I.W.A. 1982, *M.N.R.A.S.*, **200**, 1067.

Owen, F.N., Porcas, R.W., and Neff, S.G. 1978, *A.J.*, **83**, 1009.

Owen, F.N., and Puschell, J.J. 1984, *A.J.*, **89**, 932.

Peacock, J.A., and Gull, S.F. 1981, *M.N.R.A.S.*, **196**, 611.

Pearson, T.J., Perley, R.A., and Readhead, A.C.S. 1985, *A.J.*, **90**, 738.

Pearson, T.J., and Readhead, A.C.S. 1984, in IAU Symposium 110, *VLBI and Compact Radio Sources*, ed. R. Fanti, K. Kellermann, and G. Setti (Dordrecht: Reidel), p.15.

Perryman, M.A.C., Lilly, S.J., Longair, M.S., and Downes, A.J.B. 1984, *M.N.R.A.S.*, **209**, 159.

Pooley, G.G., and Henbest, S.N. 1974, *M.N.R.A.S.*, **169**, 477.

Porcas, R.W. 1981, *Nature*, **294**, 47.

Potash, R.I., and Wardle, J.F.C. 1979, *A.J.*, **84**, 707.

Readhead, A.C.S. 1986, private communication.

Readhead, A.C.S., Cohen, M.H., Pearson, T.J., and Wilkinson, P.N. 1978, *Nature*, **276**, 768.

Readhead, A.C.S., Hough, D.H., Ewing, M.S., Walker, R.C., and Romney, J.D. 1983, *Ap.J.*, **265**, 107.

Readhead, A.C.S., Napier, P.J., and Bignell, R.C. 1980, *Ap.J.(Letters)*, **237**, L55.

Riley, J.M., and Pooley, G.G. 1975, *Mem.R.A.S.*, **80**, 105.

Riley, J.M., and Pooley, G.G. 1978, *M.N.R.A.S.*, **184**, 769.

Rogers, A.E.E., et al. 1983, *Science*, **219**, 51.

Rudnick, L. 1982, in IAU Symposium 97, *Extragalactic Radio Sources*, ed. D.S. Heeschen and C.M. Wade (Dordrecht:Reidel), p.47.

Saikia, D.J. 1984, *M.N.R.A.S.*, **208**, 231.

Scheuer, P.A.G. 1984, in IAU Symposium 110, *VLBI and Compact Radio Sources*, ed. R. Fanti, K. Kellermann, and G. Setti (Dordrecht:Reidel), p.197.

Scheuer, P.A.G., and Readhead, A.C.S. 1979, *Nature*, **277**, 182.

Schilizzi, R.T., Kapahi, V.K., and Neff, S.G. 1982, *J.Astr.Ap.*, **3**, 173.

Seielstad, G.A., Readhead, A.C.S., and Pearson, T.J. 1983, *Pub.A.S.P.*, **95**, 842.

Stannard, D., and Neal, D.S. 1977, *M.N.R.A.S.*, **179**, 719.

Stocke, J., Christiansen, W., and Burns, J. 1982, in IAU Symposium 97, *Extragalactic Radio Sources*, ed. D.S. Heeschen and C.M. Wade (Dordrecht:Reidel), p.39.

Swarup, G., Sinha, R.P., and Hilldrup, K. 1984, *M.N.R.A.S.*, **208**, 813.

Swarup, G., Sinha, R.P., and Saikia, D.J. 1982, *M.N.R.A.S.*, **201**, 393.

Wardle, J.F.C., and Miley, G.K. 1974, *Astr.Ap.*, **30**, 305.

Wardle, J.F.C., and Potash, R.I. 1982, in IAU Symposium 97, *Extragalatic Radio Sources*, ed. D.S. Heeschen and C.M. Wade (Dordrecht:Reidel), p.129.

Wardle, J.F.C., and Potash, R.I. 1984, in the Proceedings of NRAO Workshop No. 9, *Physics of Energy Transport in Extragalactic Radio Sources*, ed. A.H. Bridle and J.A. Eilek (Green Bank:National Radio Astronomy Observatory), p.30.

Wilkinson, P.N. 1982, in IAU Symposium 97, *Extragalactic Radio Sources*, ed. D.S. Heeschen and C.M. Wade (Dordrecht:Reidel), p.149.

Wilkinson, P.N. 1985, private communication.

Zensus, J.A. and Porcas, R.W. 1984, in IAU Symposium 110, *VLBI and Compact Radio Sources*, ed. R. Fanti, K. Kellermann, and G. Setti (Dordrecht:Reidel), p.163.

Table 1

All Quasars in 3CR Complete Sample

Source	Class^1	z^2	$m_V{}^2$	$S_{CC}{}^3$	$S_T{}^4$	ψ	Refs.
3C9	II	2.012	18.2	<4	546	13	K1,P2,S5
3C14	D	(1)	20?	<30	606	23	J1,L5
3C43	T	1.457	20	950	1200	2.6	F2,J1,L1,P1,R1
3C47	II	0.425	18.1	61	1092	74	B2,B4,B5,M2,P2
3C48	CSS	0.367	16.2	--	5700	--	F2,P1
3C68.1	D	1.238	19.5	<20	824	47	J1,L2
3C138	CSS	0.759	17.9	--	4200	--	F1,F2,P1
3C147	CSS	0.545	16.9	--	8000	--	F2,P1
3C175	II	0.768	16.6	39	655	54	J1,M2
3C181	D	1.382	18.9	<60	655	7.5	P2
3C186	D2?	1.063	17.6	331	377	100	C1,R2,S1
3C190	T	1.197	20	100	800	4.5	F2,J1,P1,R1
3C191	IId?	1.956	18.4	35	600	5.1	B1,J1,P1,R1
3C196	Z	0.871	17.6	--	4329	--	P2,L2,L7,S1,W5
3C204	IId	1.112	18.2	26	338	39	B5,H1,L2,M2, O1,O2,P2
3C205	IId	1.534	17.6	23	665	19	B1,B5,L2,O2,P2
3C207	II	0.684	18.2	588	1430	13	L4,P2,R1,R4, W1,W3
3C208	IId	1.110	17.4	56	536	14	B5,J1,L2,L4, M1,M2
3C212	IId	1.049	19.1	148	884	11	D1,H1,J1,L2, L4,W3
3C215	II	0.411	18.3	25	407	50	H2,M2,P2,W2
3C216	T	0.668	18.5	1050	1800	2.0	F2,J1,P1,R1,S1
3C245	II	1.029	17.3	910	1557	9.1	F3,J1,L1,R4,W3

3C249.1	II	0.311	15.7	78	775	41	B5,H1,L4,L6, M2,P2,W1,W3
3C254	II	0.734	18.0	19	784	15	L2,L6,O2,P2,S1
3C263	II	0.656	16.3	130	1033	44	B3,M2,O1,P2, S1,S2,W3
3C268.4	IId	1.400	18.4	38	596	11	B5,H2,L2,L7, P2,S1
3C270.1	II	1.519	18.6	178	864	11	H1,J1,P3,R3, S1,S3
3C275.1	II	0.557	19.0	135	904	19	J1,R3,S3
3C286	CSS	0.849	17.3	--	6200	--	F2,P1
3C287	CSS	1.055	17.7	--	3280	--	F2,P1
3C309.1	T	0.904	16.8	2350	3450	2.5	F2,L1,P1,R1
3C325	D	(1)	20	<70	824	16	J1
3C334	II	0.555	16.4	165	566	56	H1,H2,J1,M2 R1,S1,W3,W4
3C336	II	0.927	17.5	29	685	24	P2,S4
3C343	CSS	0.988	20.6	--	1570	--	F2,P1
3C345	FSC	0.594	16.0	8610	8900	>3	P1
3C351	IId	0.371	15.3	15	1202	65	L2,L3,M2,R2
4C16.49	II	(1)	18.5	9	390	18	B1,L3,L6
3C380	CSS	0.691	16.8	--	7447	--	F2,J1,P1
3C432	D	1.805	18.0	<30	308	13	J1
3C454	CSS	1.757	18.5	--	800	--	B1,F2,J1,P1
3C454.3	FSC	0.860	16.1	12200	12500	>5	P1
3C455	D2?	0.543	19.7	--	923	3.2	J1,S1

Notes to Table 1

1. Class:
II(d) = "classical double," with two resolved components straddling optical quasar; "d" indicates double "hot spot" in one lobe.
D = simple double, with two unresolved components straddling optical quasar; no radio central component detected.
T = triple source, with two unresolved components straddling a radio central component coincident with the optical quasar.
D2 = two components, one of which is coincident with the optical quasar.
Z = inversion symmetric object.
FSC = flat-spectrum compact object.
CSS = steep-spectrum compact object.

2. Redshifts and visual magnitudes from Laing, Riley, and Longair 1983; ( ) indicates assumed redshift.

3. Flux densities of central components on scale of Baars, et al. 1977, with upper limits at twice the lowest map contour.

4. Total flux densities on scale of Baars, et al.; most from Laing and Peacock 1980 or Pearson, Perley, and Readhead 1985.

References to Table 1

B1=Barthel 1984

B2=Bentley, et al. 1975

B3=Browne, I., unpublished

B4=Burch 1979

B5=Burns, et al. 1984

C1=Cawthorne 1984

D1=Davis, unpublished

F1=Fanti, et al. 1984

F2=Fanti, et al. 1985

F3=Foley 1982

H1=Hine and Scheuer 1980

H2=Hintzen, Ulvestad, and Owen 1983

J1=Jenkins, Pooley, and Riley 1977

K1=Kronberg, unpublished, in Bridle and Perley 1984

L1=Laing 1981a

L2=Laing 1981b

L3=Laing, unpublished

L4=Laing, unpublished

L5=Laing, Owen, and Puschell, unpublished, in Bridle and Perley 1984

L6=Laing, Riley, and Longair 1983

L7=Lonsdale and Morison 1983

M1=Menon 1976

M2=Miley and Hartsuijker 1978

O1=Owen, Porcas, and Neff 1978

O2=Owen and Puschell 1984

P1=Pearson, Perley, and Readhead 1985

P2=Pooley and Henbest 1974

P3=Potash and Wardle 1979

R1=Readhead, private comm.

R2=Riley and Pooley 1975

R3=Riley and Pooley 1978

R4=Rudnick, unpublished

S1=Schilizzi, Kapahi, and Neff 1982

S2=Shone 1985, unpublished

S3=Stocke, Christiansen, and Burns 1982

S4=Swarup, Sinha, and Hilldrup 1984

S5=Swarup, Sinha, and Saikia 1982

W1=Wardle, unpublished

W2=Wardle, unpublished, in Bridle and Perley 1984

W3=Wardle, unpublished

W4=Wardle and Potash 1982

W5=Wilkinson 1982

Table 2

The Complete Sample of Double-lobed Quasars

Source	R	L	C	Large-scale Jet?
3C9	<0.003	71	-	Yes
3C43[1]	3.18	15	86	No
3C47	0.042	327	5	No
3C68.1	<0.014	270	-	No
3C175	0.039	294	6	No
3C181	<0.054	43	-	No
3C190[2]	0.082-0.122	26	21	No
3C191[2]	0.026-0.045	28	0	?
3C204	0.040	223	2	Yes
3C205	0.017	108	5	No
3C207	0.624	69	20	Yes
3C208	0.057	80	3	Yes
3C212	0.111	63	0	Yes
3C215	0.048	217	(12)	?
3C216[3]	0.979-1.26	11	25	No
3C245	1.06	52	5	Yes
3C249.1	0.087	154	9	Yes
3C263	0.071	230	1	No
3C268.4	0.041	63	20	Yes
3C270.1	0.066	63	35	?
3C275.1	0.122	94	23	Yes
3C309.1	2.00	14	37	?
3C334	0.183	277	4	Yes
3C336	0.027	135	12	No

3C351	0.010	268	5	?
3C432	<0.044	72	-	No

Notes to Table 2

1. 3C43 requires $\alpha > 1.1$ for the extended emission and a strongly self-absorbed core to qualify for the sample.

2. 3C190 and 3C191 qualify for the sample if α for the extended structure $\gtrsim$ the integrated α.

3. 3C216 requires $\alpha > 0.8$ for the extended emission and a slightly self-absorbed core to qualify for the sample.

Table 3

Central Components with S > 30 mJy at 5 GHz

Source	S_{CC}	Investigators
3C43	950	Simon, Scheuer, Cawthorne, and Hough
3C47	61	--
3C175	39	--
3C190	100	--
3C191	35	--
3C207	588	Hough and Readhead
3C208	56	--
3C212	148	Hough and Readhead
3C216	1050	Pearson and Readhead
3C245	910	Hough and Readhead
3C249.1	78	Hough and Readhead
3C263	130	Zensus, Hough, Porcas, and Readhead
3C268.4	38	Zensus and Porcas
3C270.1	178	Hough and Readhead
3C275.1	135	Hough and Readhead
3C309.1	2350	Wilkinson, et al.
3C334	165	Hough and Readhead

Table 4

Correlation Tests--Full Redshift Range

Variables	With Compact Triples		Without Compact Triples	
	r	P	r	P
L, z	-0.531	0.01	-0.576	0.01
log R, z	-0.240	0.25	-0.370	0.10
C, z	0.235	0.30	0.238	0.40
log R, log L_V	-0.260	0.20	-0.231	0.30

Table 5

Correlation Tests--Low Redshift Sample

Variables	With Compact Triples		Without Compact Triples	
	r	P	r	P
L, z	-0.369	0.15	-0.327	0.25
log R, z	0.066	0.80	0.043	0.90
C, z	0.009	0.95	-0.386	0.20
log P, L	-0.395	0.10	-0.362	0.20
log P, log R	0.084	0.75	0.020	0.95
log P, C	0.047	0.85	-0.307	0.30
log R, L	-0.716	<0.01	-0.632	0.01
C, L	-0.603	0.01	-0.309	0.30
C, log R	0.635	0.01	0.315	0.30

Table 6

Correlation Tests-- High Redshift Sample

Variables	With 3C43		Without 3C43	
	r	P	r	P
L, z	0.041	0.90	-0.165	0.70
log R, z	-0.548	0.15	-0.602	0.15
C, z	-0.510	0.40	-0.626	0.35
log P, L	0.437	0.30	-0.070	0.90
log P, log R	-0.866	0.01	-0.605	0.15
log P, C	-0.844	0.05	-0.139	0.85
log R, L	-0.663	0.05	-0.364	0.40
C, L	-0.557	0.35	0.048	0.95
C, log R	0.964	0.01	0.760	0.25

Figure Captions

Note: On all correlation plots, "classical doubles" are represented by filled dots and "compact triples" by crosses. On all distribution plots, "compact triples" are cross-hatched.

Fig.1 - Projected linear size, L, vs. redshift, z, for the full redshift sample.

Fig.2 - Extended structure power, P_e, vs. projected linear size, L, for the low redshift sample.

Fig.3 - Distribution of projected linear size, L, for the low redshift sample for: (a) L_{90}=330 kpc and (b) L_{90}=0-330 kpc. Solid lines represent observations, dashed lines theory.

Fig.4 - Distribution of normalized CC strength, R, for the low redshift sample for: (a) γ=5 and R_{90}=0.01, (b) γ=5 and R_{90}=0.01-0.07, and (c) γ=2 and R_{90}=0.01-0.03, this time excluding the compact triples. Solid lines represent observations, dashed lines theory.

Fig.5 - Normalized CC strength, R, vs. projected linear size, L, for the low redshift sample.

Fig.6 - Normalized CC strength, R, vs. optical luminosity, L_V, for the full redshift sample.

Fig.7 - Curvature, C, vs. projected linear size, L, for the low redshift sample.

Fig.8 - Curvature, C, vs. normalized CC strength, R, for the low redshift sample.

Fig.9 - Distribution of curvature, C, for: (a) the low redshift sample and (b) the high redshift sample.

Fig.10 - Probability distribution of apparent transverse velocity, β_{app}, for:

(a) γ=1-3 and θ=0-90°

(b) γ=4-6 and θ=0-90°

(c) γ=1-3 and θ=0-60°

(d) γ=4-6 and θ=0-60°

Fig.11 - Probability distribution of apparent curvature, ΔPA, for:

(a) ξ=2° and θ=0-90°

(b) ξ=5° and θ=0-90°

(c) ξ=10° and θ=0-90°

(d) ξ=2° and θ=0-60°

(e) ξ=5° and θ=0-60°

(f) ξ=10° and θ=0-60°

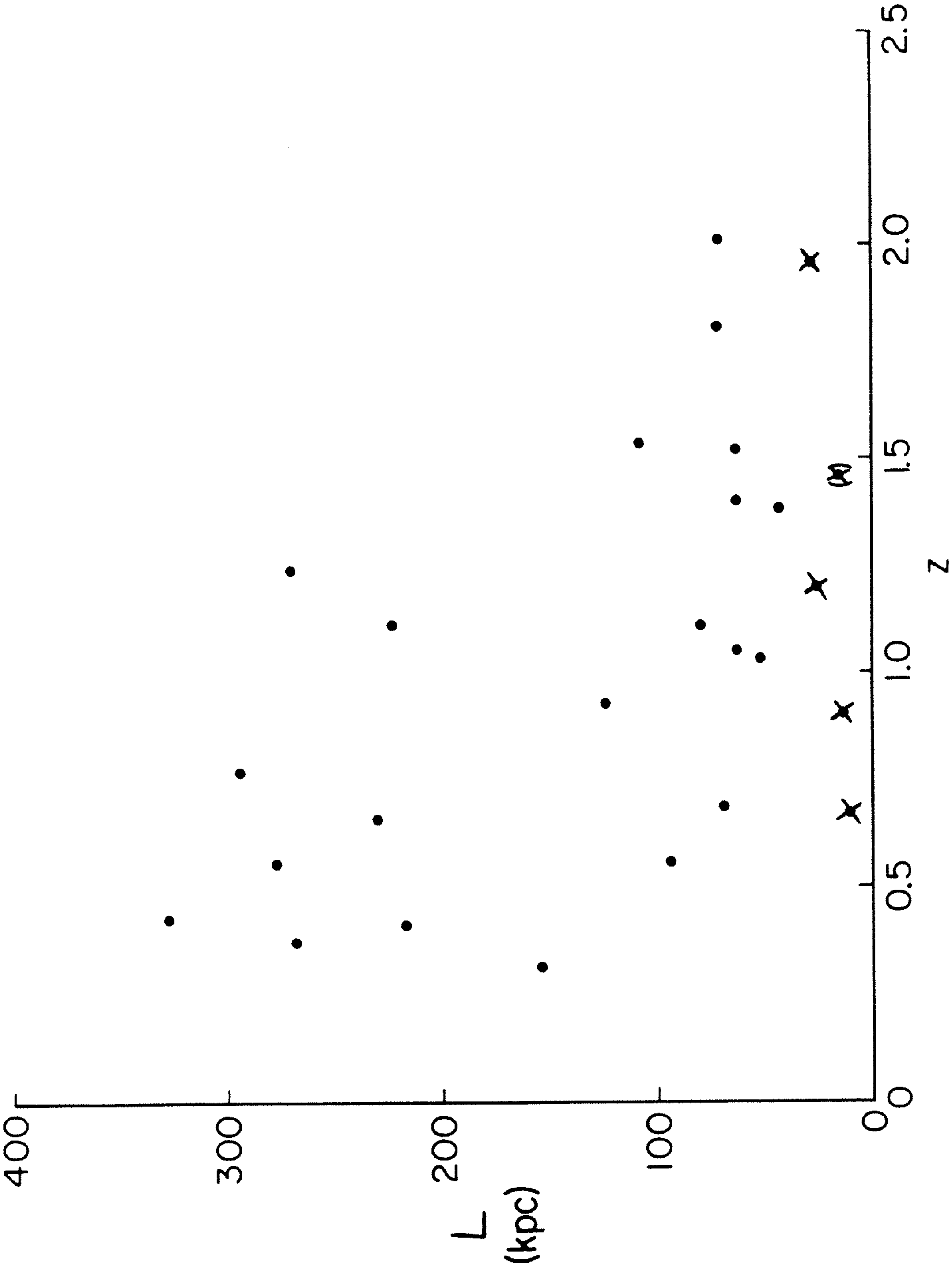

Figure 1

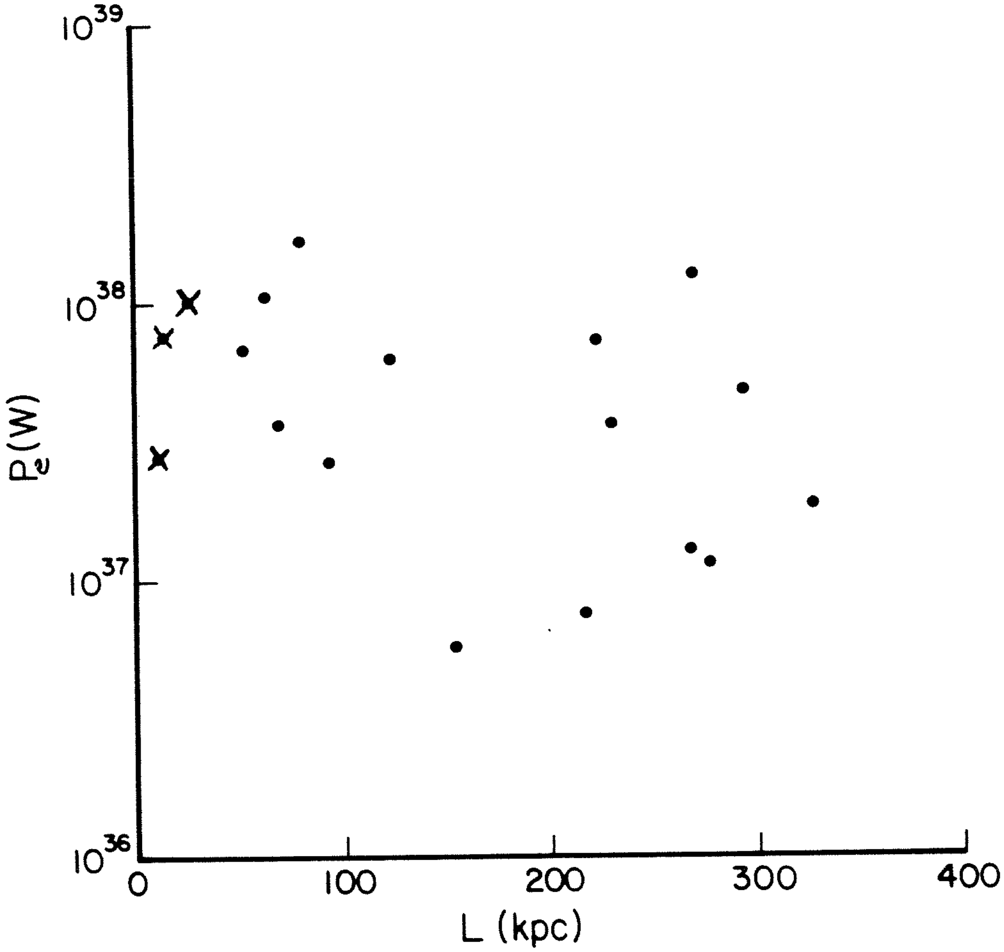

Figure 2

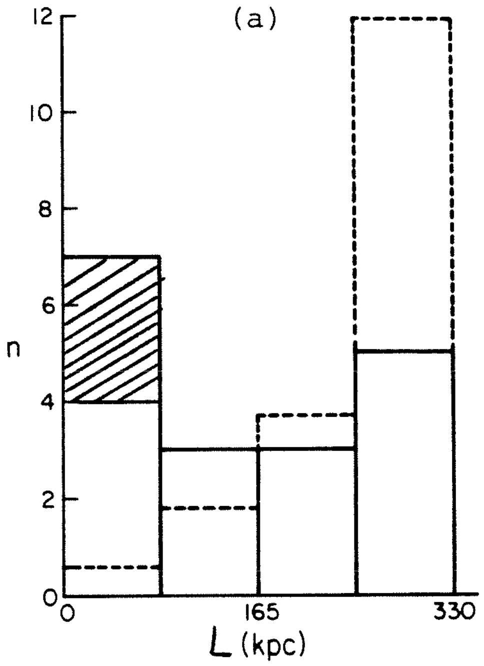

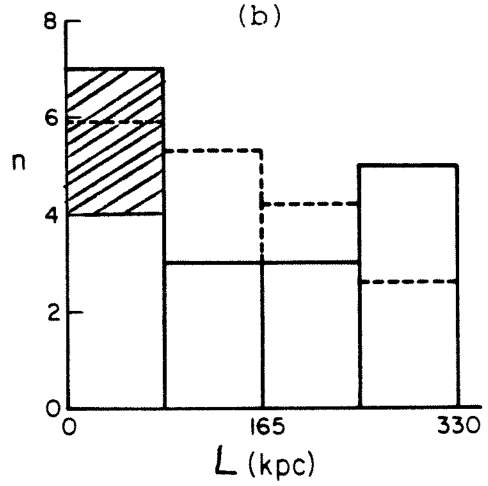

Figures 3a and 3b

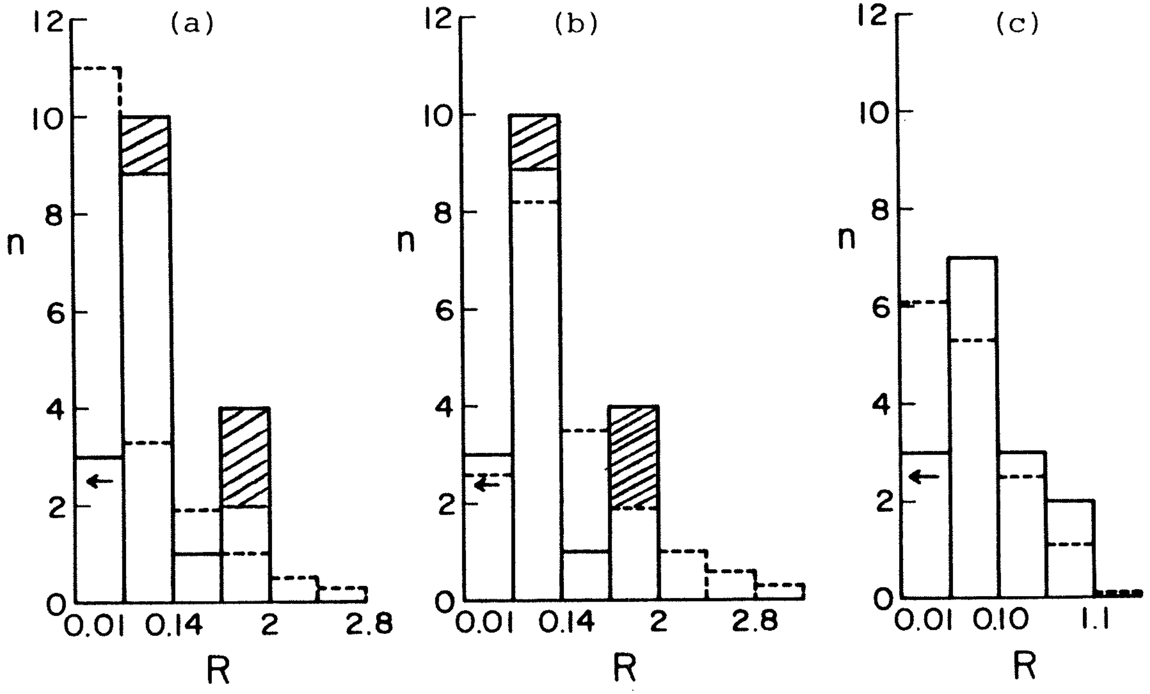

Figures 4a-c

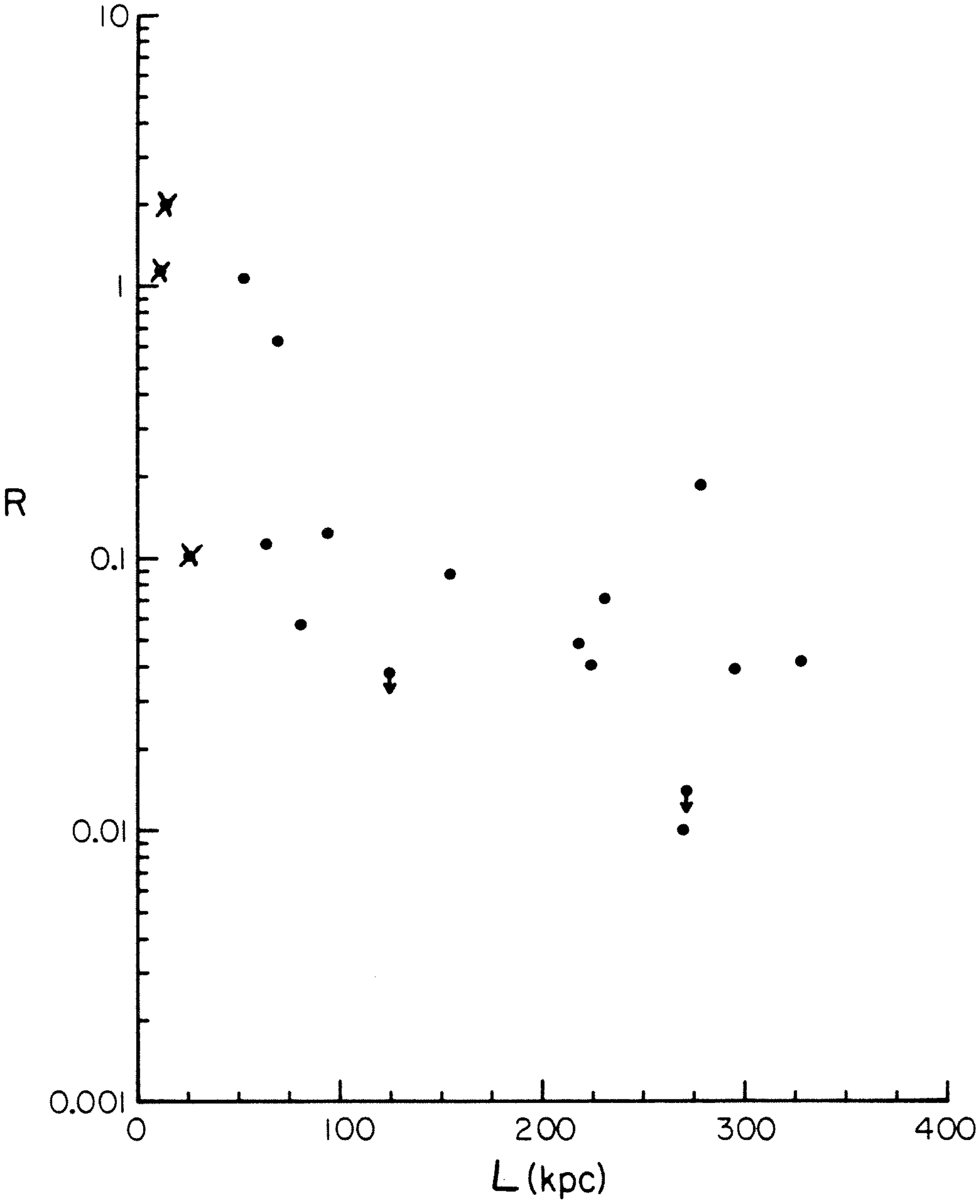

Figure 5

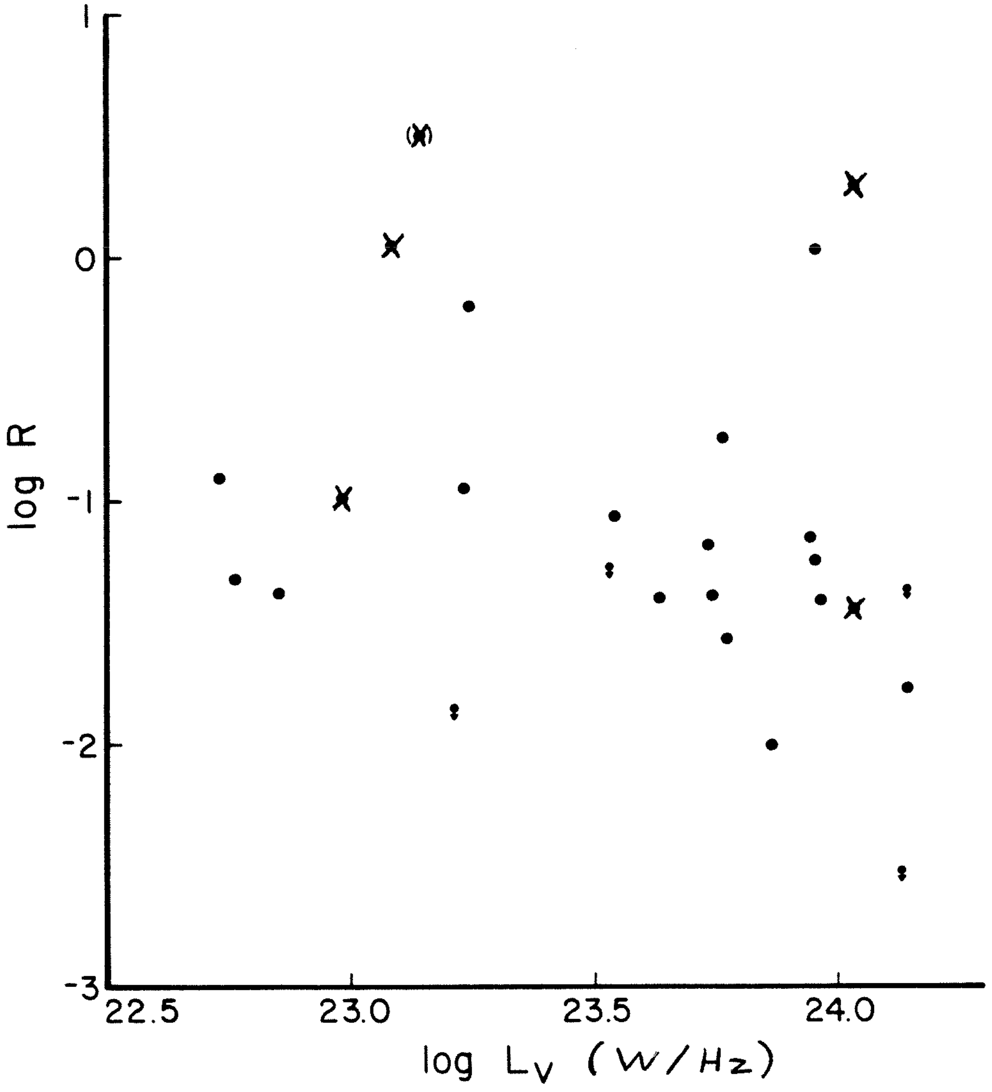

Figure 6

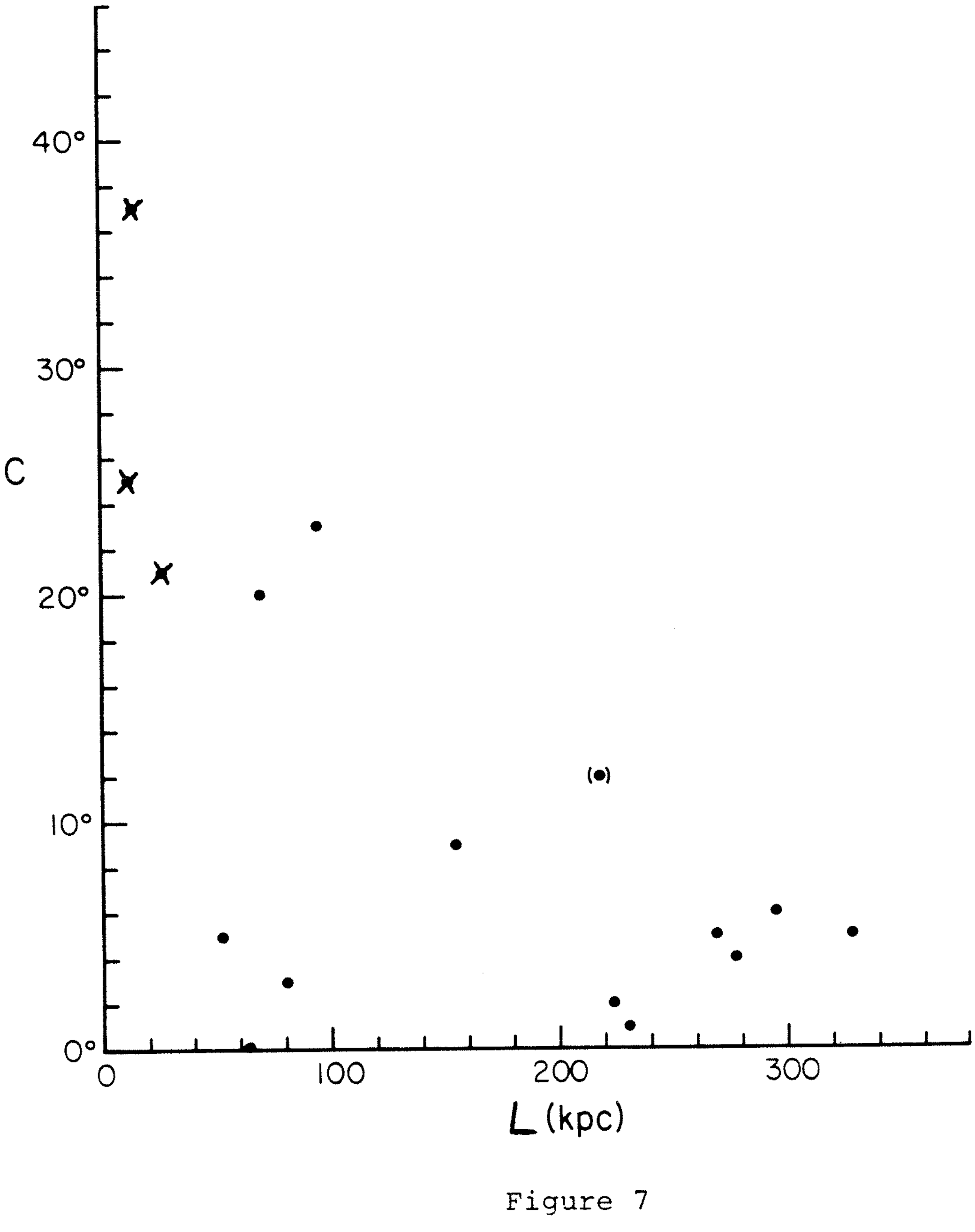

Figure 7

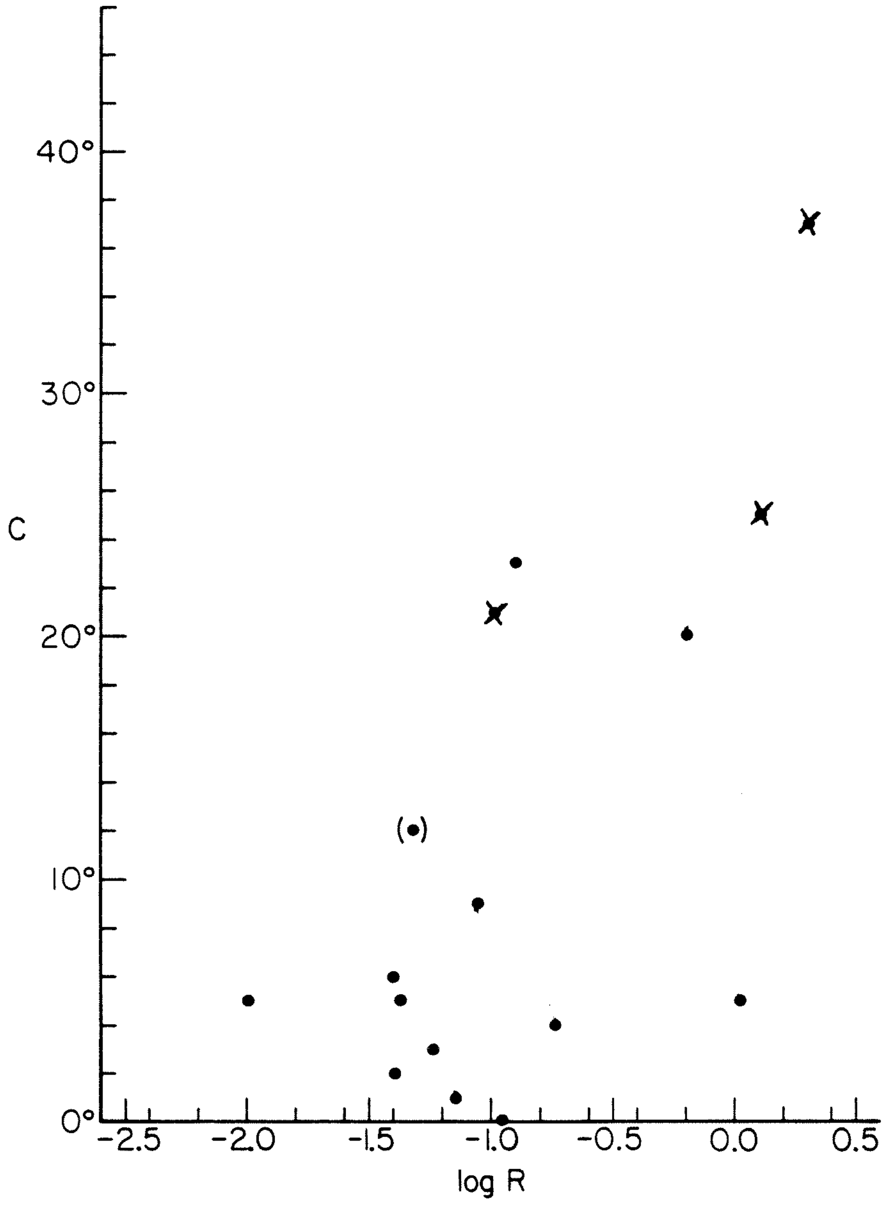

Figure 8

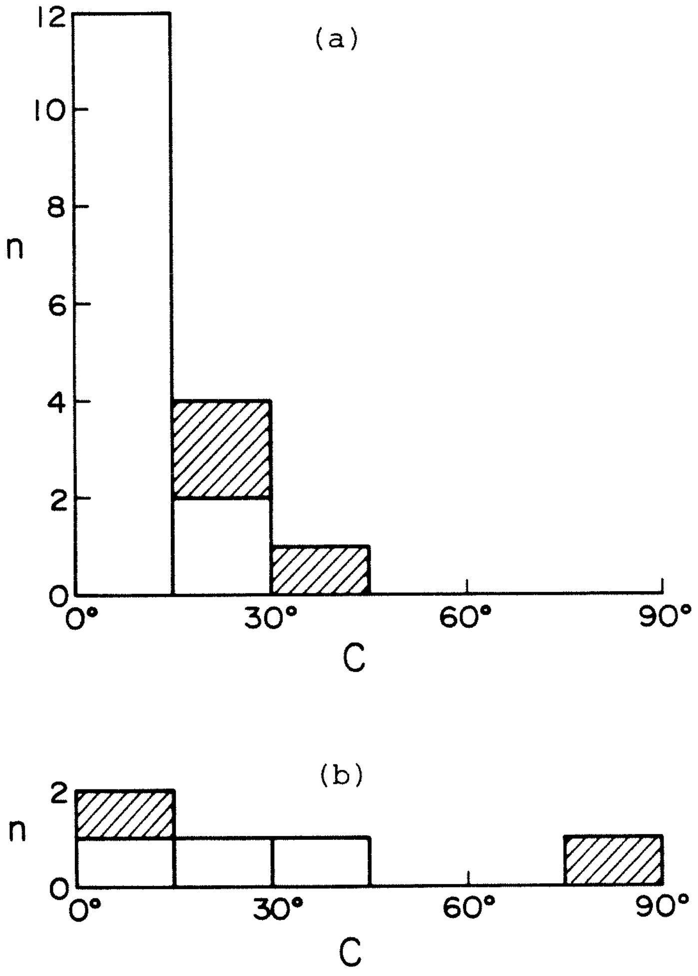

Figures 9a and 9b

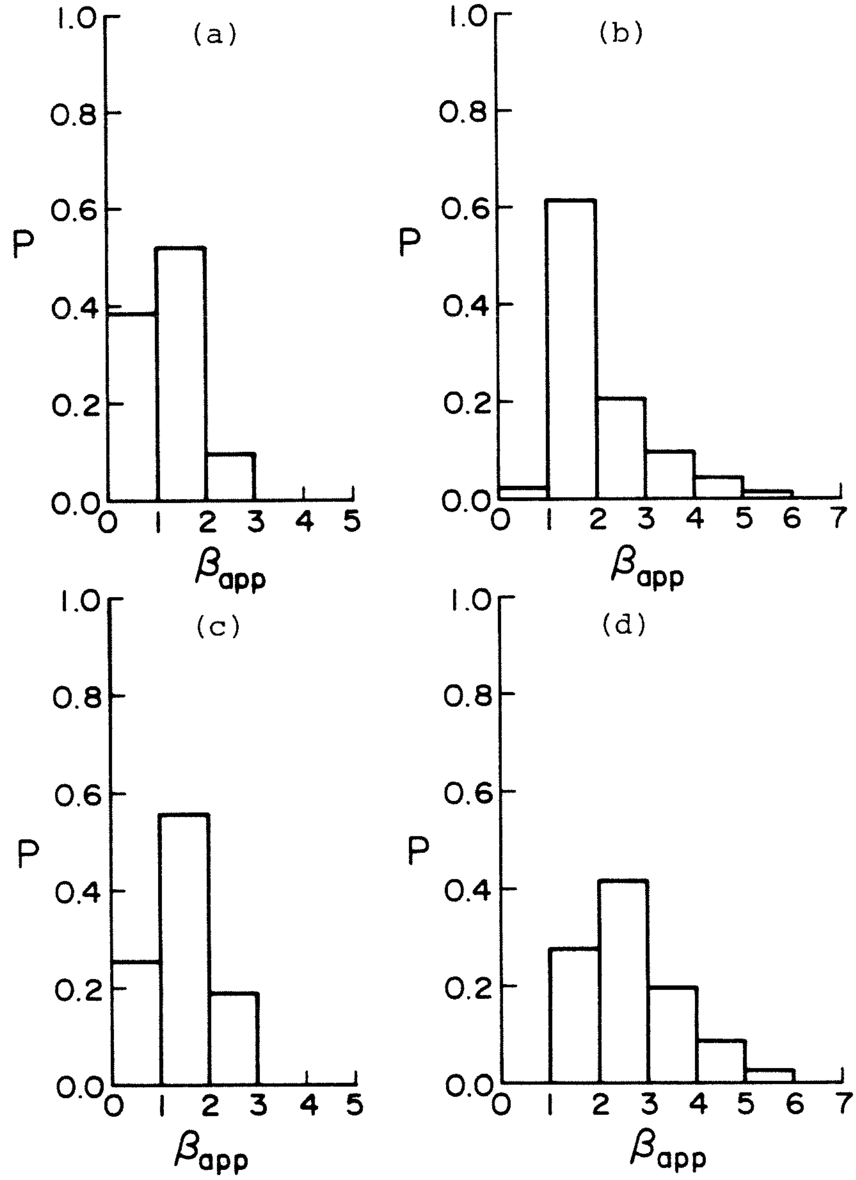

Figures 10a-d

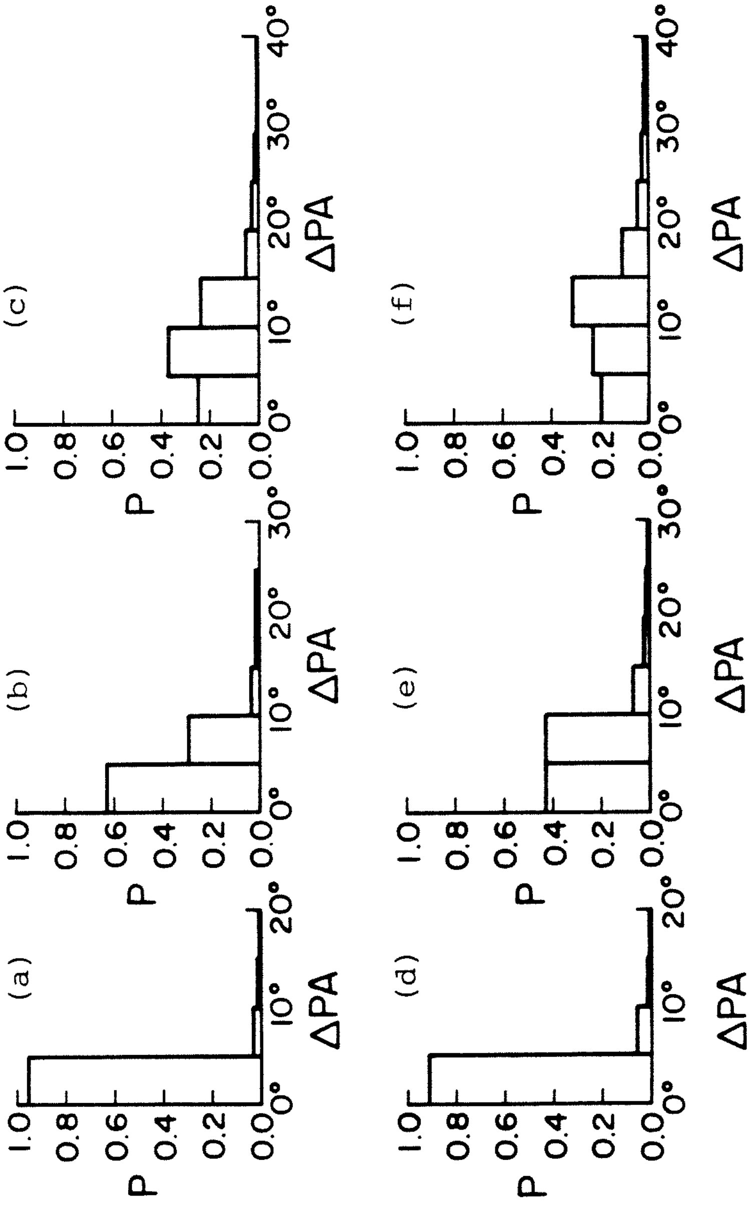

Figures 11a-f

CHAPTER 2

10.7 GHZ VLBI OBSERVATIONS OF THE CENTRAL COMPONENTS OF DOUBLE-LOBED QUASARS

Summary

We present Mark III VLBI maps of the central components (CCs) of six double-lobed quasars from the complete sample defined in Chapter 1. The CCs exhibit a double or extended structure on the ~parsec scale, which is well aligned with >~kiloparsec-scale features. These structures may be interpreted as "core-jets," with the VLBI jet lying on the same side of the compact core as the large-scale jet. No two-sided VLBI jets are found. Several objects contain two components with distinct peaks which are excellent candidates to monitor for superluminal motion.

I. Introduction

In Chapter 1, we defined a complete sample of double-lobed quasars which have central components (CCs) well suited for study by VLBI. The complete sample was chosen to be largely free of orientation bias, to facilitate statistical tests. In selecting a subsample of objects with CCs strong enough for VLBI study, a bias may be introduced in favor of sources aligned close to the line-of-sight, but this can be allowed for in any specific model to be tested. On the relativistic beaming model, for example, the distribution in θ (the angle to the line-of-sight) for the complete sample is known, and the CC strength normalized to the extended emission, R, can be used as a measure of orientation so that we can still estimate the biassed θ distribution for the VLBI subsample.

In particular, we have seen that a subsample can be defined which contains the n CCs with R above some minimum value, R_{min}. Starting from a complete sample of N objects with random orientations, it is then plausible that the n objects in the subsample are oriented between 0^{o} and θ_{max} = arccos (1-n/N). As an example, a subsample with n=N/2 would be expected to represent that portion of the complete sample with objects oriented between 0^{o} and 60^{o}. We have shown in Chapter 1 that a modest dispersion in intrinsic CC strength is required for consistency with beaming. This reduces the precision of determining the biassed θ distribution, since R_{min} does not define a unique θ_{max}. Nevertheless this method still provides a reasonable estimate of the distribution for the complete VLBI subsample.

As discussed in Chapter 1, it is not certain that compact triple objects with angular size <~ 5" are "classical doubles" viewed at very small angles to the line-of-sight. Furthermore, 3C216 and 3C309.1 of the low redshift sample ($z < 1.3$) are already included in other VLBI observing programs (Pearson and Readhead 1984a; Kus, Wilkinson, and Booth 1981). Therefore, we define here a subsample composed of the seven sources with the strongest CCs in the low z sample of fifteen clear "classical doubles." These seven sources--3C207, 3C212, 3C245, 3C249.1, 3C263, 3C275.1, and 3C334--form a subsample containing all the CCs with $S_{CC} > 75$ mJy at 5 GHz and $R \gtrsim 0.07$. This group of objects is thus both very practical for Mark III VLBI observations and well defined in terms of its θ distribution, and therefore an excellent sample on which to begin a thorough series of VLBI observations. The subsample is listed in Table 1, including the pertinent source data from Chapter 1.

In this chapter, we present the results of brief pilot observations of all seven objects and full (u,v)-track mapping observations of six objects at ~0.5 milliarcsecond (mas) resolution. These observations were made with a five-station VLBI array at 10.7 GHz using the Mark III recording system (Rogers, et al. 1983). Brightness distributions are determined by three different methods--model fitting, hybrid mapping, and maximum entropy mapping. The basic ~parsec-scale morphology of the CCs is discussed, as is its relationship to >~ kiloparsec-scale structure. We identify prime candidates to monitor for structural variations, based on the observed ~parsec-scale morphology and flux density variations.

II. Observations and Processing

The observing program consisted of two stages. The first stage was a brief pilot survey of all seven objects, in which a few short scans were made on each source to search for signs of structure in the visibility data. The second stage was a series of full (u,v)-track observations to map each source, in a priority order based on the amount of structure revealed in the pilot survey.

In all cases, the observations were made by arrangement with the U.S. VLBI Network and the Max-Planck-Institut für Radioastronomie. A five-station interferometer was used, and the telescope locations and typical properties for these experiments are given in Table 2. The observing frequency was 10.7 GHz (λ=2.8 cm), and data were recorded with the Mark III system.

The pilot observations of the seven objects in the complete VLBI subsample were made on 4-5 October 1981 and 19 June 1983. The CC of an eighth source, 3C154, was included in the first experiment because it was known to be relatively strong. 3C207 and 3C212 were reobserved for several scans in the second experiment because we found only very weak evidence of any resolved structure in the initial brief observations. The Mark III system was used at full bandwidth (56 MHz). A few short scans of thirteen minutes each at well-spaced hour angles were made on each source. (A minimum of ~five scans for a five-station experiment is required to obtain enough (u,v) samples to clearly reveal any structure, and to roughly constrain the size and position angle of a single gaussian or double point source model.)

The full (u,v)-track mapping observations were made between October 1982 and August 1984; the journal of observations is given in Table 3. The February 1983 session on 3C245 and 3C249.1 was hampered by severe weather conditions at Effelsberg and Green Bank. Despite the total loss of Effelsberg for 3C245, it was still possible to map this object with the remaining four stations. We were unable to map 3C249.1, and thus the observations were repeated in February 1984.

Model fitting to the February 1983 data is discussed below together with the results of the pilot observations. The observations of 3C263 were made in a collaboration with J.A. Zensus and R.W. Porcas. Mark III recording was done at either full or half bandwidth (56 or 28 MHz) as indicated in Table 3. Because of the time required for tape rewinding and changes, the (u,v) tracks are not continuous. The duty cycle for Mode A was typically just below ~50 per cent but was often higher for Mode B. Observations usually spanned ~twelve hours.

The data were correlated on the Mark III processor at Haystack Observatory (Whitney 1982), except for 3C263, for which the correlation was done on an identical processor at the Max-Planck-Institut für Radioastronomie. Fringe-fitting was done on the HP-1000 computer at Haystack (or MPIfR). A coherent intergration time, τ, was chosen for each experiment which provided adequate signal-to-noise ratios while avoiding significant amplitude reduction due to coherence losses (see Table 3). An export tape containing the correlation coefficients and phases was then prepared to transfer these data to a VAX computer at the California Institute of Technology for further reduction.

III. Data Reduction

A. Editing and Calibration

The uncalibrated data were edited to delete obviously bad points. In those cases where the signal-to-noise ratios at times dropped below ~7, a small correction was applied to the correlation coefficients to remove the positive bias which exists at low SNR.

The correlation coefficients were calibrated using the system temperatures, peak sensitivities, and gain curves for each telescope, following Cohen, et al. (1975). We checked the calibration, when possible, by inspection of (near)-crossing points in the (u,v) plane, and by comparison of the amplitudes on baselines of similar length for the barely resolved sources. (No really suitable, unresolved calibrator sources are available at 10.7 GHz).

For the pilot observations, we could not make very reliable checks of the calibration due to the limited amount of data. In addition, there were large gain uncertainties for the equatorial-mount telescopes with declination-dependent gain curves, especially in October 1981. As a result of these problems, absolute calibration errors of between 10 and 20 percent were added in quadrature with the noise errors for the amplitudes in these pilot survey data. Scale corrections to the station gains were calculated using S.C. Unwin's implementation of the Cornwell and Wilkinson (1981) method, AMPHI.

For the mapping observations, absolute calibration errors were not, in general, applied to the data. Scaling of the gains in the raw calibration with AMPHI usually resulted in <~ 5 percent adjustments. The noise errors range from ~1-2 mJy for Effelsberg-Green Bank to ~10-20 mJy for Haystack-Fort Davis for a thirteen-minute tape, and are typically <~ 5 mJy for most baselines. Because of appreciable scatter in the 3C245 amplitudes in February 1983, a 5 percent absolute calibration error was applied to smooth the data. The gain curves were well determined for most of the telescopes. However, in some cases difficulties were encountered with the Green Bank gain curve. In these instances, AMPHI was used to alter the Green Bank gains by optimizing the fit of the data to a model which already fitted the data for all the other stations very well.

B. Methods of Recovering Brightness Distributions

We have used three methods to determine the radio brightness distributions of the central components--model fitting, hybrid mapping, and maximum entropy mapping.

Models consisting of elliptical Gaussian components were fitted to the amplitudes and closure phases, using R.S. Simon's algorithm to minimize the reduced chi-square agreement factor between the model and the data. Errors were assigned by incrementing a given model parameter by increasing amounts away from its best-fit value, and then reoptimizing all other model parameters, until it was no longer possible to obtain an acceptable fit. (The reoptimization step was not done systematically for the crude pilot survey models, for which the large error bars lead to conservative model errors anyway). A fit was judged to be unacceptable when clear, systematic discrepancies developed between model calculations and the data. The percentage change in agreement factor from its best-fit value at the point where a fit was deemed unacceptable is remarkably consistent from one model to the next. This suggests that it is quite possible to visually assign errors in a uniform and statistically valid fashion, although it is difficult to attach a precise significance level to these errors. They are likely greater than 1σ, but probably not larger than $\sim 2\sigma$. A detailed discussion of this error analysis is given in Appendix A.

Hybrid mapping (Readhead and Wilkinson 1978) was done using a few iterations of the cycle beginning with AMPHI for amplitude and phase corrections, followed by Fourier inversion and CLEANing of the dirty map. The field of view is restricted to a width of <~ 10 mas by the shortest baseline. We made maps with both point source and two-component starting models, in order to compare the results and ascertain if any significant differences arose on the final maps due to the choice of starting model. The rms noise levels are ~1-<~2 times those expected on the basis of the input data errors. Since the structures are very compact (see Section IV), it was generally necessary to convolve the CLEAN delta-functions with a beam substantially smaller than the synthesized beam, in order to clearly illustrate the presence of individual components within the conventional beam size. "Super-resolution" by factors <~2 can be done reliably given adequate signal-to-noise ratio and (u,v) coverage (e.g., Pearson and Readhead 1984b), but if it is not done with great care one can get misleading results.

Finally, we performed maximum entropy mapping (e.g., Gull and Daniell 1978) using S.F. Gull's VLBMEM program. Several tens of iterations were typically required to reach convergence. This technique maximizes the entropy of the image, subject to the constraint of fitting the data. MEM can, in principle, produce super-resolution by taking advantage of the strong signal-to-noise ratio in high brightness regions.

Because the structure is mostly within the beam size, it is very important that all three of these methods be applied for each source, and the results carefully compared to make the best possible deductions about the true source brightness distributions. Details of the reliability of super-resolution are discussed in Appendix B.

IV. Results

A. Pilot Observations

The results of model fitting to the brief scans in the pilot survey are given in Table 4. The large errors reflect the poor calibration and sparse data and take into account model differences between fitting to the data with and without gain corrections. It should also be noted that single Gaussian or double point source models were assumed, since the data did not warrant models of greater complexity. Therefore, even allowing for the large errors, these models should be interpreted only as being indicative of source structure; the value of any particular parameter should not be regarded as being too significant.

Sufficient data are available to determine fairly reliable position angles for the elongated structures in the CCs of three objects: 3C249.1, 3C263, and 3C334. The June 1983 data for 3C207 also permit a determination of its position angle, but the associated error is very large. All four of these objects could be modeled as doubles with separations of ~1/2 mas. We could not determine position angles for any of the other three objects, but 3C212 and 3C245 are partially resolved. Non-zero closure phases point toward a very slight amount of asymmetry for 3C212 and a somewhat larger degree of asymmetry for 3C245; these asymmetries are not represented in the single Gaussian models. Only one scan was made on 3C275.1, which basically just confirms that the CC can be detected at the ~0.1 Jy level.

In 3C154, there is a highly resolved CC. Non-zero closure phases indicate asymmetric structure, but nothing can be deduced from the present data about even its crude form or alignment. A three-component structure roughly aligned with the outer lobes has been observed by Barthel (1984).

Barthel (1984) has also shown the presence of resolved structure in all of these CCs except 3C249.1 and 3C275.1. The angular sizes he found for the CCs are consistent with the values determined here.

We have reason to be confident in at least the qualitative aspects of the derived VLBI structures. The correlated flux densities and closure phases for 3C212 are consistent with its being a barely resolved source, while other objects tend to show increasing variations in both correlated flux density and closure phase as the derived structure becomes more complicated (i.e., in going from single Gaussian to double structures).

A comparison of the model flux densities at two epochs for three objects indicates that 3C207 may have undergone a variation at the ~1 σ level ($\Delta S \sim 0.1$ Jy in 1.7 years), while 3C212 and 3C249.1 have remained constant on similar timescales, within the errors.

The fact that the models generally contain ~75 per cent of the mean correlated flux density on one of the shortest baselines (Haystack-Green Bank or Fort Davis-Owens Valley) suggests that there may be structure on the scale of a few mas, which has not been accounted for in the models (see Table 5). However, it is also possible that the models are so crude that they do not correctly account for all the flux density, even if it is all indeed located on the <~ 1 mas scale.

It is of more importance and interest that the maximum visibilities on the shortest baselines range from ~0.3 to ~1, typically being ~0.75 (see Table 5). Since the total CC flux densities are from maps with ~arcsecond-scale resolution, this indicates that at least some objects have significant structure on scales between a few mas and ~1 arcsecond. 3C212 and 3C263 appear to have most of the flux density in the VLBI core. The visibilities on the lower end of the range may well be particularly low due to variability of the CCs, especially in 3C207 and 3C245, for which variability has clearly been established (see part B), and an estimate of the maximum CC flux density has been used in calculating the visibility. But in two other objects which have been monitored and are believed to be constant--3C249.1 and 3C334--it is evident that ~25 per cent of the flux density emanates from regions of intermediate size. (No careful flux density monitoring has been reported for 3C275.1, with a similar maximum visibility.) Yet even in these objects, a very large fraction of the total flux density originates in a compact region less than a few mas in size deep within the ~arcsecond CC. Swarup, Sinha, and Hilldrup (1984) have previously noted that quasar CCs are often slightly resolved at arcsecond resolution.

B. First-epoch Mapping Observations

Each of the six objects in the pilot survey which possessed at least some signs of resolved ~mas structure was reobserved with full (u,v) tracks to permit mapping. The only object in the low z complete subsample which we have not mapped is 3C275.1. The general results common to all objects from model fitting, hybrid mapping, and MEM mapping are presented and compared below. Particular results for each object follow. Tables 6-11 summarize the component parameters derived using the three different techniques.

1. General Results

On hybrid maps presented at the conventional resolution, each object is slightly resolved in one direction (see Figures 1a-f). This resolved structure appears as a well-defined extension for the objects at high declination, and it is perceptible as the broadest tapering of the contours for those at low declination. However, in order to probe the structure on smaller scales, and to make a quantitative assessment of the degree of alignment of these extensions with large-scale structures, it has been necessary to resort to further techniques.

The hybrid maps consist of a set of CLEAN delta-functions convolved with a restoring beam, which is an elliptical Gaussian whose dimensions are taken from the full width at half maximum of the synthesized dirty beam. We can attempt to determine the structure on a somewhat smaller scale than this conventional beam simply by choosing a smaller restoring beam. Thus, keeping in mind the inherent dangers of this practice referred to above, the super-resolved (SR) hybrid maps are presented in Figures 2a-f. The structures seen on the conventional maps are now almost all resolved into two components, with distinct peaks appearing in both components in some cases. In these latter cases, examination of the CLEAN delta-functions shows that they are indeed located mostly within two distinct clumps. The components are of unequal strength, with flux density ratios ~1.5-10. Hereafter, we shall call the stronger component "A" and the weaker component "B." B usually appears slightly resolved in comparison to A. No objects are found with extensions in opposite directions on both sides of the core at the limits of the present maps. For all but one of the objects, a reliable position angle of the source axis can be derived. In those cases with two distinct peaks, a separation of B from the core can be measured; these are nearly always <~ the conventional beam size. The errors on the parameters in Tables 6-11 are standard deviations on the mean of several measurements from mapping runs with different starting models, different sets of baselines, and with and without gain corrections. This method may tend to underestimate errors when the solutions are not sensitive to the circumstances of the different runs.

Two more fully independent deconvolutions have been made of the data. Model fitting with two Gaussian components is especially important for providing confirmation of the relative position and orientation of A and B. The errors determined from model fitting are also probably the most consistent and appropriate.

More importantly, MEM mapping confirms the presence and nature of the double structure in each case (see Figures 3a-f). Where very distinct components are revealed on the SR hybrid maps, MEM produces distinct components; where component B is barely resolved from the core and lacks a pronounced peak on the hybrid maps, similar features show up using MEM. The separations of the peaks are generally in good agreement with those from the hybrid maps. The ratio of peak flux densities of A relative to B is systematically higher for MEM images; this may be interpreted as being due to MEM's ability to achieve authentic super-resolution, where the greater signal-to-noise ratio for the stronger component permits superior resolution and thus, for a very compact component, results in a higher observed peak surface brightness. MEM also tends sometimes to make the weaker components more elongated along the source axis.

The fits to the data, especially the amplitudes, are not as spectacularly good as those generally obtained in hybrid mapping but are still impressive. This is due partly to the difficulty in calculating the visibilities of the Fourier components from the MEM image (Gull), and partly to the fact that the present MEM algorithm does not have a gain adjustment option. MEM can also produce spurious features at window edges when these are employed to emphasize the longest spacings and obtain the best fit possible to the most compact structure.

2. Specific Results for Each Object

3C207

The structure is very compact, with a weak extension from the core visible on both the SR hybrid and MEM maps. While a secondary peak is just distinguishable on the hybrid map, MEM shows a smooth extension in the same orientation. The data can be fitted well by a double Gaussian model. The relative position of A and B is similar for the model fitting and hybrid mapping. There is evidently structure on the ~10 mas scale that we have not accounted for here, which reveals itself on the Haystack-Green Bank baseline. We believe that the integrity of the data has not been compromised, despite the proximity of the sun during the experiment (approximately 7o distant), since no significant amplitude reduction occurred for short enough coherent averages (60 seconds). The CC has possibly varied over the three observing sessions from 1981 to 1984 by ~0.1 Jy; Wardle (1984) has monitored the CC at 15 GHz and observed a drop of ~0.17 Jy between January 1983 and December 1983.

3C212

This object has been the most stubborn of all in revealing its structure. Both modelfits from the pilot survey showed a barely resolved core. The core on both the SR hybrid and MEM maps appears to be slightly broader on the western side than on the eastern side. The parameters for a two-component model are hard to constrain. Most of the CC flux density is in the compact core. This object was observed when it was a little over 3° from the sun; we have confidence in the results, using very short coherent averages, since the amplitudes using 8 second and 16 second coherent averages are in good agreement. No flux density variations are evident from the VLBI data; Hine and Scheuer (1980) found the CC to be constant at 5 GHz over ~10 years, and Wardle (1984) saw no variations at 15 GHz over ~1 year.

3C245

Despite the loss of the Effelsberg telescope, sufficient resolution was obtained to distinguish a weak secondary component ~1 mas from the core on the SR hybrid map. The model fitting and MEM results are in basic agreement with the hybrid map; all three methods, however, indicate that the position of B is poorly defined. There is also clearly structure on a scale of ~10 mas which contributes to the visibility on the short Haystack-Green Bank baseline that has not been accounted for here. This is confirmed in a recent 18cm VLBI map by Barthel (1986). There has been a dramatic increase in correlated flux density between 1981 and 1983, as measured in the total flux density monitoring at 10.8 GHz of Seielstad, Readhead, and Pearson (1983). Aller and Aller (1985) also saw significant variations in total flux density at 8 GHz over ~1 year, and Wardle (1984) has measured a drop of ~0.24 Jy at 15 GHz in the CC from January 1983 to December 1983. The structural changes associated with this outburst seen in subsequent observations are discussed in Chapter 3.

3C249.1

A loss of data for a few hours at Owens Valley left a gap on the long Effelsberg-Owens Valley baseline precisely where a minimum in the amplitude may have occurred. The SR hybrid map shows that CLEAN has produced a secondary peak in component B, whereas MEM finds a core with a very smooth extension. Model fits with two circular Gaussians and with a combination of a circular Gaussian and an elliptical, "jet-like" Gaussian extension both give good fits to the data, so it is not really possible to choose between these two representations of the source structure. The position angle of the extension, however, is well defined and the values from all three methods agree very well. These data confirm the pilot survey result that ~25 percent of the CC flux density lies on scales between a few mas and ~1 arcsecond. The VLBI observations and the 5 GHz monitoring of Hine and Scheuer (1980) show no variations over ~3 years and ~10 years, respectively; Wardle (1984) found the CC to be constant at 15 GHz over ~1 year.

3C263

A distinct double structure is present on both the SR hybrid and MEM maps, which is well represented by a model consisting of two circular Gaussian components. All three methods yield excellent agreement on the separation and position angle of B relative to A. Essentially all of the CC flux density is accounted for on the ~1 mas scale. The VLBI data and the monitoring of Wardle (1984) at 15 GHz show no evidence for significant flux density variations on a ~1 year timescale.

3C334

A double structure is evident on the SR hybrid and MEM maps, which is well represented by two circular Gaussian components. The relative position of the two components is fairly well determined by all three methods. As was found in the pilot survey, ~20 percent of the CC flux density is unaccounted for on scales of <~ a few mas and must come from scales greater than this. Hine and Scheuer (1980) classified the CC as constant at 5 GHz over ~10 years; Wardle (1984) found it to be constant at 15 GHz over ~1 year, in agreement with the VLBI results here.

V. Discussion

The high-sensitivity, high-resolution VLBI observations presented above have revealed detectable structure on a scale of <~ 1 mas (i.e., <~ a few parsecs) in the central components of six double-lobed quasars in the complete VLBI subsample. The fact that these objects can be resolved is significant, in that they are far weaker than the cores in flat-spectrum, core-dominated quasars, yet exhibit structure on similar size scales. This provides a basis for comparisons of the ~parsec-scale morphology between the CCs of lobe-dominated objects and core-dominated objects at high redshift. The CCs may have been unresolved if their far weaker emission corresponded to their having much smaller structure. Conversely, if the weak emission had been largely spread out on scales up to a few kiloparsecs, then there would have been little flux density remaining to detect on VLBI scales. As it turns out, there is appreciable emission on intermediate scales in some of these objects, indicating a continuity of structure on all scales, but most of the emission is from a compact core.

The structure in each object consists of two components (A and B), with both components containing clearly defined peaks in three out of six objects. The stronger component, A, is typically a factor of a few stronger than the weaker component, B. B generally appears to be slightly more resolved than A, and the MEM maps sometimes suggest that A is a high surface brightness core and B is elongated along the source axis. This is consistent with the interpretation that these are "core-jet" objects similar in morphology to the compact cores in the flat-spectrum, core-dominated sources. In the absence of spectral information and better resolution, we cannot firmly establish which component might be the compact, flat-spectrum core and which the extended, steep-spectrum jet. However, it is certainly plausible that the weaker components correspond to the jets.

The fact that distinct components are often embedded in the jets in these quasars, as well as in those studied by Zensus (1984), is very fortunate for pursuing tests of relativistic beaming. The four radio galaxy CCs mapped by Linfield (1981) contain smooth, one-sided jets without distinct features which facilitate proper motion studies. It was not clear before these new surveys that the situation would be any different for "classical double" quasars, but the frequent occurrence of discrete double structures now makes it clear that we will be able to conduct a search for proper motions, if any, in these objects. One should also keep in mind, however, that these images are at the very limit of resolution; it may be that the apparent double structure is a result of our inability to resolve multiple, exceedingly compact components.

The VLBI structure is generally aligned fairly well with compact features in the outer jets and lobes on the >~ kiloparsec scale (see Table 12, Figures 4a-f). The large-scale jets exhibit complex structure out beyond a few kiloparsecs, often with a pattern of knots superimposed on an overall gradual curvature. It is therefore most useful to consider ΔPA, the position angle difference between nuclear and outer structures, for the VLBI source axis and the innermost compact feature on the large-scale map (Knot A). This will indicate the curvature occurring over a physical size scale spanning ~three orders-of-magnitude in going from the near vicinity of the "central engine" to the general environment of the galaxy in which the quasar presumably resides.

The misalignments are $< 10^{o}$ for all objects in which the VLBI position angle is well determined. For 3C212, we cannot really define a VLBI position angle, but note that the western side of the core is slightly broader than the eastern side. Barthel (1984) has demonstrated the alignment in 3C263 previously. This good alignment between small- and large-scale structures adds further support to the conclusion of Zensus (1984), that the trend for alignment in symmetric, lobe-dominated objects at low redshift ($z < 0.1$) noted by Readhead, et al. (1978) continues for these objects at high redshift (z~0.3-1.0). Thus, high-redshift, symmetric objects do not exhibit the large misalignments which are often seen in high-redshift, core-dominated objects. This is consistent with the interpretation of Readhead, et al. (1978), that the large misalignments in core-dominated objects are due to projection effects in sources oriented very close to the line-of-sight. The symmetric objects are randomly oriented, and only a very small fraction of them would be expected to be oriented such that any small intrinsic bend would appear as a large observed misalignment.

We should point out that the apparent trend in these objects in which misalignment was correlated with CC strength and anti-correlated with projected linear size, based on our preliminary analysis of the pilot survey data (Readhead 1984; Hough and Readhead 1984), has not been borne out by the maps.

If we assume that there are projection effects at work and refer to the distribution of ΔPA for a biassed sample in Chapter 1, it seems that intrinsic curvatures of up to perhaps ~5° are required to account for the observed ΔPAs for these six objects. If a pressure gradient is responsible for bending a continuous small-scale jet, then it may be that the typical bulk Lorentz factor, γ, is constrained to be <~10, since it is difficult to bend a relativistic jet through an angle greater than $\sim 1/\gamma$ (e.g., Smith and Norman 1981). Another possible explanation is that the "central engine" spews out ejecta over a cone of half-angle ~5° (e.g., Scheuer 1984).

In addition to this good alignment, there is the fact that the weaker of the VLBI components lies on the same side of the strong component as the large-scale jet or dominant "hot spot" in all six objects. Since it is very likely that the stronger VLBI components are the compact cores in these asymmetric nuclear structures, the weaker components can be interpreted as small-scale jets lying on the same side of the "central engine" as the large-scale jets. This brings to ~twenty the total number of objects known to have small- and large-scale jets pointing in the same general direction (e.g., Jones, et al. 1986). Thus, it is very clear that the small- and large-scale asymmetries are related, and in particular that relativistic beaming may be at work on both scales (as noted in Chapter 1).

It is interesting to note that in three objects (3C207, 3C212, and 3C245) the brighter, more compact outer "hot spot" in the "jetted" lobe is further from the CC than the peak in the "unjetted" lobe. This is expected on the simple beaming model, assuming that the approaching component is the one with the observed jet. These sources are all of small projected linear size, so they may be oriented at relatively small θ and display strong beaming effects. In the other three sources (3C249.1, 3C263, and 3C334), however, the more compact outer "hot spot" (in all cases except 3C263 associated with a large-scale jet) is nearer the nucleus than the peak in the opposite lobe. Although these objects are of large projected linear size and therefore may not be expected to exhibit strong symptoms of beaming, there is no obvious explanation of why they should systematically show the opposite trend to the other three sources. Thus, there is no consistent trend for all six objects which is easily accounted for by simple large-scale beaming.

On the twin-jet model, the present VLBI maps provide lower limits to the jet/counterjet brightness ratio, J (using 3σ upper limits for the counterjets). These limits permit us to determine the maximum angle to the line-of-sight, θ_{max}, and minimum bulk Lorentz factor, γ_{min}, required to conceal from view a counterjet oppositely directed to, but intrinsically identical to, the observed jet:

$$\cos\theta_{max} = [J^{(1/2+\alpha)} - 1]/[J^{(1/2+\alpha)} + 1] = \beta_{min}\,; \qquad (1)$$
$$\gamma_{min} = (1 - \beta_{min}^2)^{-1/2},$$

where α is the spectral index (Linfield 1982). Even with the sensitivity of Mark III VLBI, the jet/counterjet lower limits are not very tight. The jets need be only mildly relativistic (γ <~1.5) in each case to hide the counterjet; even at θ_{max}, γ ~5 only is required (α=0.5 is assumed). Therefore, although no two-sided jets have been found here, the receding jets could easily escape detection. Thus, unfortunately, the present jet/counterjet brightness ratios do not permit us to draw any conclusions on the issue of one-sided versus two-sided ejection or about the bulk Lorentz factor.

If a two-sided VLBI jet is found later in the course of this survey, then this would demonstrate the existence of a two-sided ejection mechanism in at least some luminous radio sources. The best candidates are the two objects of largest projected linear size in the complete sample of Chapter 1 which also have CCs stronger than ~30 mJy: 3C47 and 3C175. If one of these large sources should be oriented at, e.g., $\theta = 70^\circ$, we expect that a counterjet would appear even if γ=10, for which we would predict a ~6:1 brightness ratio. On the other hand, since 3C263 and 3C334 are the next two largest objects after these with observable CCs, and we see no counterjets in them here, the absence of counterjets at a level of >~0.1 of the jet brightness in the four largest objects would begin to cast doubt on the hypothesis of intrinsically symmetrical two-sided ejection.

Knowledge of the bulk Lorentz factor will have to come from monitoring suitable objects in this sample for ~parsec-scale motion. The objects which show distinct knots in the presumed VLBI jets and/or show significant flux density variations are the obvious candidates to monitor for component motion. 3C245 and 3C263 are the two best cases, based on the first-epoch maps and, for 3C245, significant variability; see Chapter 3. Prospects are good for 3C207, especially if a second-epoch map were to reveal more clearly a discrete peak in the weaker component which could be tracked. 3C334 is also a possibility, although it will probably require a time base of a few years to detect unambiguously a proper motion because of the limited resolution along the source axis. 3C249.1 needs to be reobserved to determine if it does indeed have a smooth jet, while 3C212 does not look too promising on the basis of all the observations to date. Therefore, it will be difficult and require patience, but it is evident that a large fraction of the central components in the complete sample are, and likely will be found to be, suitable for direct tests of relativistic beaming.

VI. Conclusions

The central components of six double-lobed quasars from the complete sample all show an extended structure on the ~parsec-scale. This structure may be interpreted in terms of the "core-jet" hypothesis for compact, flat-spectrum sources. The VLBI jet components lie on the same side of the compact core as, and are aligned with, one-sided >~kiloparsec-scale jets. We find no two-sided VLBI jets at the present sensitivity limits. A large fraction of the objects has two components with discrete peaks which are highly suitable to monitor for structural variations.

References

Aller, H., and Aller, M. 1985, private communication.

Barthel, P.D. 1984, Ph.D. dissertation, Leiden.

Barthel, P.D. 1986, private communication.

Cohen, M.H., et al. 1975, *Ap.J.*, **201**, 249.

Cornwell, T.J., and Wilkinson, P.N. 1981, *M.N.R.A.S.*, **196**, 1067.

Gull, S.F., and Daniell, G.J. 1978, *Nature*, **272**, 686.

Hine, R.G., and Scheuer, P.A.G. 1980, *M.N.R.A.S.*, **193**, 285.

Hough, D.H., and Readhead, A.C.S. 1984, *Bull.A.A.S.*, Vol.**16**, No.4, p.1010.

Jones, D.L., et al. 1986, *Ap.J.*, **305**, in press..

Kus, A.J., Wilkinson, P.N., and Booth, R.S. 1981, *M.N.R.A.S.*, **194**, 527.

Linfield, R.P. 1981, *Ap.J.*, **244**, 436.

Linfield, R.P. 1982, *Ap.J.*, **254**, 465.

Pearson, T.J., and Readhead, A.C.S. 1984a, in IAU Symposium 110, *VLBI and Compact Radio Sources*, ed. R. Fanti, K. Kellermann, and G. Setti (Dordrecht:Reidel), p.15.

Pearson, T.J., and Readhead, A.C.S. 1984b, *Ann.Rev.Astr.Ap.*, **22**, 97.

Readhead, A.C.S. 1984, in Proceedings of the Workshop on QUASAT, ESA SP-213, *QUASAT-A VLBI Observatory in Space*, ed. W.R. Burke (Noordwijk:European Space Agency), p.139.

Readhead, A.C.S., Cohen, M.H., Pearson, T.J., and Wilkinson, P.N. 1978, *Nature*, **276**, 768.

Readhead, A.C.S., and Wilkinson, P.N. 1978, *Ap.J.*, **223**, 25.

Rogers, A.E.E., et al. 1983, *Science*, **219**, 51.

Scheuer, P.A.G. 1984, in IAU Symposium 110, *VLBI and Compact Radio Sources*, ed. R. Fanti, K. Kellermann, and G. Setti (Dordrecht:Reidel), p.197.

Seielstad, G.A., Readhead, A.C.S., and Pearson, T.J. 1983, *Pub.A.S.P.*, **95**, 842.

Smith, H.E., Spinrad, H., and Smith, E.O. 1976, *Pub.A.S.P.*, **88**, 621.

Smith, M.D., and Norman, C.A. 1981, *M.N.R.A.S.*, **194**, 771.

Swarup, G., Sinha, R.P., and Hilldrup, K. 1984, *M.N.R.A.S.*, **208**, 813.

Wardle, J.F.C. 1984, private communication.

Whitney, A.R. 1982, "The Mark III Correlator: Design, Operation, and Productivity," Northeast Radio Observatory Corporation Haystack Observatory document.

Zensus, J.A. 1984, Ph.D. dissertation, Münster.

Table 1

The Complete Low Redshift VLBI Subsample

Source	IAU Name	z	S_{CC}	R	L(kpc)	C(°)
3C207	0838+133	0.684	588	0.624	69	20
3C212	0855+143	1.049	148	0.111	63	0
3C245	1040+123	1.029	910	1.06	52	5
3C249.1	1100+772	0.311	78	0.087	154	9
3C263	1137+660	0.656	130	0.071	230	1
3C275.1	1241+166	0.557	135	0.122	94	23
3C334	1618+177	0.555	165	0.183	277	4

Table 2

The Telescopes

Station[1]	Diameter(m)	T_{sys}	Peak K/Jy
B	100	110	0.90
K	36	115	0.15
G	43	65	0.21
F	26	170	0.05
O	40	70	0.21

1. B= Max-Planck-Institut für Radioastronomie, Effelsberg, West Germany

   K= Haystack Observatory, Westford, Massachusetts

   G= National Radio Astronomy Observatory, Green Bank, West Virginia

   F= George R. Agassiz Station of Harvard College Observatory, Fort Davis, Texas

   O= Owens Valley Radio Observatory, Big Pine, California

Table 3

Journal of Observations

Date of Observation	Source	Mode	τ(sec)	Stations[1]
4-5 October 1981	All	A	780	BKGFO
1 October 1982	3C263	A	120	BKG(F)O
9 February 1983	3C245	B	120	KGFO
11 February 1983	3C249.1	A	240	BKG(F)O
19 June 1983	3C207	A	120	BKGFO
19 June 1983	3C212	A	120	BKGFO
19-20 June 1983	3C334	A	120	BKGFO
12 February 1984	3C249.1	A	240	BKG(F)O
4 August 1984	3C212	A	16	BKGFO
5 August 1984	3C207	B	60	BKGFO

1. ( ) indicates data not used in analysis.

Table 4

Pilot Survey Results

Source	Scans	Model	S(Jy)	Size[1] (mas)	PA[2]	Date
3C154[3]	3	Point	.10+/-.01	--	--	10/81
3C207	2	Gaussian	.36+/-.09	.3+/-.1	--	10/81
3C207	5	Double	.32+/-.05	--	--	6/83
			.13+/-.06	.4+/-.1	60+50	
					-20	
3C212	3	Gaussian	.15+/-.02	<.3	--	10/81
3C212	5	Gaussian	.17+/-.03	.2+/-.1	--	6/83
3C245	3	Gaussian	.25+/-.04	<.3	--	10/81
3C249.1	5	Double	.03+/-.005	--	--	10/81
			.01+/-.005	.3+/-.1	97+15	
					-15	
3C249.1[4]	25	Double	.04+/-.02	--	--	2/83
			.02+/-.02	.4+/-.2	88+30	
					-30	
3C263	5	Double	.08+/-.02	--	--	10/81
			.03+/-.02	.6+/-.3	117+15	
					-15	
3C275.1	1	Point	.11+/-.01	--	--	10/81
3C334	6	Double	.04+/-.01	--	--	10/81
			.03+/-.01	.6+/-.1	137+15	
					-15	

[1] Size is FWHM for gaussians, separation for doubles.

[2] Position angle, in degrees.

[3] 3C154=0610+261 not in complete sample; optical identification from Smith, Spinrad, and Smith 1976, with $z=0.580$ and $m_V=18.0$.

[4] Double consists of two gaussians with axes <0.35, .6+/-.4 mas, respectively.

Table 5

Flux Densities and Visibilties, Pilot Survey

Source	$S_{10.7}$[1]	S_{corr}[2]	F[3]	V[4]	Date
3C154	0.45	0.15	0.67	0.33	10/81
3C207	0.70var	0.44	0.82	0.63	10/81
3C207	0.70var	0.54	0.84	0.77	6/83
3C212	0.17	0.16	0.94	0.94	10/81
3C212	0.17	0.19	0.88	1.12	6/83
3C245	0.91var	0.36	0.69	0.40	10/81
3C249.1	0.07	0.05	0.78	0.71	10/81
3C249.1	0.07	0.05	1.20	0.71	2/83
3C263	0.17	0.15	0.73	0.88	10/81
3C275.1	0.18	0.14	0.79	0.78	10/81
3C334	0.11	0.08	0.81	0.73	10/81

1. Estimated flux density of CC at 10.7 GHz, Jy.
2. Maximum correlated flux density, Jy.
3. Fraction of S_{corr} in Table 4 model.
4. Visibility = $S_{corr}/S_{10.7}$.

Table 6

Results for 3C207

Model-fitting[1]

Component	S(mJy)	Radius(mas)	PA	Axis(mas)
A	320^{+30}_{-30}	0	0	<~0.3
B	120^{+30}_{-30}	$0.3^{+0.1}_{-0.1}$	95^{+60}_{-60}	<~0.5

Hybrid Mapping

Component	S(mJy)	Radius(mas)	PA
A	330	0	0
B	80	0.34	93

MEM

Component	Peak Flux (mJy/mas^2)	Radius(mas)	PA
A	1150	0	0
B	---	----	--

[1] Errors from ERRFIT (see Appendix A).

Table 7

Results for 3C212

Model-fitting

Component	S(mJy)	Radius(mas)	PA	Axis(mas)
A	~130	0	0	<~0.2
B	~30	~0.4	~-40	----

Hybrid Mapping

Component	S(mJy)	Radius(mas)	PA
A	~135	0	0
B	--	----	--

MEM

Component	Peak Flux (mJy/mas^2)	Radius(mas)	PA
A	597	0	0
B	---	----	--

Table 8

Results for 3C245

Model-fitting

Component	S(mJy)	Radius(mas)	PA	Axis(mas)
A	586^{+30}_{-30}	0	0	<0.3
B	60^{+100}_{-30}	$1.1^{+0.4}_{-0.2}$	-81^{+30}_{-30}	<1.5

Hybrid Mapping

Component	S(mJy)	Radius(mas)	PA
A	581^{+5}_{-5}	0	0
B	44^{+12}_{-12}	$1.18^{+0.06}_{-0.06}$	$-71+5$

MEM

Component	Peak Flux (mJy/mas^2)	Radius(mas)	PA
A	1460^{+340}_{-340}	0	0
B	41^{+33}_{-33}	$1.39^{+.06}_{-.06}$	-77^{+9}_{-9}

Table 9

Results for 3C249.1

Model-fitting

Component	S(mJy)	Radius(mas)	PA	Axis(mas)
A	35^{+3}_{-3}	0	0	<0.15
B	14^{+3}_{-2}	$0.42^{+0.02}_{-0.02}$	91^{+4}_{-4}	<0.3

Hybrid Mapping

Component	S(mJy)	Radius(mas)	PA
A	36^{+2}_{-2}	0	0
B	11+1	$0.40^{+.05}_{-.05}$	90^{+1}_{-1}

MEM

Component	Peak Flux (mJy/mas^2)	Radius(mas)	PA
A	732	0	0
B	--	----	---

Table 10

Results for 3C263

Model-fitting

Component	S(mJy)	Radius(mas)	PA	Axis(mas)
A	95^{+20}_{-10}	0	0	<0.2
B	74^{+20}_{-20}	$0.48^{+0.02}_{-0.02}$	110^{+2}_{-2}	<0.3

Hybrid Mapping

Component	S(mJy)	Radius(mas)	PA
A	95^{+6}_{-6}	0	0
B	58^{+2}_{-2}	$0.48^{+0.01}_{-0.01}$	110^{+1}_{-1}

MEM

Component	Peak Flux (mJy/mas^2)	Radius(mas)	PA
A	2460^{+350}_{-350}	0	0
B	930^{+400}_{-400}	$0.50^{+.02}_{-.02}$	110^{+1}_{-1}

Table 11

Results for 3C334

Model-fitting

Component	S(mJy)	Radius(mas)	PA	Axis(mas)
A	54^{+10}_{-10}	0	0	<0.3
B	36^{+15}_{-15}	$0.9^{+0.3}_{-0.3}$	144^{+5}_{-10}	<0.5

Hybrid Mapping

Component	S(mJy)	Radius(mas)	PA
A	57^{+2}_{-2}	0	0
B	27^{+3}_{-3}	$0.88^{+.07}_{-.07}$	143^{+3}_{-3}

MEM

Component	Peak Flux (mJy/mas^2)	Radius(mas)	PA
A	274	0	0
B	96	0.81	138

Table 12

Position Angle Differences Between Small- and Large-scale Structures

Source	Knot[1]	Radius(″)	PA(°)	ΔPA(°)[2]
3C207	A	1.3	95	0
	B	6.3	91	
3C212	A	0.9	-39	-
	B	5.3	-41	
3C245	A	0.4	-73	2
	B	4.9	-86	
3C249.1	A	1.0	99	9
	B	7.9	92	
3C263	A-B	16.1	112	2
3C334	A	2.7	139	4
	B	17.9	132	

1. A= innermost compact feature in large-scale jet
   B= the more compact outer "hot spot"

2. ΔPA between hybrid map VLBI axis and
   PA of Knot A.

Figure Captions

Fig. 1 - Hybrid maps of central components at conventional resolution; beam FWHM shown cross-hatched.

(a) 3C207: beam is 2.64 x 0.45 mas, PA=168°; scale is 1.0 mas/tick; contours are -0.6,0.6, 2,5,10,20,30,40,50,60,70,80,90 per cent; peak is 324 mJy/beam.

(b) 3C212: beam is 2.64 x 0.45 mas, PA=168°; scale is 1.0 mas/tick; contours are -3,3, 5,10,20,30,40,50,60,70,80,90 per cent; peak is 139 mJy/beam.

(c) 3C245: beam is 2.68 x 0.83 mas, PA=167°; scale is 1.0 mas/tick; contours are -1,1,5, 10,20,30,40,50,60,70,80,90 per cent; peak is 573 mJy/beam.

(d) 3C249.1: beam is 0.52 x 0.48 mas, PA=90°; scale is 0.5 mas/tick; contours are -2.5,2.5, 5,10,20,30,40,50,60,70,80,90 per cent; peak is 35.2 mJy/beam.

(e) 3C263: beam is 0.52 x 0.48 mas, PA=90°; scale is 0.5 mas/tick; contours are -2,2,5, 10,20,30,40,50,60,70,80,90 per cent; peak is 97.0 mJy/beam.

(f) 3C334: beam is 2.21 x 0.46 mas, PA=165°; scale is 1.0 mas/tick; contours are -2,2,5, 10,20,30,40,50,60,70,80,90 per cent; peak is 58.0 mJy/beam.

Fig. 2 - Hybrid maps of central components with "super-resolution; beam FWHM shown cross-hatched.

(a) 3C207: beam is 1.32 x 0.23 mas, PA=168°; scale is 0.5 mas/tick; contours are 5,10, 20,30,40,50,60,70,80,90 per cent; peak is 258 mJy/beam.

(b) 3C212: beam is 1.32 x 0.23 mas, PA=168°; scale is 0.5 mas/tick; contours are -3,3,5 10,20,30,40,50,60,70,80,90 per cent; peak is 133 mJy/beam.

(c) 3C245: beam is 1.79 x 0.55 mas, PA=167°; scale is 1.0 mas/tick; contours are -1,1,5, 10,20,30,40,50,60,70,80,90 per cent; peak is 570 mJy/beam.

(d) 3C249.1: beam is 0.26 x 0.24 mas, PA=90°; scale is 0.5 mas/tick; contours are -3,3,5, 10,20,30,40,50,60,70,80,90 per cent; peak is 28.7 mJy/beam.

(e) 3C263: beam is 0.35 x 0.32 mas, PA=90°; scale is 0.5 mas/tick; contours are -2,2,5, 10,20,30,40,50,60,70,80,90 per cent; peak is 81.4 mJy/beam.

(f) 3C334: beam is 1.11 x 0.23 mas, PA=165°; scale is 0.5 mas/tick; contours are -2,2,5, 10,20,30,40,50,60,70,80,90 per cent; peak is 45.1 mJy/beam.

Fig. 3 - Maximum entropy maps of central components.

(a) 3C207: scale is 0.2 mas/vertical tick; contours are 2,5,10,20,40,60,80,100 per cent; peak is 1152 mJy/mas^2.

(b) 3C212: scale is 0.2 mas/vertical tick; contours are 1,2,5,10,20,40,60,80,100 per cent; peak is 597 mJy/mas^2.

(c) 3C245: scale is 1.0 mas/tick; contours are 2,3,4,10,20,40,60,80,100 per cent; peak is 1699 mJy/mas^2.

(d) 3C249.1: scale is 0.2 mas/vertical tick; contours are 1,2,5,10,20,40,60,80,100 per cent; peak is 732 mJy/mas^2.

(e) 3C263: scale is 0.2 mas/vertical tick; contours are 1,5,15,25,40,60,80,100 per cent; peak is 2710 mJy/mas^2.

(f) 3C334: scale is 0.2 mas/vertical tick; contours are 2,5,15,30,40,60,80,100 per cent; peak is 274 mJy/mas^2.

Fig. 4 - Maps of large-scale structure

(a) 3C207: 5 GHz VLA, courtesy of J.F.C. Wardle, unpublished.

(b) 3C212: 5 GHz VLA, courtesy of R.A. Laing, unpublished.

(c) 3C245: 1.6 GHz MERLIN, courtesy of A.R. Foley and R. Davis (in Foley's Ph.D. thesis, Manchester).

(d) 3C249.1: 408 MHz MERLIN, reprinted from M.N.R.A.S. 203, 833, with the permission of C.J. Lonsdale.

(e) 3C263: 1.5 GHz VLA, courtesy of D.L. Shone, unpublished.

(f) 3C334: 5 GHz VLA, courtesy of J.F.C. Wardle (published in IAU Symposium 97, p.129.)

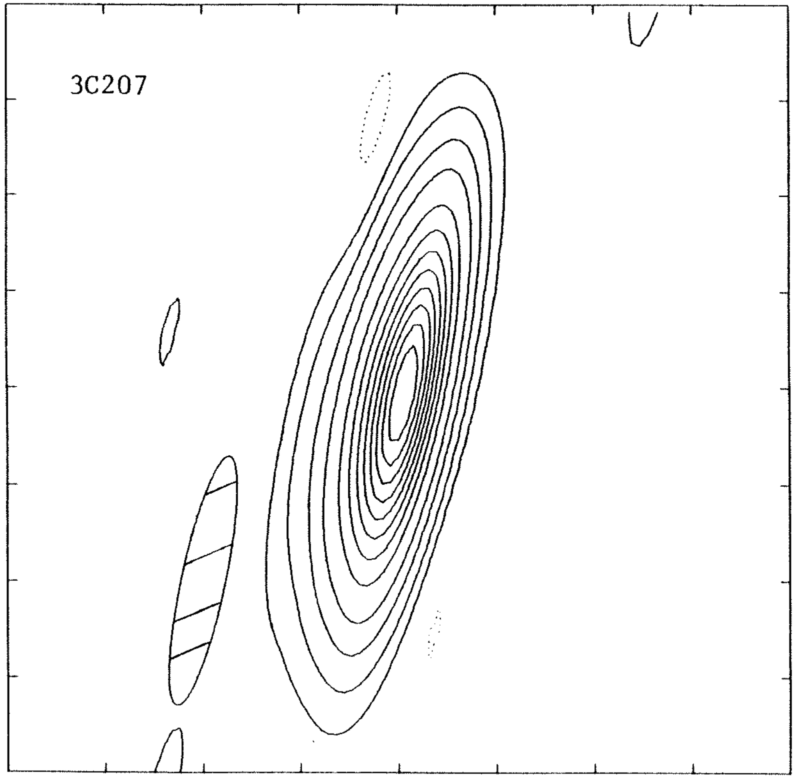

Figure 1a

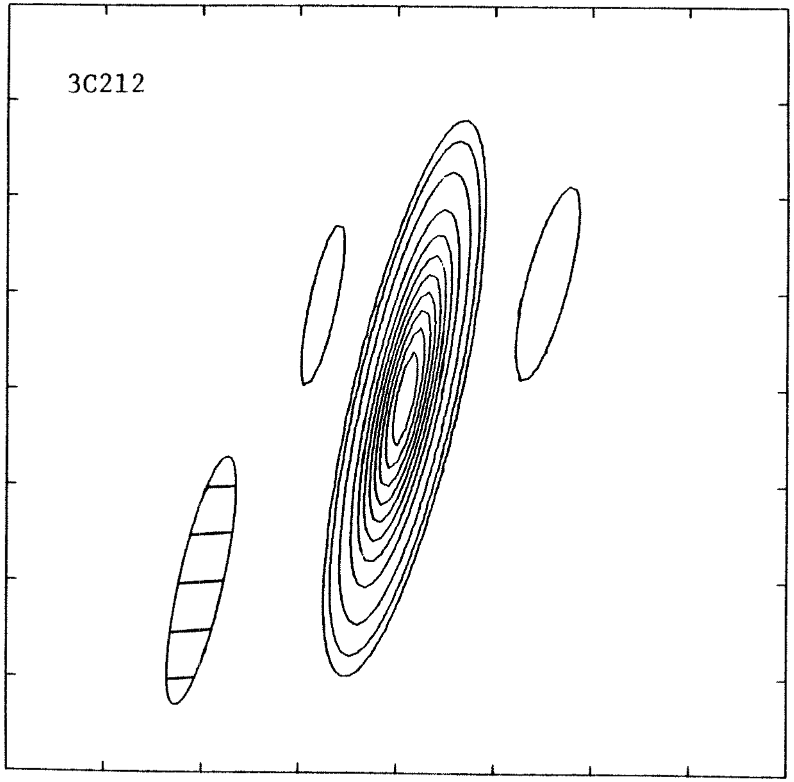

Figure 1b

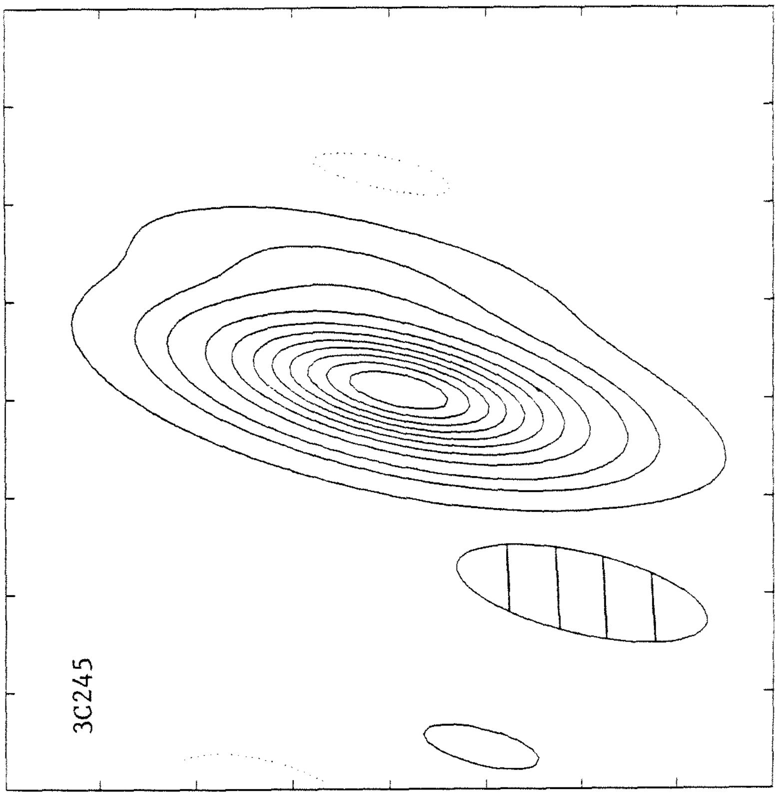

Figure 1c

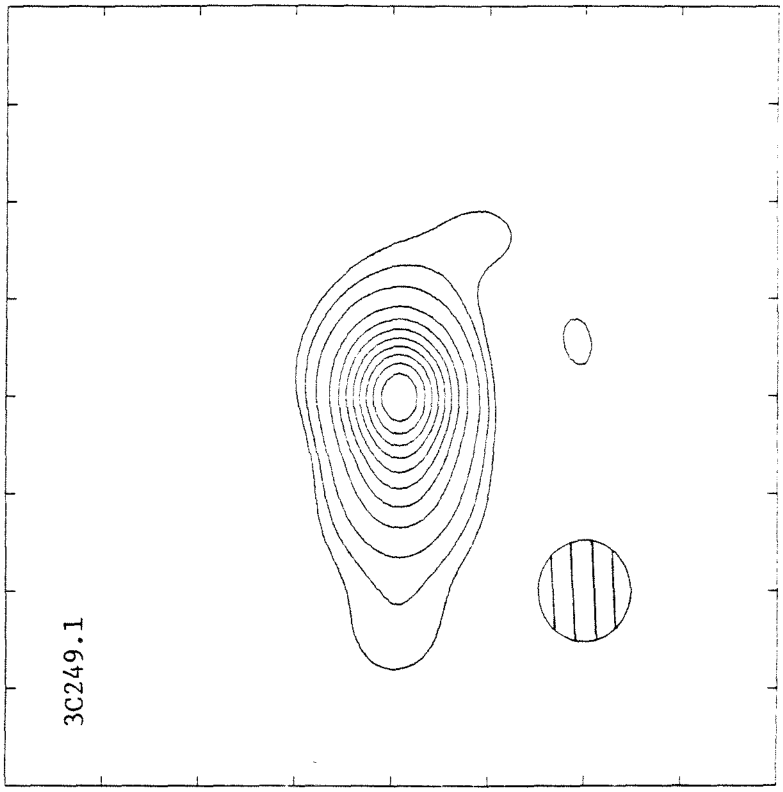

Figure 1d

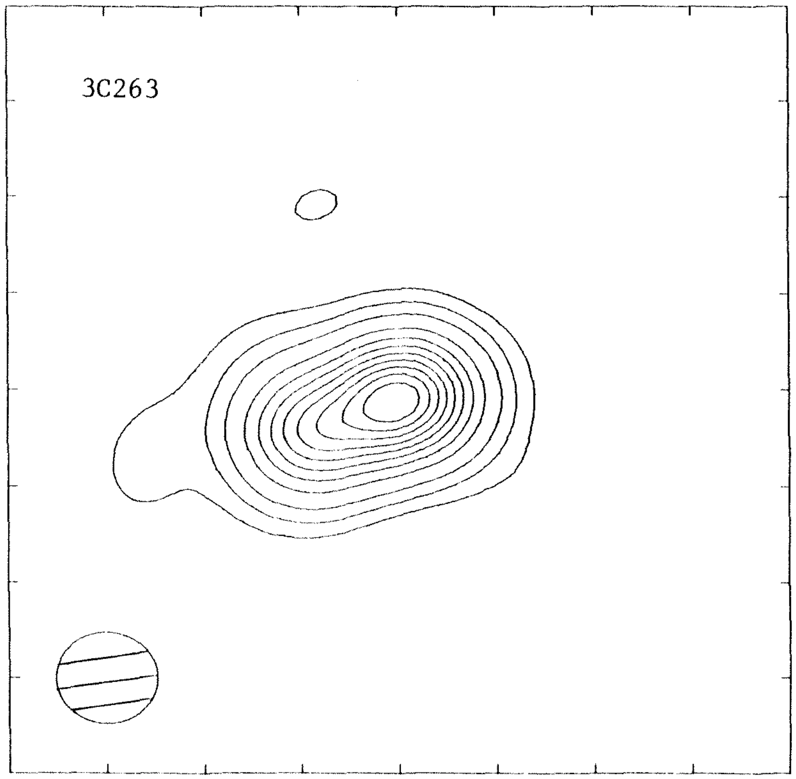

Figure 1e

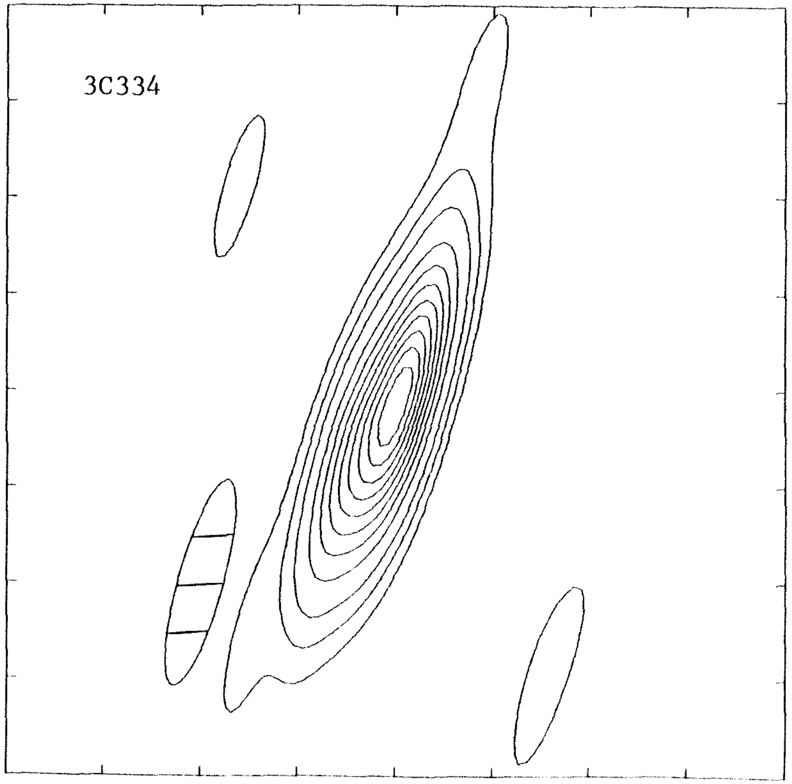

Figure 1f

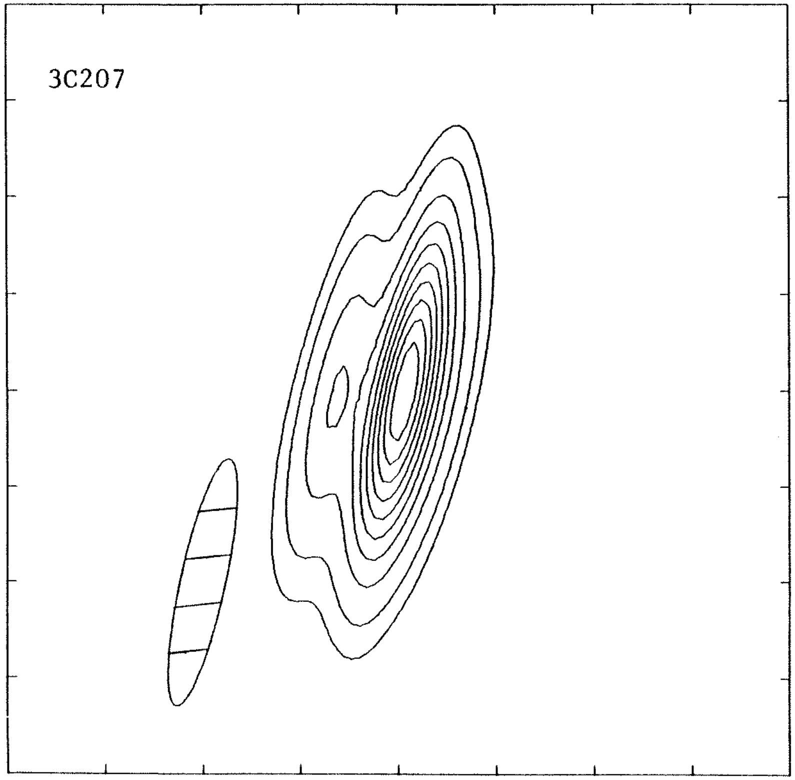

Figure 2a

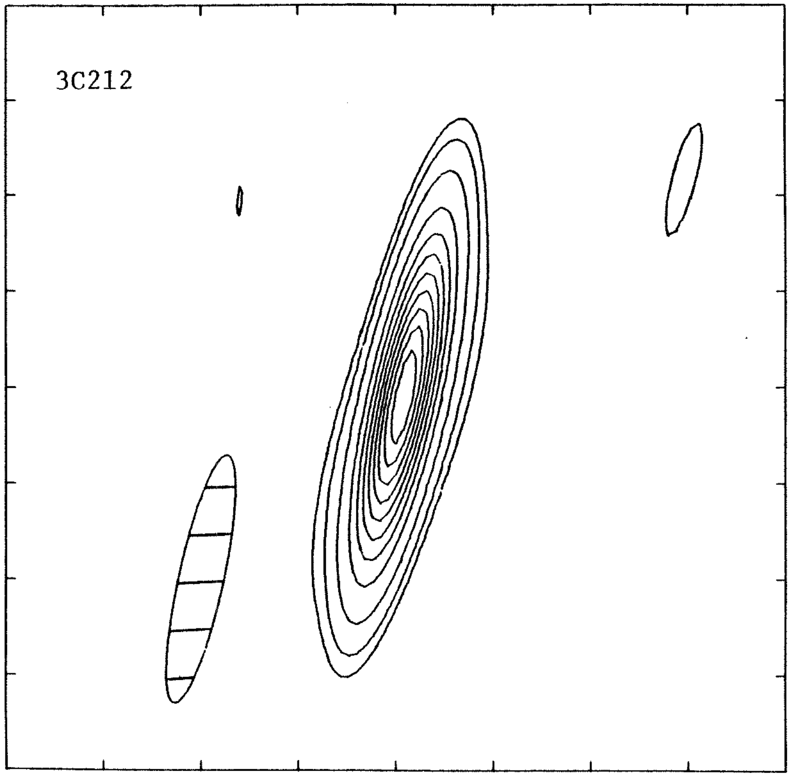

Figure 2b

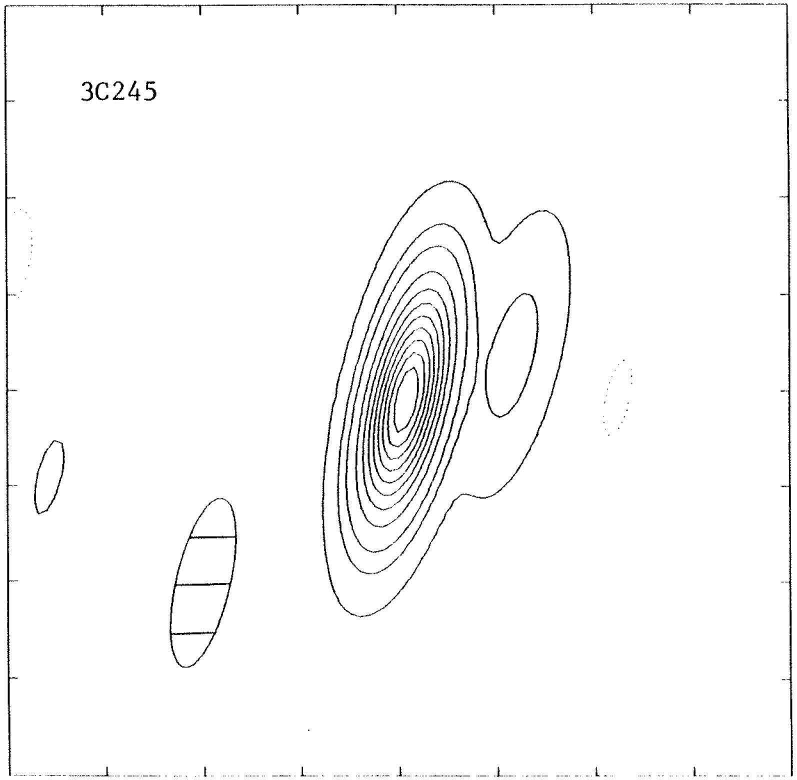

Figure 2c

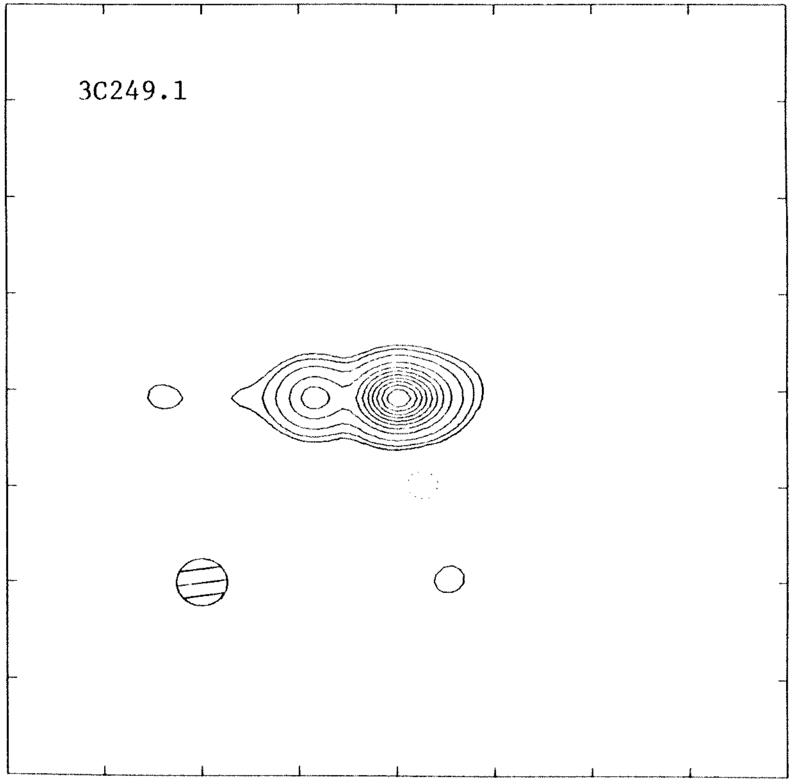

Figure 2d

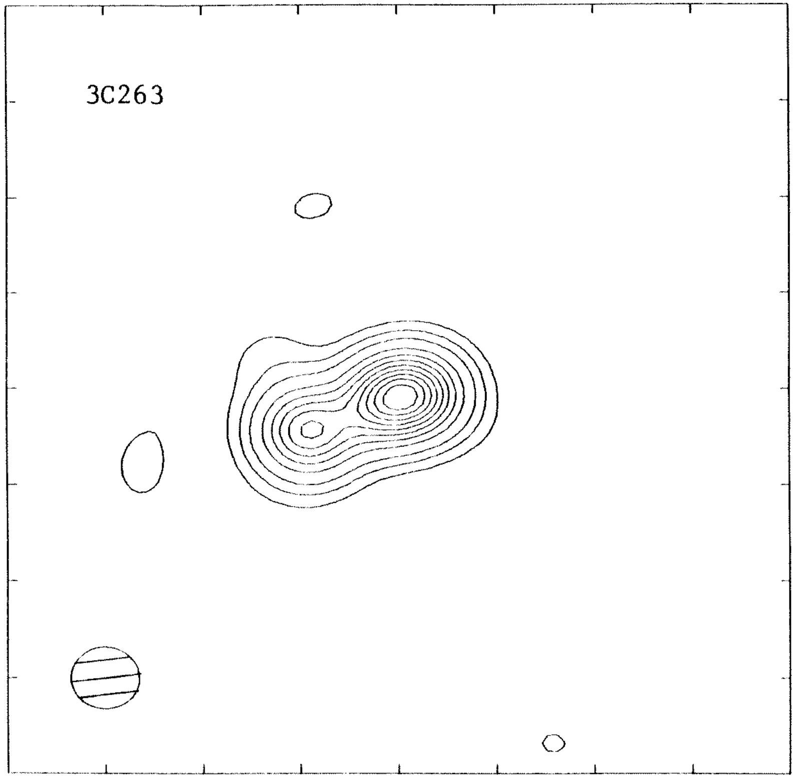

Figure 2e

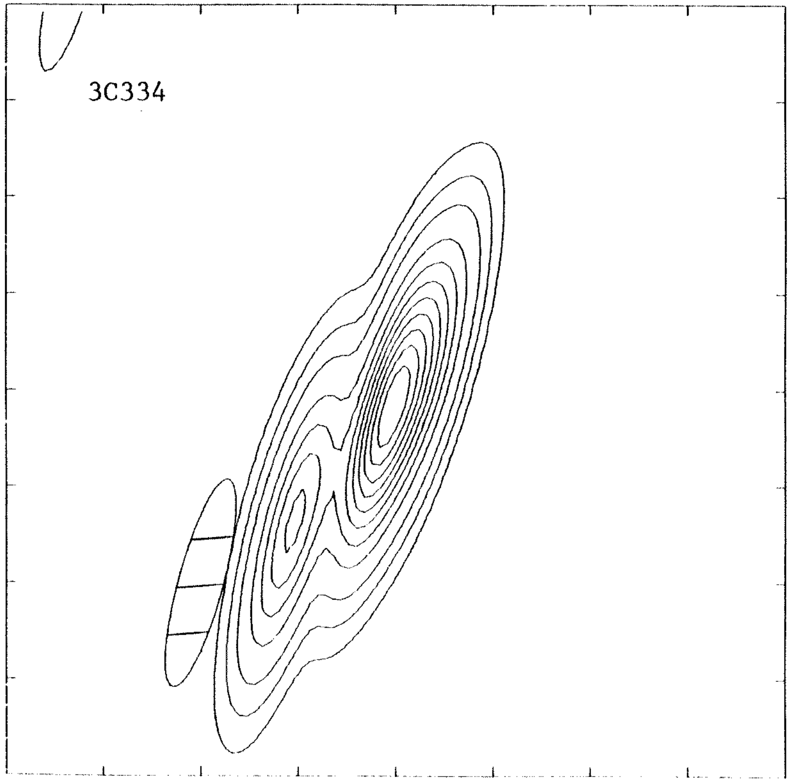

Figure 2f

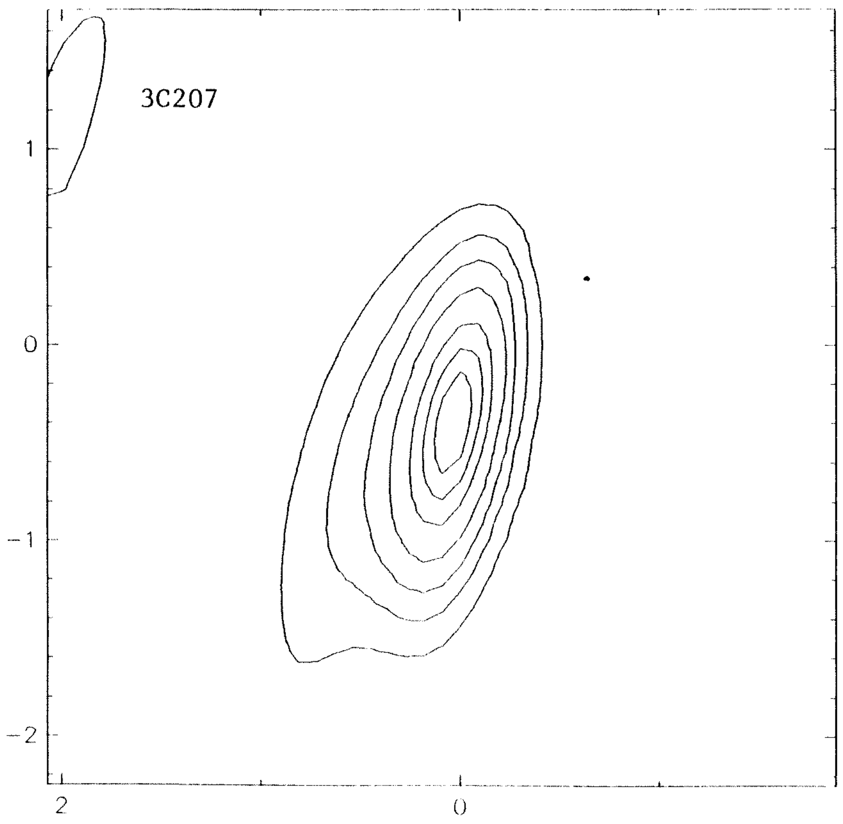

Figure 3a

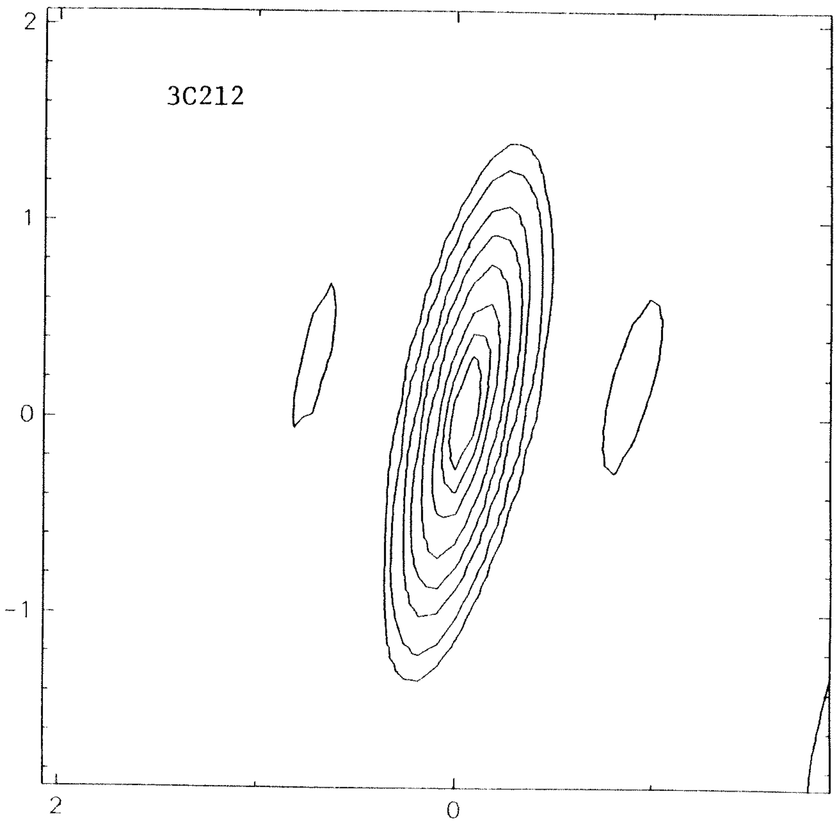

Figure 3b

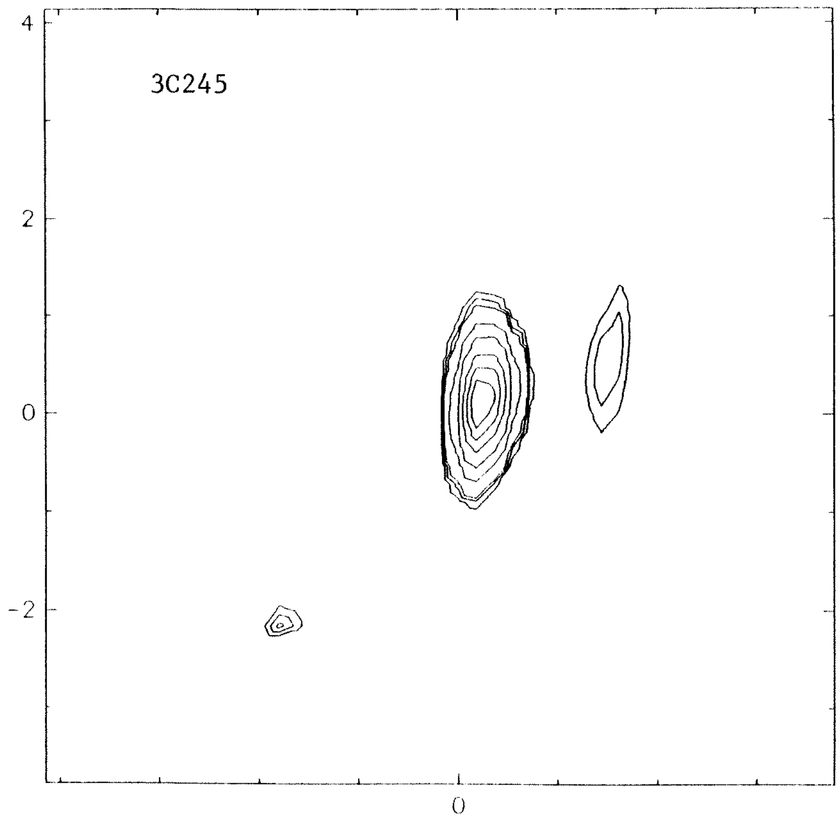

Figure 3c

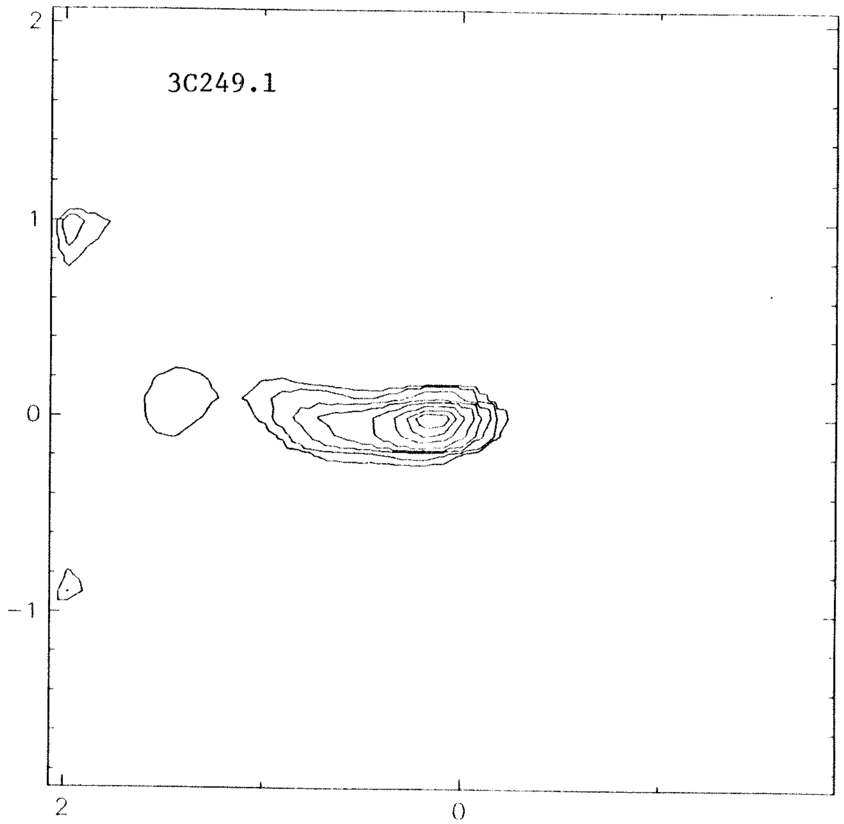

Figure 3d

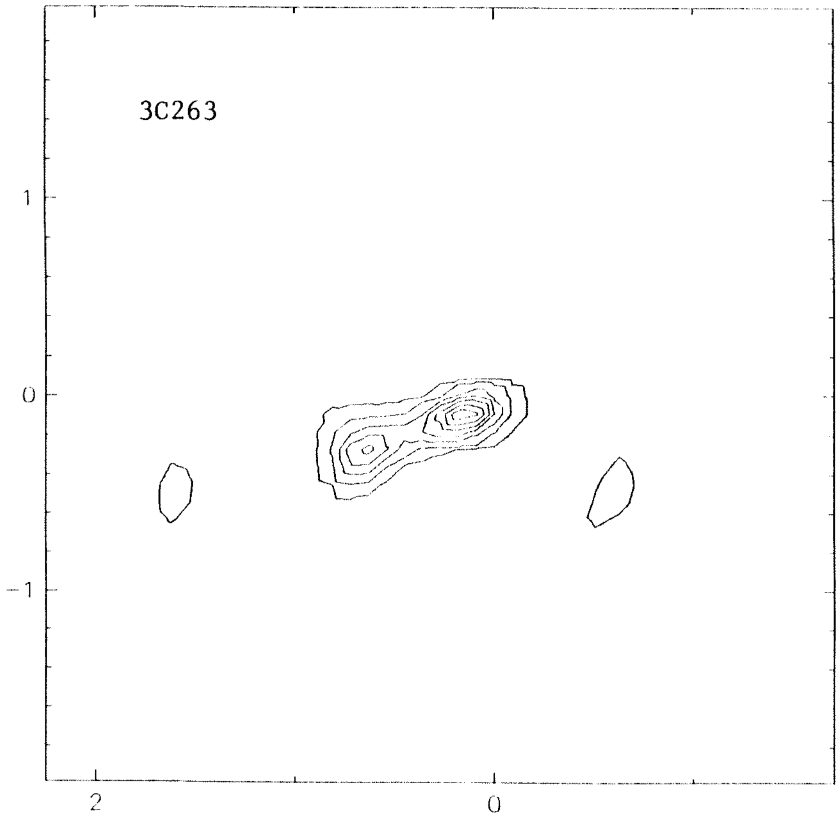

Figure 3e

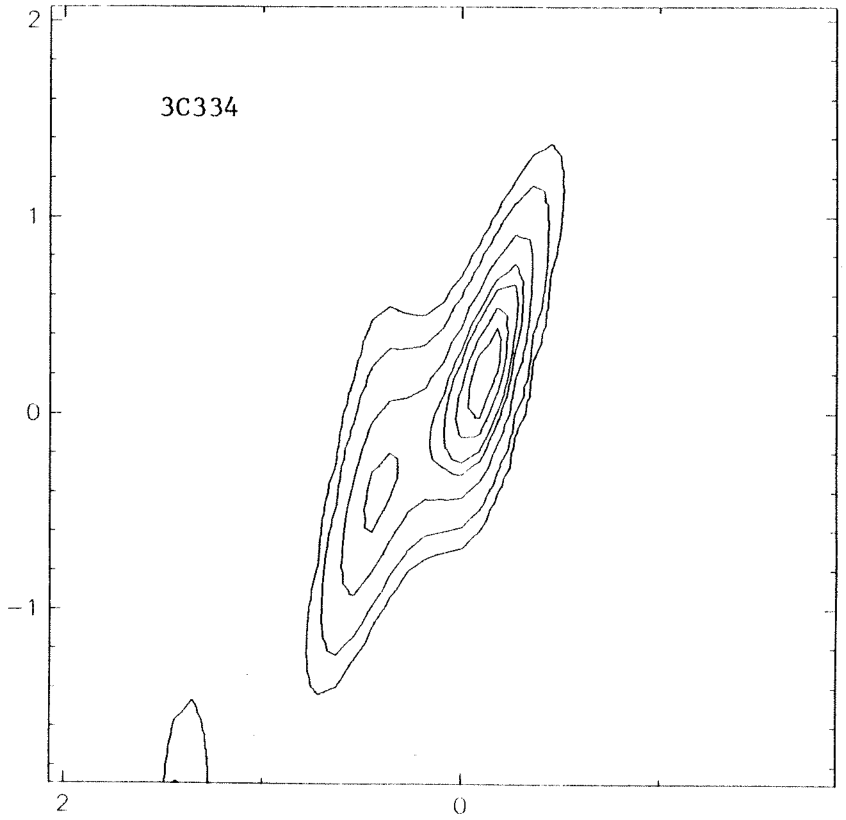

Figure 3f

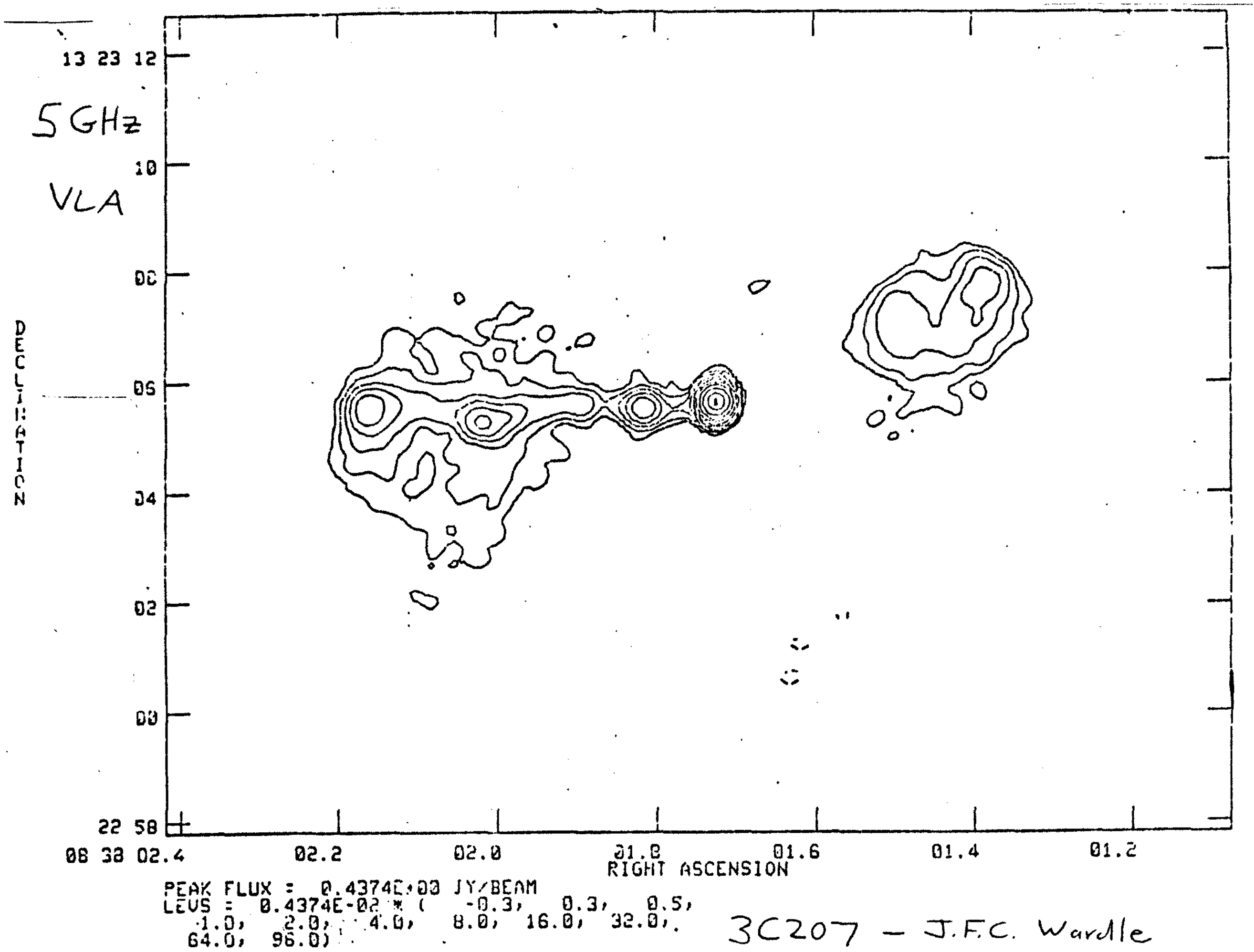

5 GHz

VLA

3C207 - J.F.C. Wardle

Figure 4a

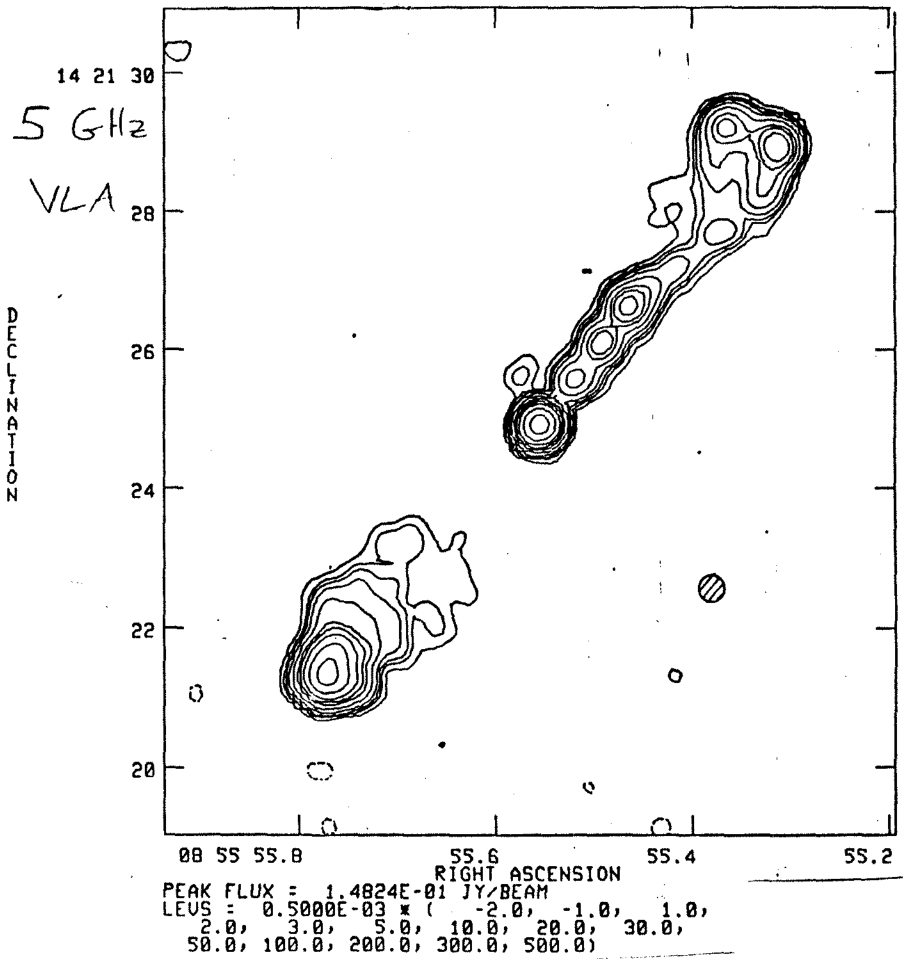

3C212 - R.A. Laing

Figure 4b

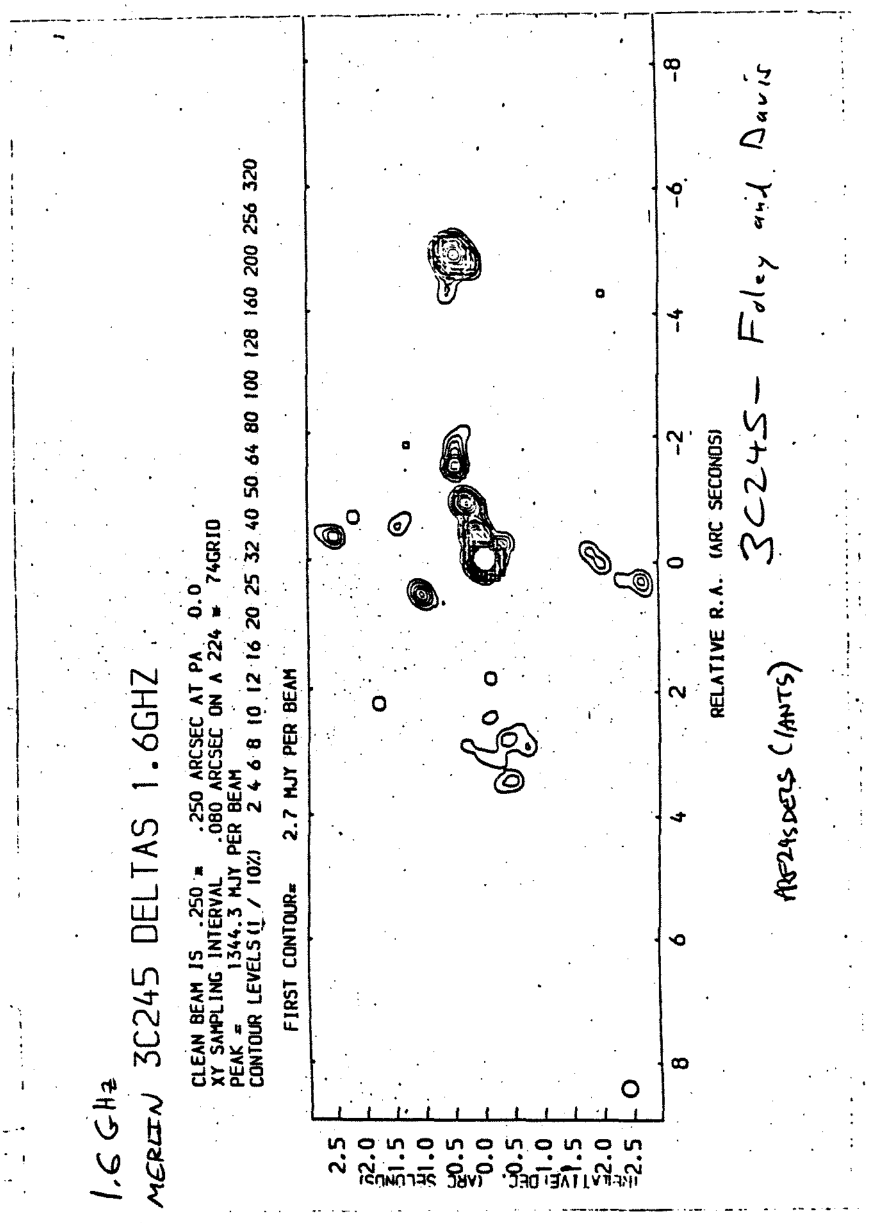
1.6 GHz
MERLIN 3C245 DELTAS 1.6GHZ
CLEAN BEAM IS .250 * .250 ARCSEC AT PA 0.0
XY SAMPLING INTERVAL .080 ARCSEC ON A 224 * 74GRID
PEAK = 1344.3 MJY PER BEAM
CONTOUR LEVELS (1 / 10%) 2 4 6 8 10 12 16 20 25 32 40 50 64 80 100 128 160 200 256 320
FIRST CONTOUR= 2.7 MJY PER BEAM
RELATIVE DEC. (ARC SECONDS)
2.5
2.0
1.5
1.0
0.5
0.0
-0.5
-1.0
-1.5
-2.0
-2.5
RELATIVE R.A. (ARC SECONDS)
8
6
4
2
0
-2
-4
-6
-8
3C245 - Foley and Davis
AB245DELS (IANTS)

Figure 4c

0.4 GHz

MERLIN

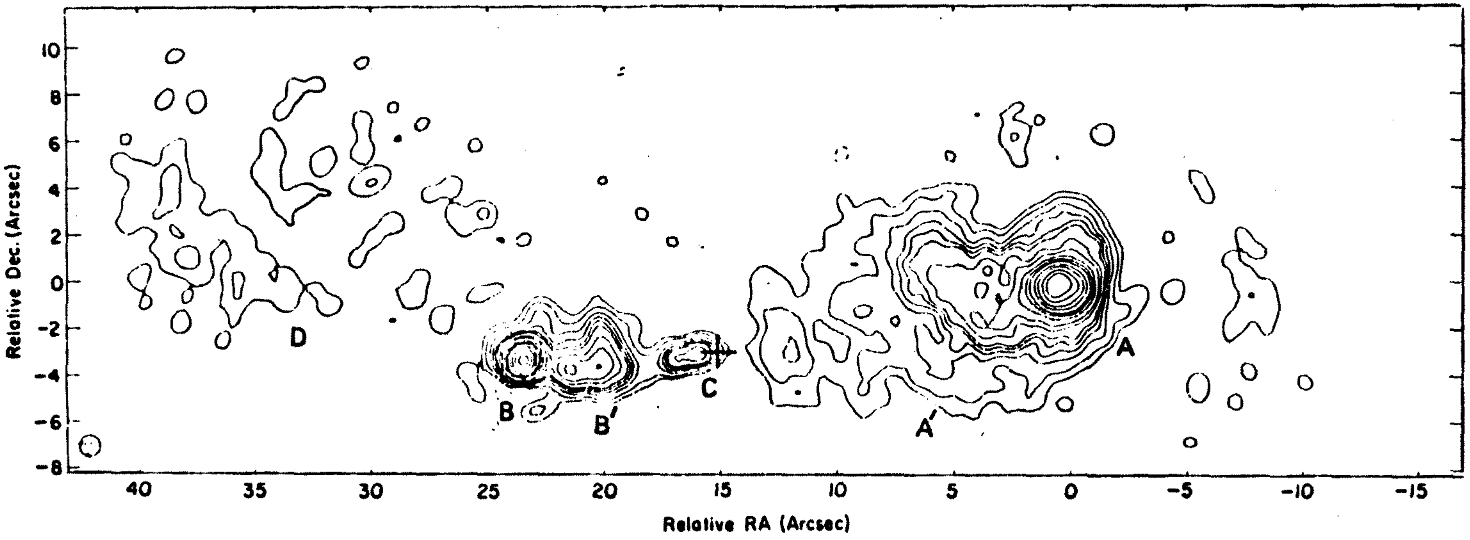

Figure 5. 3C 249.1 at 408 MHz with 0.9-arcsec beam. Contours are 0.5, 1, 2, 3, 4, 5, 7.5, 10, 15, 20, 25, 35, 45, 60, 75 per cent of the peak brightness, which is 640 mJy beam^{-1}.

3C249.1 — Lonsdale and Morison

Figure 4d

1.5 GHz
VLA

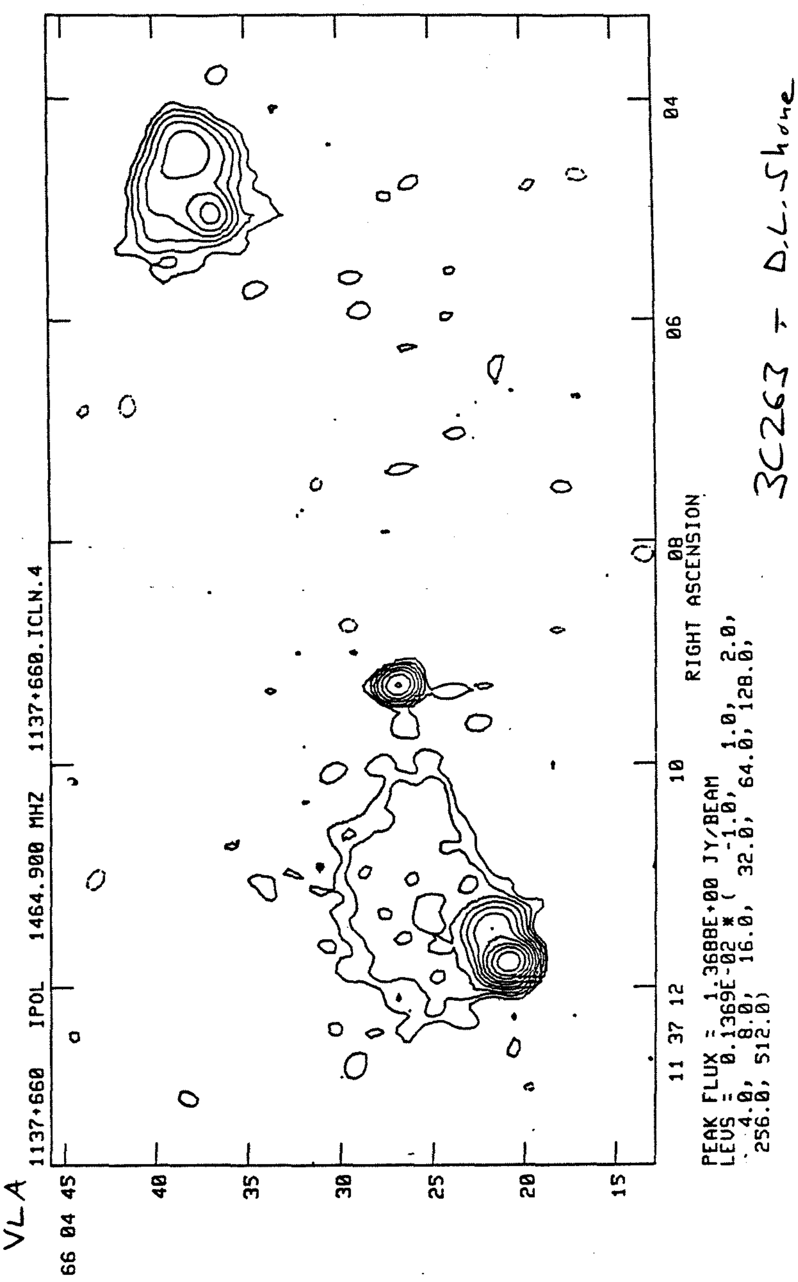

3C263 - D.L. Shone

Figure 4e

5GHz
VLA

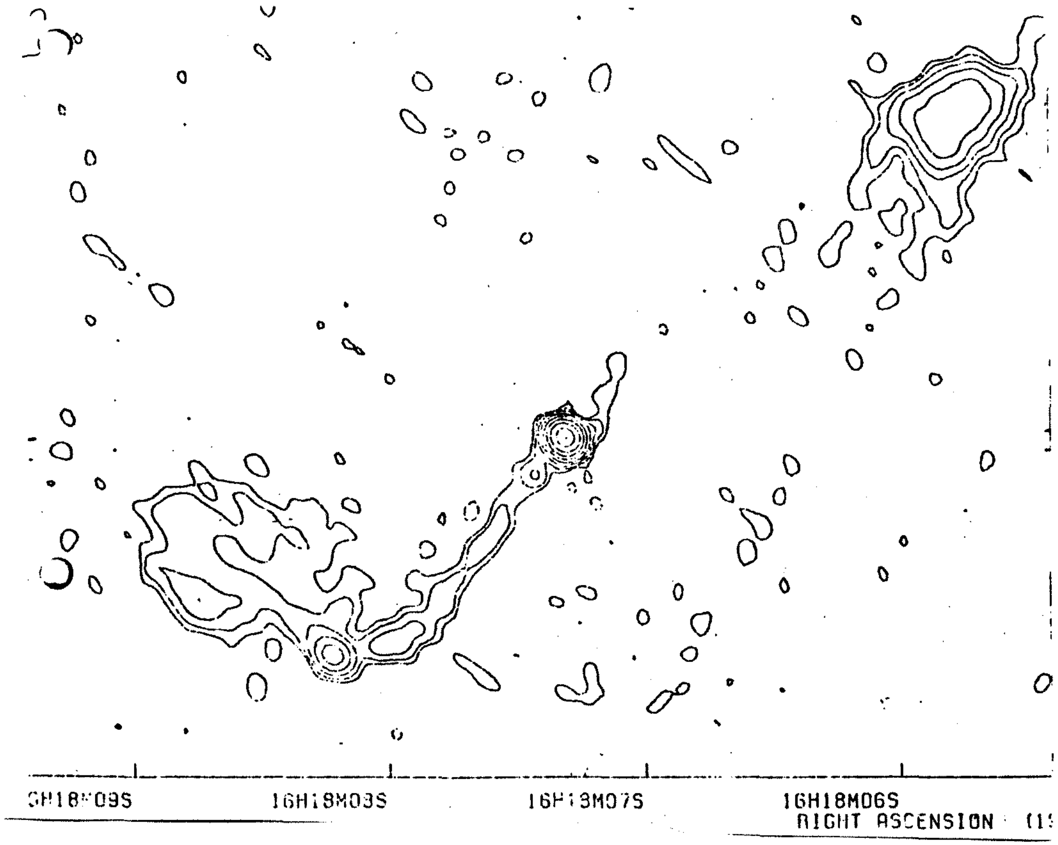

3C334 - J.F.C. Wardle

Figure 4f

CHAPTER 3

THREE-EPOCH VLBI OBSERVATIONS OF THE CENTRAL COMPONENTS OF 3C245 AND 3C263

Summary

We present VLBI observations of the central components of 3C245 and 3C263 at three epochs. Superluminal expansion with an apparent velocity of ~1.5c is found in 3C263, while the evidence suggests an apparent velocity of ~4c in 3C245. This demonstrates that it will likely be possible to monitor component motion in the nuclei of many double-lobed quasars. The results for these first two objects in the complete sample are consistent with the simple relativistic beaming model and a bulk Lorentz factor ~4 in both objects.

I. Introduction

The main result of Chapter 2 was the discovery that the central components (CCs) of double-lobed quasars often exhibit a distinct double structure on the ~parsec scale. A prime objective of our survey is to test the relativistic beaming hypothesis in these objects. This test requires the presence of discrete features in the VLBI jets which can be monitored for proper motion. We are fortunate that several objects possess such a structure and are therefore excellent candidates for multiple-epoch observations.

On the basis of VLBI structure, overall morphology, and strength of the CC emission, we have selected 3C245 and 3C263 as the two best objects for repeated VLBI observations. 3C245 has a CC which contains a strong core with a weak, yet distinct, secondary component; the overall projected linear size is small, and the CC is the most dominant in the complete sample defined in Chapter 1. 3C263 has a CC which reveals the clearest double structure, with two components of comparable strength; the overall size is large, and the CC is of moderate strength.

In Chapter 1 great care was taken to select a complete sample free of orientation bias. Thus, unlike other VLBI studies, we will be able to test the simple beaming theory, which depends strongly upon the angle of the source axis to the line-of-sight, θ, over a very large range of θ. In particular, if the bulk flow velocity is relativistic and is similar in all these objects, then only a small fraction of sources favorably oriented at small Θ should display large superluminal motions.

A comprehensive test naturally requires observations of many objects in the sample over a long period. However, it is interesting to examine the results on 3C245 and 3C263 in the context of the beaming theory. Since 3C245 is of small apparent size and has a dominant CC (which is also variable in flux density), it may well be a source which is oriented at relatively small Θ. 3C263, however, is of large apparent size and has a CC of intermediate strength, which suggest that it may be an object oriented at a relatively large Θ. We must be extremely cautious in drawing any conclusions based on a comparison of only two objects. But the detection of markedly different apparent velocities in these two objects would either be consistent with the simple beaming model, or lead us to consider a more sophisticated model which produces relativistic outflow over a broad range of angles. The choice of model, of course, would depend upon which object displayed the larger superluminal motion.

In this chapter, we present the results of three-epoch Mark III VLBI observations of the CCs of 3C245 and 3C263. Brightness distributions are determined, using the same techniques used in Chapter 2. Component motion and evolution are described, and implications for the beaming model are discussed.

II. Observations and Processing

The observations were made under the auspices of the U.S. VLBI Network and in conjunction with the Max-Planck-Institut für Radioastronomie. The 32- meter telescope of Medicina was available for the third experiment on 3C263, thanks to the efforts of F. Mantovani. The telescope locations and properties are given in Table 1, and the journal of observations is provided in Table 2. All observations were made at a frequency of 10.7 GHz, and data were recorded with the Mark III system (Rogers, et al. 1983) at either full or half bandwidth (56 or 28 MHz) as indicated in Table 3. 3C263 has been observed in collaboration with J.A. Zensus and R.W. Porcas.

All the data for 3C245 and some of the data for 3C263 were correlated on the Mark III processor at Haystack Observatory (Whitney 1982). Most of the 3C263 data were correlated on an identical processor at the Max Planck Institut für Radioastronomie. Fringe-fitting and coherent averaging were performed at the processors, and export tapes containing the correlation coefficients and phases were prepared to transfer these data to the California Institute of Technology for further reduction.

III. Data Reduction

Data editing and calibration were done in the same manner described in Chapter 2, Section III, where the treatment of the first-epoch data is also given. The October 1983 amplitudes for 3C245 showed a significant scatter, and a 5 percent absolute calibration error was applied to smooth these data. The Green Bank gain curve was again not well determined in all cases. Gain adjustments for this station are discussed for the individual experiments in Section IV.

We have used the three methods of determining the source brightness distributions here described in Chapter 2 -- model fitting, hybrid mapping, and maximum entropy mapping. Similar error analysis and "super-resolution" mapping were done (see also Appendices A and B). The maps all have rms noise levels ~1-<~2 times the noise expected from the input data errors.

For these objects, we not only find that most of the structure is within a conventional beam width, but we are also interested in measuring small changes in this structure as a function of time. Therefore the results using all three methods are compared in detail at each epoch and across all epochs in Section IV.

IV. Results

A. 3C263

1. First Epoch

Four telescopes were used successfully in October 1982. The calibration of the Green Bank telescope was difficult since no gain curve was measured. We proceeded by assuming a gain curve from February 1983 and adjusting the gains for Green Bank alone, using a model of two Gaussian components which already fitted the data for the other stations very well. Thus, the Green Bank calibration is not fully independent, but this procedure allows us to use four stations with an internally consistent calibration instead of only three.

The results for the first epoch are given in Table 3. A good fit to the data is obtained with a model consisting of two circular Gaussian components of separation D = 0.48 milliarcseconds (mas). The weaker of the two components lies at a position angle (PA) of 110° relative to the stronger component.

A hybrid map is shown in Figure 1a at the conventional resolution (clean beam full width at half maximum = 0.5 mas). In Figure 2a, the CLEAN delta-functions have been convolved with a clean beam with FWHM = 0.35 mas. The peaks of the two components are separated by 0.48 mas, in excellent agreement with the model fitting result. The flux density ratio is 1.6:1. The total flux density of 153 mJy in the two components is close to an extrapolation to 10.7 GHz of the spectrum of the CC (~170 mJy), indicating that essentially all the CC flux density is accounted for on the ~< 1 mas scale.

We also made an MEM map (Figure 3a), and obtained a good fit using a window equal in size to the hybrid map CLEAN window. The separation of the two components is confirmed by measuring the distance between the two centroids, which yields D=0.50 mas. The ratio of peak flux densities is 2.6:1.

2. Second Epoch

Three telescopes were used to observe full (u,v) tracks in October 1983. Maps were made including very short tracks for Green Bank and Fort Davis, but the three-station results are presented here. No special calibration difficulties were encountered.

The results for the second epoch are given in Table 4. The source is again represented well by two circular Gaussian components. The separation is D = 0.53 mas along PA = 108°.

The hybrid map at standard resolution (Figure 1b) again shows an extension from the core. The "super-resolved" hybrid map is shown in Figure 2b. The component peaks are separated by 0.54 mas, close to the value obtained from model fitting. The total flux density in the two components is ~127 mJy, with a flux density ratio of ~2.0:1.

The MEM map (Figure 3b) confirms the component separation, with the distance between centroids D = 0.57 mas. The ratio of peak flux densities is ~4.2:1.

3. Third Epoch

We used five telescopes in December 1984. Two of the baselines including Medicina, those to Haystack and Owens Valley, had to be discarded during the course of the analysis because of poor quality, low signal-to-noise ratio data.

A two-component model again provides a reasonable fit to the data. The components stand at a separation of 0.61

mas. This time, however, a superior fit is obtained if the weaker component is taken to be an elliptical Gaussian, with its major axis along the separation axis of the double (see Table 5). The core component is still very compact.

The conventional and "super-resolved" hybrid maps are displayed in Figures 1c and 2c, respectively. Significant corrections were made to the Green Bank gains in the later iterations of mapping, and the maps shown here were made using these corrected data. The weaker component is more clearly separated from the core on the conventional map than at the earlier epochs. The component separation on the "super-resolved" map is 0.63 mas along PA = 108°. The total flux density is ~142 mJy, with a flux density ratio of ~3.2:1.

A MEM map made with the gain-corrected data from hybrid mapping, less Medicina (Figure 3c), yields R=0.71 mas and a ratio of peak flux densities ~6.0:1.

4. Comparison of the Three Epochs

It is of primary interest to measure any change in angular separation of the double with time. Using each of the three methods described above, we find that the double has expanded by a small, yet discernible, amount. This is true whether we compare D for each method independently at all three epochs, or we use a straight average value of D for the three methods at each epoch and then calculate the change in D, ΔD.

The change in separation for the model fitting between the first and second epochs is ΔD=0.05+/-0.04 mas, which is only significant at the 1σ level. Between the second and third epochs, ΔD=0.08+/-0.05 mas, again a marginal result. If we use the total time base, however, from the first to the third epoch, ΔD=0.13+/-0.05 mas, which is clearly a significant detection of motion. The time interval is 2.2 years, which leads to a proper motion of 0.06 +/- 0.02 mas/year. The hybrid and MEM maps yield proper motions of 0.07 and 0.10 mas/year, respectively.

The position angle of the moving component has remained constant, within the errors. It is clear, however, that this component has diminished in flux density by ~35 per cent between the first and later epochs, based on the models and hybrid maps. The core component seems to show small brightness fluctuations at the ~10 per cent level.

To confirm these structural changes, we also repeated all of the model fitting and mapping using the subset of stations Effelsberg, Haystack, and Owens Valley which were common to all experiments. This provided similar (u,v) coverage at all three epochs. The results agree very well with those using the full complement of stations.

B. 3C245

1. First Epoch

Four U.S. stations were used in February 1983; Effelsberg was lost due to severe weather conditions. The calibrations of Haystack and Green Bank were poorly determined. Therefore, gains were scaled for these two stations prior to mapping.

A two-component model fits the data fairly well, and the hybrid and MEM (with gain-corrected data) mapping results agree with this model, given the large uncertainties. See Table 6 and Figures 4a, 5a and 6a. There is obviously structure on the >~ 10 mas scale, to which the Haystack-Green Bank baseline is sensitive. Because we could not determine this structure with so little short-baseline information, the Haystack-Green Bank baseline was omitted in the hybrid mapping. The flux density ratio is ~10:1. The position of the weaker component is poorly determined, but it lies roughly 1 mas from the core in PA~ -75°.

As noted in Chapter 2, the CC has undergone a flux density outburst since the initial pilot survey of October 1981. It is difficult to determine the precise time of the outburst. The best estimate comes from the 10.8 GHz total flux density monitoring of Seielstad, Readhead, and Pearson (1983), who measured a jump of ~0.4 Jy between August 1982 and November 1982. Therefore, the outburst probably occurred sometime in the last quarter of 1982.

2. Second Epoch

Five telescopes were used in October 1983, with no particular calibration problems. The results are given in Table 7.

A two-component model again serves to fit the data, with similar results for the hybrid and MEM mapping (see

Figures 4b, 5b, and 6b). However, now a broad Gaussian of FWHM=0.33 mas is required for the core component. (If a model of two point sources is fitted to the core, the two point components are of about equal flux density and are aligned roughly in the east-west direction at a separation of 0.26 +/- 0.03 mas). The flux density ratio is ~10:1. The position of the outer component is still poorly determined, with D ~ 1 mas and PA ~ -70°.

The total source flux density measured at Effelsberg was 1.27 +/- 0.03 Jy.

3. Third Epoch

Five telescopes were used in the December 1984 observations. The Green Bank gain curve required adjustments during the late stages of the mapping process to obtain acceptable fits. See Table 8.

At this epoch, a new component has clearly emerged from the core (Figures 4c, 5c, and 6c). Both the "super-resolved" hybrid and MEM maps show a distinct peak in the new component. The weak outer component is still detected, but it appears even weaker than at the earlier epochs, and its position is even more poorly constrained. The new component close to the core, A2, is about 80 percent as strong as the core as measured by all three methods. It is emerging along PA=~-70°, and is thus well aligned with the innermost knots in the large-scale jet (see Chapter 2). Model fitting gives the separation as 0.40 mas, whereas the hybrid and MEM (without Green Bank) maps yield 0.34 and 0.33

mas, respectively.

The total source flux density measured at Effelsberg was 1.12 +/- 0.02 Jy, which gives a drop of 0.15 +/- 0.05 Jy between the second and third epoch. This agrees with the decrease of 0.19 Jy measured off the hybrid maps.

4. Comparison of All Three Epochs

It is evident that the first-epoch map was made not long after a dramatic flux density increase in the core. At the second epoch, we are sensitive to a broadening of the core but cannot detect individual components that might be in the core and be associated with the outburst. By the third epoch, a new component has clearly emerged from the core, and the total flux density of A1 plus A2 (see Table 8) has dropped by ~30 percent from the first two epochs. Thus, as in 3C263, a component appears to be moving outward and decaying in flux density along the way, although we cannot determine flux densities of the individual components prior to the third epoch. If we assume that the appearance of the new component coincided with the flux density increase in ~September 1982, and that this component has expanded outward at constant velocity since then, then it has traveled ~0.35 mas in 2.3 years. This yields a proper motion of 0.15 mas/year. If we adopt the double model of the core at the second epoch, a similar value of 0.12 +/- 0.06 mas/year is obtained. We must stress, however, that no motion has been directly measured, and that the assumption of constant velocity could well be a poor one (e.g., 3C345 in Biretta 1985).

We have determined the position of the centroid of component B relative to the half-power contour on the eastern edge of the core at each epoch. This side of the core is opposite the presumed motion, and provides the best reference point for measuring the position of B. Unfortunately, B is so weak that a measurement of ΔD between the first and third epochs results in ~0.14 +/- 0.25 mas, and thus we cannot make any deductions about its motion.

V. Discussion

We have demonstrated definite expansion of the VLBI double structure in the CC of 3C263 and probable expansion of the double structure in the CC of 3C245. Considering these objects together with 3C179 (Porcas 1981) and others in the sample of Zensus and Porcas (1984) which show structural variations, it is now clear that component motion in the CCs of double-lobed quasars is a frequent phenomenon. Thus, the properties of these CCs, in terms of not only morphology but also motion, are very similar to the cores in the core-dominated, flat-spectrum sources. At the third epoch for 3C263, the weaker component of the VLBI double is definitely elongated along the main axis of the source. Thus this component clearly resembles the characteristic jet components seen in other compact radio sources. In addition, the moving components in the CCs evolve in flux density, decaying as they move outward, as has been seen, for instance, in the flat-spectrum object 3C345 (Unwin 1982).

We can translate the observed or deduced proper motions into apparent transverse velocities following Cohen and Unwin (1982):

$$\beta_{app} = \mu s (1+z) \quad , \qquad (1)$$

where β_{app} is the apparent transverse velocity in units of the speed of light, μ is the proper motion in mas per year, s gives the scale of light-years per mas, and z is the redshift. For 3C263 at $z=0.656$, assuming $H_o=100$ km/s/Mpc and $q_o=0.5$, we have $s=12.8$. Using the proper motion of 0.06 +/- 0.02 mas/year from model fitting, we find that there is a superluminal expansion in the CC of 3C263 with $\beta_{app}=1.3$ +/- 0.4. (For an average of the proper motions from all three methods in Section IV, we find $\beta_{app}=1.7$). This is one of the smallest expansions with a superluminal velocity yet found in an extragalactic object. Individual components in some of the well-known superluminals travel at similar speeds, e.g., in 3C345 (Biretta 1985), and general expansion at 2c has been seen in the radio galaxy 3C120 (e.g., Seielstad, et al. 1979). Apparent superluminal motion of this size is not in accord with the predictions of the magnetic dipole model (Bahcall and Milgrom 1980), for which a minimum apparent relative velocity of 4c is expected. The CC of 3C263 is also the weakest object (~170 mJy) to exhibit superluminal motion.

This relatively small superluminal velocity is significant, because we have selected this object as a double-lobed source which is likely to be oriented at fairly large Θ. The velocity could be small due to either a large Θ or a smaller bulk Lorentz factor, γ, than is typically required for the well-known superluminal sources (γ~5-10). Since the rapid motion in the CC of 3C179 demands γ >~5 (from Zensus (1984), adapted to our cosmology), we know that large γ must occur in at least some CCs. As we argue below, 3C179 is likely to be oriented at small Θ, and thus a large β_{app} is not too surprising. Assuming then that 3C263 is not the first object to buck the trend for large γ, the simplest explanation is that the low velocity arises mainly because the source is oriented at a large angle to the line-of-sight. (γ >~5 is needed to hide a hypothetical counterjet as well, if Θ is large.)

We cannot directly measure an expansion velocity in the CC of 3C245 from the present data; a fourth epoch will be necessary to track the component which clearly emerged at the third epoch. However, if we make the simple assumption that this new component has traveled at constant velocity and began its motion at the origin (i.e., at the peak of the core component on the map), then we derive a proper motion of 0.15 mas/year (assuming the time of outburst in Section IV). At a redshift z=1.029, this corresponds to $\beta_{app}=4.2$. (Using the change in separation for the double models at the second and third epochs gives $\beta_{app}=3.4$.) Further, there was a marked decrease in the flux density of the broad core component (second epoch) as it became resolved as a double (third epoch). At both epochs, the characteristic size of the core was ~0.35 mas, with the brightness change occurring over ~1.2 years. From these figures, we derive an internal expansion speed of ~8c. Therefore, we have some evidence that superluminal expansion is occurring in 3C245, and that it is taking place at a considerably larger speed than in 3C263. It is interesting to note that β_{app}~5 for 3C179 (Zensus (1984), using the same cosmology applied here), and that this object is similar to 3C245 in that: (1) about half of the high-frequency total flux density for the source is in the CC; (2) the CC is variable; and (3) the source is of small projected overall size. These morphological characteristics suggest that both 3C245 and 3C179 are probably aligned at small Θ, and therefore might be expected to exhibit large superluminal motions.

The minimum bulk Lorentz factor, γ, required to explain the observed motion in 3C263 is 1.7 ($\Theta(\gamma=1.7)=36^{\circ}$), consistent with the value of <~2 derived by Scheuer and Readhead (1979) for the CCs of "classical doubles." If there is indeed motion in 3C245 with ~4c, then the minimum γ is ~4, but of course we have no solid evidence for this velocity at present. It is interesting to speculate, however, that if the velocity we guess here for 3C245 is correct, and if both objects have the same γ~4, then it is easy to explain the different apparent velocities on the basis of different orientations alone. In this case, one would expect the observed velocity in 3C263 if this large source with moderate CC strength were oriented at $\Theta \sim 70^\circ$. The larger velocity in 3C245 would arise if this small source with a dominant CC were oriented at $\Theta \sim 15^\circ$. This small Θ for 3C245 would present no problem when deprojecting the apparent linear size; in fact, 3C245 would still turn out to be intrinsically smaller than 3C263.

The CC of 3C263 has an inverted spectrum at centimeter wavelengths, with $\alpha \sim -0.4$, suggesting that it may be dominated by an optically thick component with a spectral turnover at even shorter wavelengths. The CC of 3C245, however, has a rather steep spectral index ($\alpha \sim 0.5$), which might be accounted for if this object is oriented at a small angle to the line-of-sight. A strongly enhanced, steep-spectrum jet directed at small Θ would dominate the flux density of the CC. 3C245 is therefore an excellent candidate for higher frequency VLBI observations (22 GHz), better to resolve the components and obtain their spectra for the purpose of positively identifying the flat-spectrum core and steep-spectrum jet. Zensus (1984) has shown that the weaker VLBI component in 3C179 has the steeper spectral index and lies on the same side of the core as the large-scale jet.

We have measured one velocity and deduced another in the complete sample of objects defined in Chapter 1. It will take several years to observe enough of the objects at multiple epochs for making statistically meaningful statements about the distribution of apparent velocities. But the first object has turned out to be mildly superluminal. This is expected for a weak central component on the simple beaming model, and can also explain the observed lack of a counterjet. We note that in the absence of even mild superluminal expansion in objects at large θ, one would have to postulate two separate explanations for one-sidedness (Begelman, Blandford, and Rees 1984). We have dispelled the fear that such motion would not be detectable in weak central components because a cocoon surrounding the jet may have dominated over the jet emission (Blandford and Königl 1979). And, with the possibility of a much larger expansion velocity in 3C245, it seems that there is no need yet to abandon the simple beaming model based on the first two objects studied. A narrow jet moving relativistically at different angles to the line-of-sight in the two objects can readily account for the different observed velocities. Zensus and Porcas (1986) note that the common occurrence of structural variations in the CCs of the double-lobed quasars in their sample causes difficulties for the simple beaming model. However, we must wait and see how strongly superluminal the motions turn out to be in both samples, in order to assess quantitatively any shortcomings of the simple model.

VI. Conclusions

Observations of the central components of 3C245 and 3C263 at three epochs have revealed sharp structural variations in both objects. We have found superluminal motion with β_{app}~1.5 in 3C263 and suggest that motion with β_{app}~4 may be occurring in 3C245, but this must be confirmed by direct observation. These results show that it is, and will be, possible to measure velocities in this type of object. Although it is undoubtedly premature to draw any firm conclusions, the simple beaming model can account for the different apparent velocities, if the bulk Lorentz factor is typically ~4.

References

Bahcall, J.N., and Milgrom, M. 1980, *Ap.J.*, **236**, 24.

Begelman, M.C., Blandford, R.D., and Rees, M.J. 1984, *Rev.Mod.Phys.*, **56**, 255.

Biretta, J.A. 1985, Ph.D. dissertation, California Institute of Technology.

Blandford, R.D., and Königl, A. 1979, *Ap.J*, **232**, 34.

Cohen, M.H., and Unwin, S.C. 1982, in IAU Symposium 97, *Extragalactic Radio Sources*, ed. D.S. Heeschen and C.M. Wade (Dordrecht:Reidel), p.345.

Porcas, R.W. 1981, *Nature*, **294**, 47.

Rogers, A.E.E., et al. 1983, *Science*, **219**, 51.

Scheuer, P.A.G., and Readhead, A.C.S. 1979, *Nature*, **277**, 182.

Seielstad, G.A., Cohen, M.H., Linfield, R.P., Moffet, A.T., Romney, J.D., Schilizzi, R.T., and Shaffer, D.B. 1979, *Ap.J.*, **229**, 53.

Seielstad, G.A., Readhead, A.C.S., and Pearson, T.J. 1983, *Pub.A.S.P.*, **95**, 842.

Unwin, S.C. 1982, in IAU Symposium 97, *Extragalactic Radio Sources*, ed. D.S. Heeschen and C.M. Wade (Dordrecht:Reidel), p.357.

Whitney, A.R. 1982, "The Mark III Correlator: Design, Operation, and Productivity," Northeast Radio Observatory Corporation, Haystack Observatory document.

Zensus, J.A. 1984, Ph.D. dissertation, Münster.

Zensus, J.A., and Porcas, R.W. 1984, in IAU Symposium 110, VLBI and Compact Radio Sources, ed. R. Fanti, K. Kellermann, and G. Setti (Dordrecht:Reidel), p.163.

Zensus, J.A., and Porcas, R.W. 1986, in IAU Symposium 119, Quasars, in press.

Table 1

The Telescopes

Station[1]	Diameter(m)	T_{sys}	Peak K/Jy
B	100	100	0.88
L	32	110	0.13
K	36	115	0.16
G	43	65	0.18
F	26	130	0.05
O	40	70	0.21

1. See Chapter 2, Table 2 for station codes. L=Medicina, Italy 32m.

Table 2

Journal of Observations

Date of Observation	Source	Mode	τ(sec)	Stations[1]
1 October 1982	3C263	A	120	BKG(F)O
9 February 1983	3C245	B	120	KGFO
11 October 1983	3C245	B	120	BKGFO
11-13 October 1983	3C263	A/B	250	BK(GF)O
9 December 1984	3C263	B	390	BLKGO
12 December 1984	3C245	B	60	BKGFO

1. ( ) indicates data not used in analysis.

Table 3

Results for 3C263 at First Epoch

Model-fitting

Component	S(mJy)	Radius(mas)	PA	Axis(mas)
A	95^{+20}_{-10}	0	0	<0.2
B	74^{+20}_{-20}	$0.48^{+0.02}_{-0.02}$	110^{+2}_{-2}	<0.3

Hybrid Mapping

Component	S(mJy)	Radius(mas)	PA
A	95^{+6}_{-6}	0	0
B	58^{+2}_{-2}	$0.48^{+0.01}_{-0.01}$	110^{+1}_{-1}

MEM

Component	Peak Flux (mJy/mas^2)	Radius(mas)	PA
A	2460^{+350}_{-350}	0	0
B	930^{+400}_{-400}	$0.50^{+.02}_{-.02}$	110^{+1}_{-1}

Table 4

Results for 3C263 at Second Epoch

Model-fitting

Component	S(mJy)	Radius(mas)	PA	Axis(mas)
A	86^{+15}_{-5}	0	0	<0.2
B	45^{+15}_{-5}	$0.53^{+0.02}_{-0.02}$	108^{+2}_{-2}	<0.3

Hybrid Mapping

Component	S(mJy)	Radius(mas)	PA
A	85^{+2}_{-2}	0	0
B	42^{+1}_{-1}	$0.54^{+0.01}_{-0.01}$	108^{+1}_{-1}

MEM

Component	Peak Flux (mJy/mas^2)	Radius(mas)	PA
A	2053	0	0
B	493	0.57	110

Table 5

Results for 3C263 at Third Epoch

Model-fitting

Component	S(mJy)	Radius(mas)	PA	Axis(mas)
A	103^{+15}_{-5}	0	0	<0.1
B	52^{+10}_{-10}	$0.61^{+0.02}_{-0.04}$	109^{+2}_{-2}	0.5+0.1[1]

Hybrid Mapping

Component	S(mJy)	Radius(mas)	PA
A	108^{+2}_{-2}	0	0
B	34+3	$0.63^{+0.02}_{-0.02}$	108^{+1}_{-1}

MEM

Component	Peak Flux (mJy/mas^2)	Radius(mas)	PA
A	3310^{+310}_{-310}	0	0
B	550^{+180}_{-180}	$0.71^{+.02}_{-.02}$	109^{+1}_{-1}

1. Component B is an elliptical gaussian, with axial ratio <0.7 and PA=103+/-20.

Table 6

Results for 3C245 at First Epoch

Model-fitting

Component	S(mJy)	Radius(mas)	PA	Axis(mas)
A	586+30 -30	0	0	<0.3
B	60+100 -30	1.1+0.4 -0.2	-81+30 -30	<1.5

Hybrid Mapping

Component	S(mJy)	Radius(mas)	PA
A	581+5 -5	0	0
B	44+12 -12	1.18+0.06 -0.06	-71+5

MEM

Component	Peak Flux (mJy/mas^2)	Radius(mas)	PA
A	1460+337 -337	0	0
B	41+33 -33	1.39+.06 -.06	-77+9 -9

Table 7

Results for 3C245 at Second Epoch

Model-fitting

Component	S(mJy)	Radius(mas)	PA	Axis(mas)
A	587^{+50}_{-50}	0	0	0.33+0.03
B	69^{+30}_{-30}	$1.0^{+0.4}_{-0.1}$	-74^{+20}_{-30}	<0.4

Hybrid Mapping

Component	S(mJy)	Radius(mas)	PA
A	577^{+7}_{-7}	0	0
B	51^{+6}_{-6}	$1.16^{+0.07}_{-0.07}$	-64^{+4}_{-4}

MEM

Component	Peak Flux (mJy/mas^2)	Radius(mas)	PA
A	1590^{+90}_{-90}	0	0
B	58^{+26}_{-26}	$0.98^{+.04}_{-.04}$	-70^{+6}_{-6}

Table 8

Results for 3C245 at Third Epoch

Model-fitting

Component	S(mJy)	Radius(mas)	PA	Axis(mas)
A1	224+50 -30	0	0	<0.3
A2	175+20 -30	0.40+0.05 -0.02	-76+8 -8	<0.3
B	106+100 -80	1.3+0.5 -0.5	-66+20 -40	<3

Hybrid Mapping

Component	S(mJy)	Radius(mas)	PA
A1	414+/-7	0	0
A2		0.34+.02 -.02	-68+4 -4
B	23+5 -5	1.28+.15 -.15	-77+16 -16

MEM

Component	Peak Flux (mJy/mas^2)	Radius(mas)	PA
A1	1039	0	0
A2	800	0.33	-69
B	79	1.35	-72

Figure Captions

Fig. 1 - Hybrid maps of the central component of 3C263 at three epochs at conventional resolution; beam of FWHM=0.5 mas shown cross-hatched; scale is 0.5 mas/tick; contours are -2,2,5,10,20,30,40,50,60,70, 80,90,100 mJy/beam.

(a) October 1982: peak is 95.7 mJy/beam.

(b) October 1983: peak is 83.3 mJy/beam.

(c) December 1984: peak is 105 mJy/beam.

Fig. 2 - Hybrid maps of the central component of 3C263 at three epochs with "super-resolution"; beam of FHWM=0.35 mas shown cross-hatched; scale is 0.5 mas/tick; contours are -2,2,5,10,20,30,40,50,60,70, 80,90,100 mJy/beam.

(a) October 1982: peak is 81.9 mJy/beam.

(b) October 1983: peak is 80.4 mJy/beam.

(c) December 1984: peak is 100 mJy/beam.

Fig. 3 - Maximum entropy maps of the central component of 3C263 at three epochs; scale is 0.2 mas/vertical tick.

(a) October 1982: contours are 1,5,15,25,40, 60,80,100 per cent; peak is 2710 mJy/mas^2.

(b) October 1983: contours are 2,5,10,20,40, 60,80,100 per cent; peak is 1816 mJy/mas^2.

(c) December 1984: contours are 0.5,2.5,7.5, 17.5,27.5,40,60,80,100 per cent; peak is 3095 mJy/mas^2.

Fig. 4 - Hybrid maps of the central component of 3C245 at three epochs at conventional resolution; beam FWHM shown cross-hatched; scale is 1.0 mas/tick.

(a) February 1983: beam is 3.0 x 0.8 mas, PA=170°; contours are -1,1,5,10,20,30, 40,50,60,70,80,90 per cent; peak is 574 mJy/beam.

(b) October 1983: beam is 3.0 x 0.5 mas, PA=170°; contours are -2.5,2.5,5,7.5, 10,20,30,40,50,60,70,80,90 per cent; peak is 486 mJy/beam.

(c) December 1984: beam is 3.0 x 0.5 mas, PA=170°; contours are -2.5,2.5,4,6,10, 20,30,40,50,60,70,80,90 per cent; peak is 285 mJy/beam.

Fig. 5 - Hybrid maps of the central component of 3C245 at three epochs with "super-resolution"; beam FWHM shown cross-hatched; scale is 0.5 mas/tick.

(a) February 1983: beam is 1.5 x 0.4 mas, PA=170°; contours are -1,1,5,10, 20,30,40,50,60,70,80,90 per cent; peak is 570 mJy/beam.

(b) October 1983: beam is 1.5 x 0.25 mas, PA=170°; contours are -2.5,2.5,5, 7.5,10,20,30,40,50,60,70,80,90 per cent; peak is 405 mJy/beam.

(c) December 1984: beam is 1.5 x 0.24 mas, PA=170°; contours are -2.5,2.5,5, 7.5,10,20,30,40,50,60,70,76,80,90 per cent; peak is 166 mJy/beam.

Fig. 6 - Maximum entropy maps of the central component of 3C245 at three epochs; scale is 0.2 mas/vertical tick.

(a) February 1983: contours are 2,3,4,10,20, 40,60,80,100 per cent; peak is 1699 mJy/mas^2.

(b) October 1983: contours are 2,3.5,5,10,20, 40,60,80,100 per cent; peak is 1523 mJy/mas^2.

(c) December 1984: contours are 2,5,7,10,20, 30,40,50,60,70,77,82,90,100 per cent; peak is 1039 mJy/mas^2.

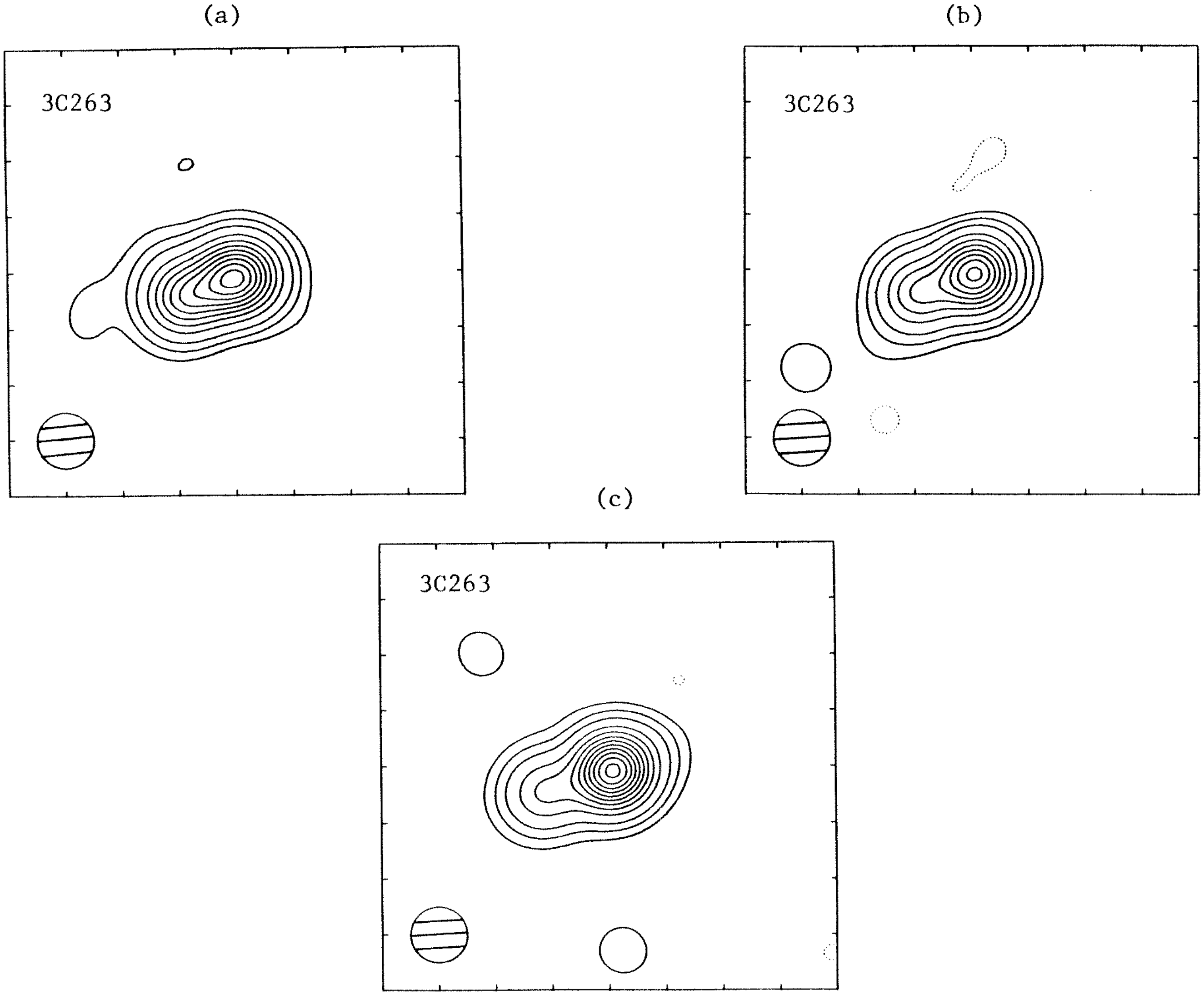

Figure 1

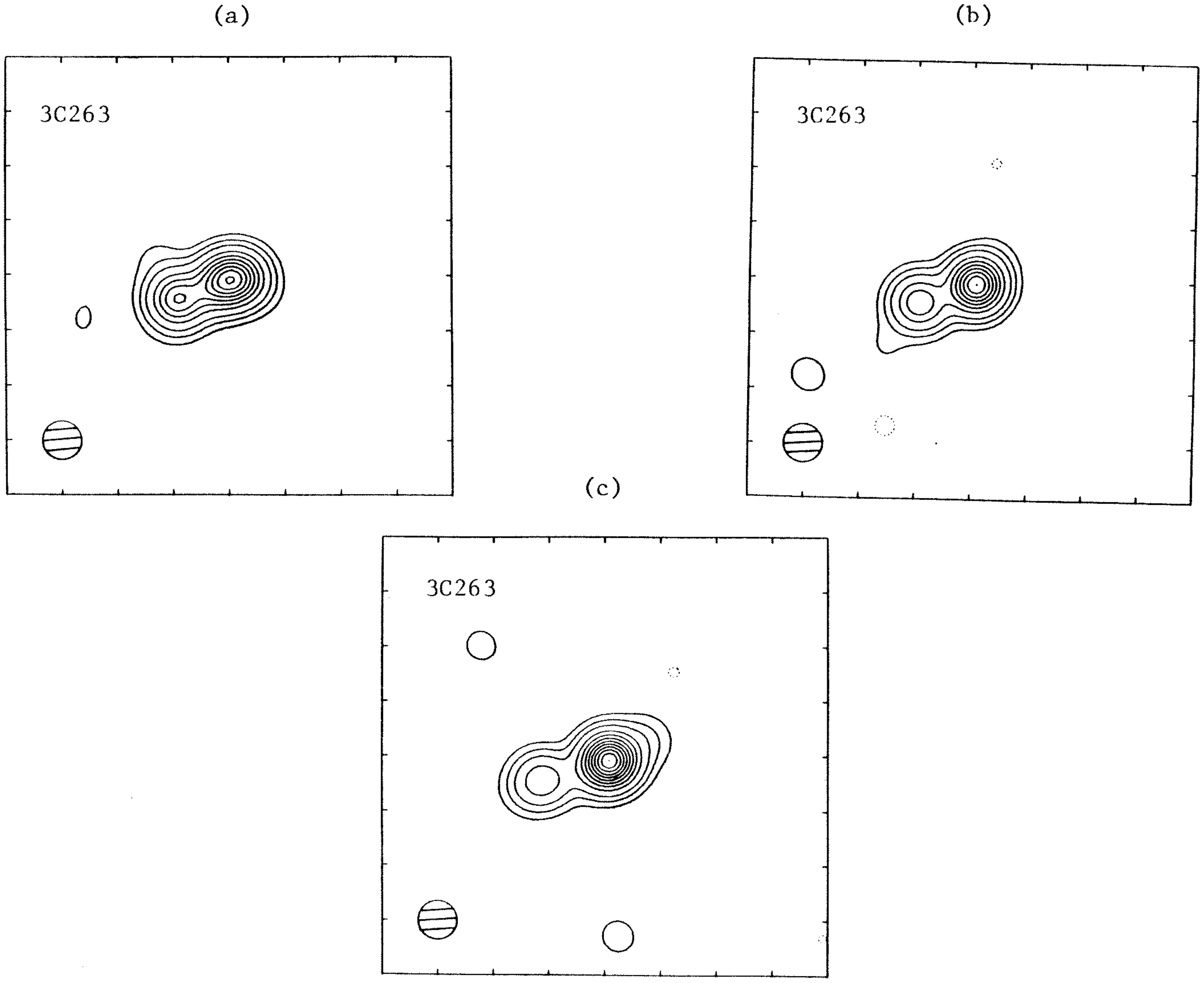

Figure 2

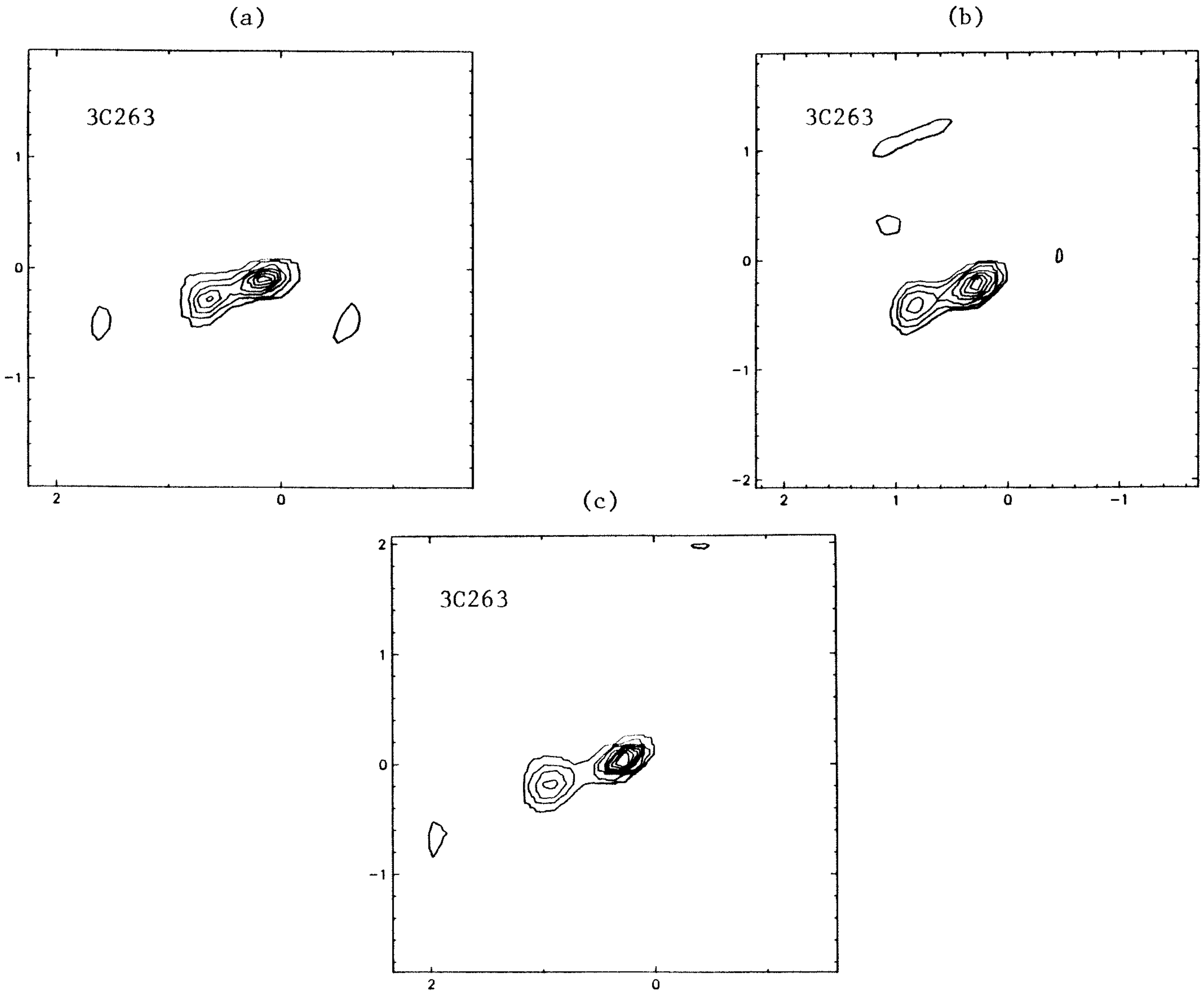

Figure 3

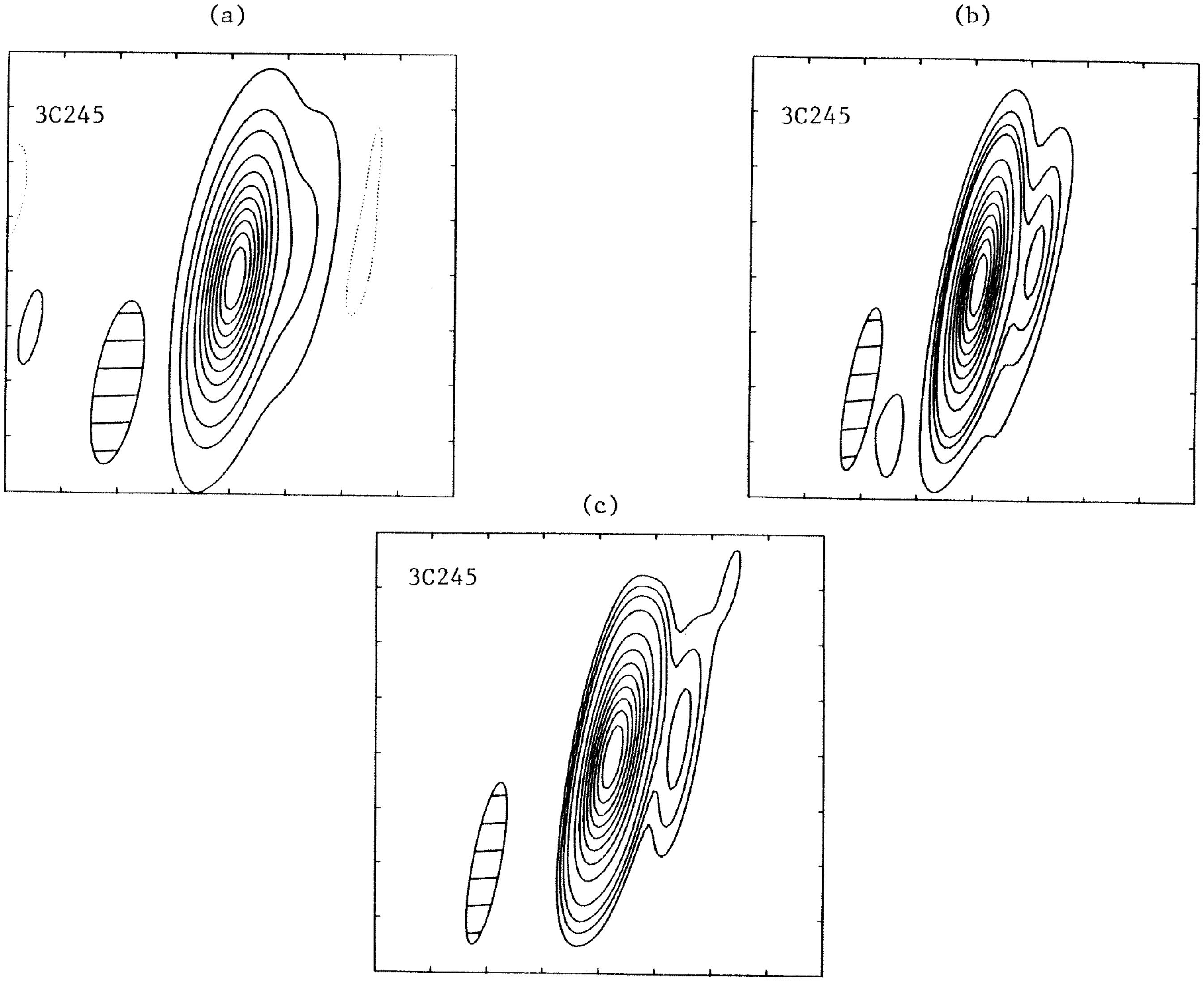

Figure 4

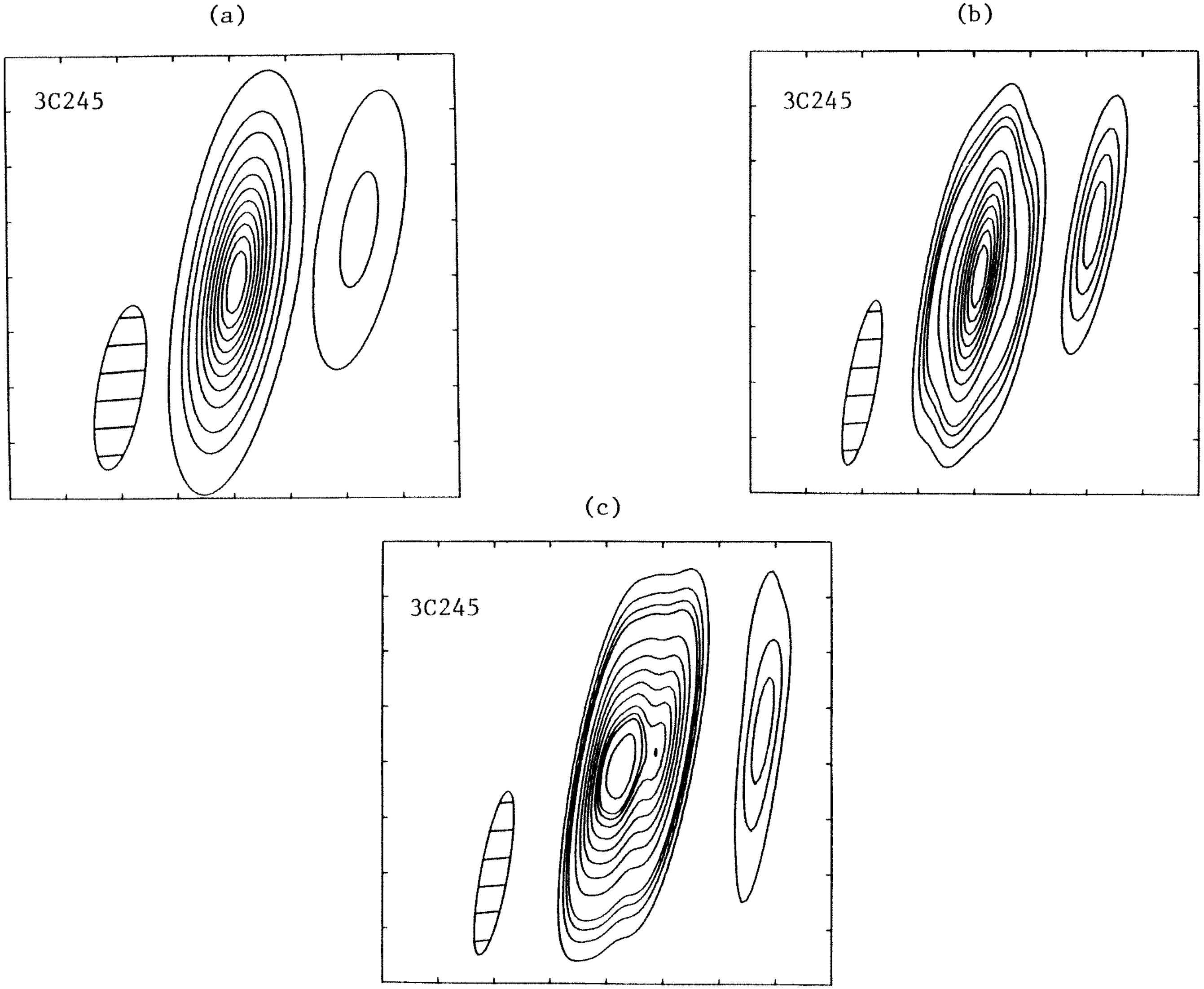

Figure 5

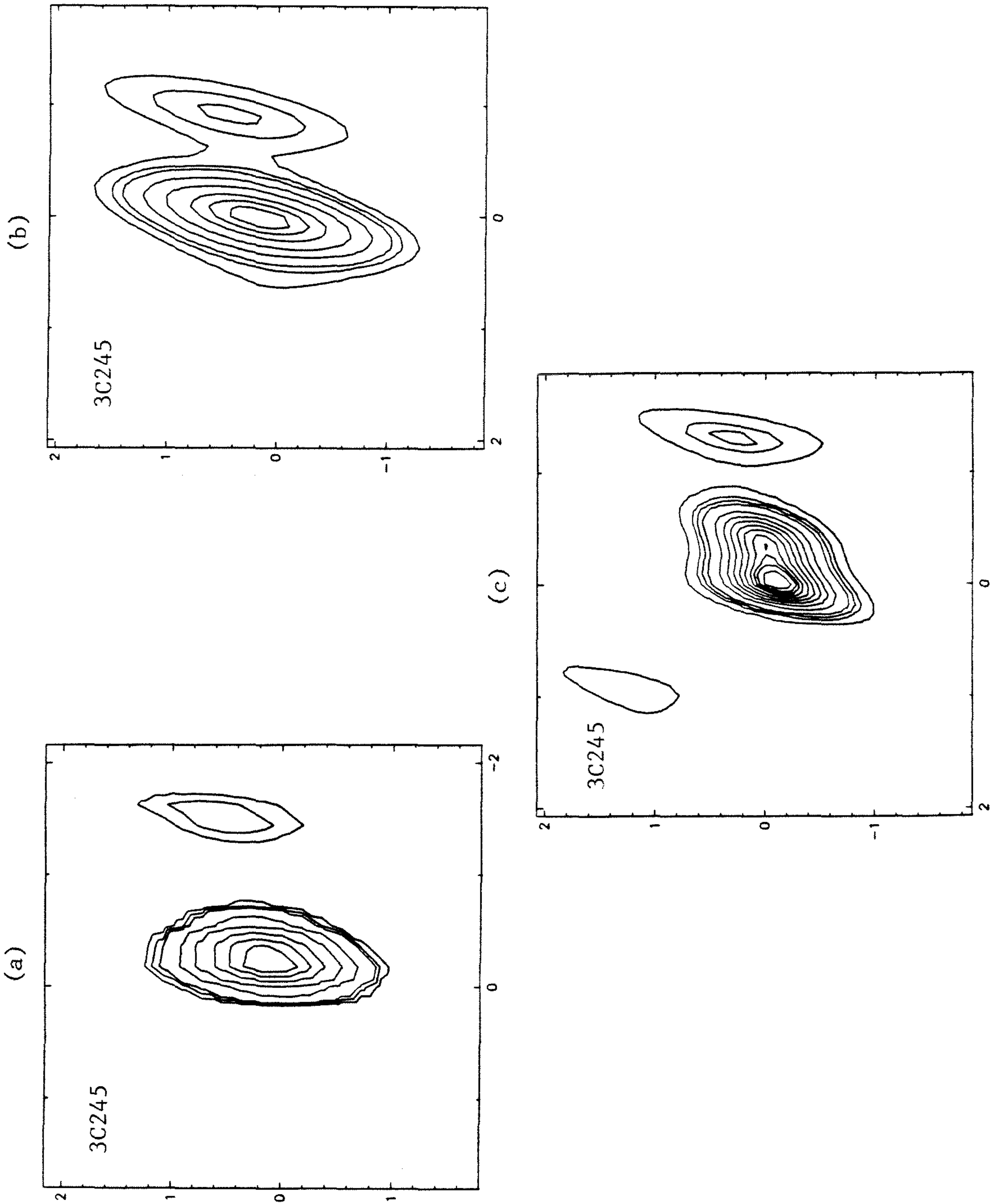

Figure 6

CHAPTER 4

PHYSICAL CONDITIONS IN THE CENTRAL COMPONENTS

Summary

We present some rough estimates of the physical conditions in the quasar central components. The peak brightness temperatures are all well below the inverse Compton limit. Synchrotron calculations do not provide tests sensitive to departures from energy equipartition. The minimum pressures place constraints on the density and temperature of a confining gas cloud which make thermal confinement seem unlikely. Although we have detected superluminal motion in 3C263, and 3C245 is also probably superluminal (see Chapter 3), crude self-Compton X-ray calculations are not useful tests of bulk relativistic motion in either object.

I. Introduction

We can make some rough estimates of the physical conditions in the quasar central components using the data in Chapters 2 and 3. The data do not exist which would permit making very accurate calculations of the particle energy, magnetic field strength, internal pressure, and other quantities of interest. However, with a few plausible assumptions, we can proceed with these calculations. We first determine peak brightness temperatures. Next, physical information is derived using synchrotron theory, first on the basis of equipartition and minimum energy arguments and second assuming self-absorption turnovers in the core components. Finally, crude estimates of the minimum Doppler factors for 3C263 and 3C245 are given, based on inverse Compton X-ray arguments.

II. Peak Brightness Temperatures

The peak brightness temperature in a compact synchrotron source is limited to $<\sim 10^{12}$ K, where the onset of the inverse Compton "catastrophe" occurs. It is therefore of interest to see how close to this limit the observed peak brightness temperatures are in the central components. This calculation requires knowledge of the angular size at the frequency where the flux density is measured:

$$T_b\,(K) = 1.77\times 10^{12}\,\frac{S_\nu(Jy)\,(1+z)}{\nu^2(GHz)\,\psi^2(mas)} \quad . \qquad (1)$$

Unfortunately, in almost all cases, we have only upper limits to the angular size. Thus we can obtain only lower limits to T_b. Further, since the angular sizes have been determined using Gaussian components but we assume homogeneous, spherical sources throughout the analysis in this chapter, a correction factor of 1.8 is applied to give an approximate value for a homogeneous sphere (Marscher 1983). The components are barely resolved, so this approximation is valid.

The flux densities and angular sizes from model fitting are listed in Table 1, along with the lower limits to T_b. In no case does T_b approach 10^{12} K; the largest value, for component A in 3C263 at the third epoch, is 8×10^{10} K. Only if the actual sizes are at least $\gtrsim 5$ times smaller than the upper limits does a problem arise; in that case modest beaming would eliminate the problem, through the Doppler factor δ ($T_b \propto 1/\delta$). It is also possible that there may be a different mechanism which acts as a "thermostat" in these objects, limiting T_b to $\sim 10^{11}$ K.

III. Equipartition and Minimum Energy

We assume that the observed radio emission is incoherent synchrotron radiation produced by relativistic electrons gyrating in a tangled magnetic field. If we further assume that there is equipartition of energy between relativistic particles and magnetic fields (or a minimum energy configuration, which is nearly identical), several important physical quantities can be derived. The formulae used here are taken from the treatments by Moffet (1975) and Linfield (1982).

For a power-law distribution of electron energies, which leads to a power-law for the radio emission, the energy in the electrons is

$$U_e(\text{ergs}) = 1.057\times 10^{12} f(\alpha, \nu_1, \nu_2)\, L_R B^{-3/2} = A L_R B^{-3/2}, \qquad (2)$$

where $f(\alpha, \nu_1, \nu_2)$ is a function of the radio spectral index, α, and the lower and upper cutoff frequencies, ν_1 and ν_2. L_R is the radio luminosity for an optically thin component (ignoring any beaming effects), and B is the magnetic field (all cgs units). We neglect any contribution to the particle energy from protons. The energy stored in the magnetic field is

$$U_m = VB^2/8\pi, \qquad (3)$$

where V is the source volume. The total energy U_e+U_m has a minimum, which is very close to the equipartition value, of

$$U_{min} = 0.5\,(AL_R)^{4/7}\,V^{3/7} \approx U_{eq}. \qquad (4)$$

The equipartition magnetic field is

$$B_{eq}(\text{Gauss}) = 2.51\,(AL_R/V)^{2/7}, \qquad (5)$$

while the minimum pressure due to particles and fields can be expressed as

$$P_{min}(dynes/cm^2) = 0.61\ U_{min}/V\ . \qquad (6)$$

We can also calculate the time for an electron radiating at a given frequency ν_0 to lose half its energy from

$$t(years) = 3.5 \times 10^{10} / B_{eq}^{3/2}(\mu G)\ \nu_0^{1/2}(MHz)\ . \qquad (7)$$

In Table 2 we give the luminosity and volume (assuming spherical geometry) for each component in all sources, assuming an Einstein-deSitter universe with H_0=75 km/sec/Mpc and q_0=0.5. Cutoff frequencies ν_1=10 MHz and ν_2=100 GHz have been used in calculating the luminosity, assuming a power law with α=0 for the "cores" (component A) and α=0.3 for the "jets" (component B); these are the approximate spectral indices for the two VLBI components in the nucleus of 3C179 (Zensus 1984). These same spectral indices have been applied in evaluating other quantities which depend upon α, since no spectra are available for the VLBI components. The other entries in Table 2 are the equipartition energy and magnetic field, minimum pressure, and synchrotron lifetime for an electron radiating at 10.7 GHz in the source frame.

The lower limits to the equipartition magnetic fields are quite similar to those found by Linfield (1982) in the central components of radio galaxies, with B~0.01-0.1 Gauss and with the core typically having a somewhat stronger field than the jet. The upper limits to the equipartition energies are roughly an order-of-magnitude greater than those in the radio galaxies. Although there is not a direct scaling, this is consistent with the fact that quasar central components are observed to be typically ~10 times as powerful as those in radio galaxies.

The minimum pressures are often $\sim 10^{-4}$ dynes/cm^2, implying $nT \gtrsim 10^{12}$ cm^{-3}K if the components are confined by a surrounding gas cloud. This implies very large densities and/or temperatures in the gas cloud, in the absence of which the components must either be confined by another mechanism (e.g., magnetic self-confinement) or expand freely.

The upper limits to the synchrotron lifetimes are many times the light travel time across the components or the travel time from the cores to the jets. Thus there is no indication here of relativistic velocities. This would change if the magnetic fields are actually significantly larger than we estimate.

IV. Synchrotron Self-absorption

Physical information on a compact radio source can be gained from analysis of the spectrum. The magnetic field can be calculated directly from the flux density and angular size at the spectrum turnover. Scott and Readhead (1977) have shown that one can predict an equipartition angular size at the turnover; differences between this size and the observed size point towards departures from equipartition, and can be used to tell if the particle or field energies dominate.

The quasar central components must contain optically thick components which appear self-absorbed at the highest observed frequencies. This is because several objects (3C207, 3C212, and 3C263; see references in Table 1 of Chapter 1) have inverted spectra ($\alpha \sim -0.2$) between 5 and 15 GHz, which may be due to an optically thick component whose spectrum peaks at a frequency above 15 GHz. This component is likely to be the compact VLBI core, component A, although we have no spectral information for any of the individual VLBI components to substantiate this.

For this discussion, we assume that the core is self-absorbed and take the peak of the spectrum to be at the highest observed frequency, 15 GHz. The assumed VLBI flux densities at 10.7 GHz are extrapolated to 15 GHz using $\alpha = -0.2$. Assuming an optically thin spectral index of 0.3 and applying a correction to the flux density at the peak from Scott and Readhead (1977) gives the equipartition angular size

$$\psi_{eq}(\mathrm{mas}) = 4000 \left[1 - (1+z)^{-1/2} \right]^{-.0588} (1+z)^{.459} S(\mathrm{Jy})^{.471} \nu(\mathrm{MHz})^{-1.01} , \qquad (8)$$

where minor differences in assumptions by Scott and Readhead (1977) and those made here (e.g., choice of H_0, etc.) have only a small effect on ψ_{eq}. We can express the magnetic field strength, total energy, and ratio of electron to magnetic field energy densities in terms of the ratio, η, of observed to equipartition angular size:

$$\eta = \psi_{obs}/\psi_{eq} , \qquad (9.1)$$

$$B/B_{eq} = \eta^{4} , \qquad (9.2)$$

$$U/U_{eq} = \tfrac{1}{2}\eta^{11}(1+\eta^{-17}), \qquad (9.3)$$

$$u_e/u_m = \eta^{-17} . \qquad (9.4)$$

The values of ψ_{eq} and η for the core components are given in Table 3. The equipartition angular sizes are all significantly smaller than the observed upper limits, but not drastically so. If the actual angular sizes are near the observed upper limits, then the fields dominate and the total energies are very large. However, based on these rough calculations, we cannot tell if there is any departure from equipartition in the VLBI cores. It is often found that the particle energy dominates in compact components (e.g., Biretta 1985). If the actual angular sizes are those for equipartition, then the brightness temperatures are still well below 10^{12} K.

V. Inverse Compton X-Rays

It is possible to make deductions about the minimum Doppler factor by considering the self-Compton X-ray emission from a compact radio source. We have two objects from Chapter 3 which are either clearly (3C263) or likely (3C245) superluminal, and it is of interest to see if any useful estimate of δ_{min} can be made for these objects.

Cohen (1985) gives the following expression for the minimum Doppler factor:

$$\delta_{min} = 10^{-2} e(\alpha) F_h \nu_n^{-p} \psi^{-q} S_x^{-r} (1+z)^s , \qquad (10)$$

where F_n(Jy) and ν_h(GHz) are the flux density and frequency at the intersection of the low- and high-frequency asymptotes for a self-absorbed spectrum, and S_x (ergs/sec/cm^2) is the X-ray flux in the range (0.5-4.5)/(1+z) keV. The constant $e(\alpha)$ and the exponents are all functions of the high-frequency radio spectral index, which will be assumed to be 1. This value of α is chosen as a compromise, because the calculation depends upon the X-ray and high-frequency radio emission having the same spectral index. Based on the Einstein Observatory data for 3C263, the X-ray spectral index is ~1.5, while the compact radio components probably have high-frequency spectral indices < 1. Otherwise, we will make the same assumptions about the spectra of the VLBI cores used in Section IV.

The most interesting case in 3C263 is component A at the third epoch, when the flux density is largest and the upper limit to the angular size smallest. The Einstein Imaging Proportional Counter X-ray flux in the appropriate band is ~2.1 x 10^{-12} ergs/sec/cm^2 (April 1980). The resulting δ_{min} is 0.6; we could obtain δ_{min}=1, for example, by taking the angular size to be ~0.7 of the upper limit.

We know that 3C245 is strongly variable at radio wavelengths. It is probably best to use the 1981 pilot survey data from Chapter 2, which is from a time prior to the 1982 flux outburst, to compare with the Einstein X-ray data from May 1980. The X-ray flux is ~5.4 x 10^{-13} ergs/sec/cm^2, yielding δ_{min}=0.4; we could obtain δ_{min}=1, for instance, by setting the angular size equal to ~0.6 of the upper limit.

These calculations of δ_{min} are too low to be of use and there are several arbitrary assumptions which enter into them. Even if these assumptions were justified, the results do not require bulk relativistic motion in the VLBI components, although it is certainly permitted. It would be possible to raise δ_{min} significantly above 1, if the angular size could be determined on a smaller scale, e.g., that which would be probed by QUASAT.

VI. Conclusions

Rough estimates of the physical conditions in the quasar central components have been presented. The observed peak brightness temperatures are all well below 10^{12} K. It is not possible, based on synchrotron theory arguments, to check for departure from energy equipartition. The minimum pressures suggest that confinement by a thermal gas may be difficult to accomplish. Although superluminal expansion has been demonstrated in Chapter 3 for 3C263 (and is likely for 3C245), self-Compton X-ray calculations are inconclusive regarding the need for bulk relativistic motion. This could easily be changed, however, if the angular sizes are somewhat smaller than the observed upper limits.

References

Biretta, J.A. 1985, Ph.D. dissertation, California Institute of Technology.

Cohen, M.H. 1985, in Proceedings of the Winter School on *Extragalactic Energetic Sources*, ed. V.K. Kapahi (Indian Academy of Sciences:Bangalore), p.1.

Linfield, R. 1982, *Ap.J.*, **254**, 465.

Marscher, A.P. 1983, *Ap.J.(Letters)*, **264**, 296.

Moffet, A.T. 1975, in Stars and Stellar Systems, Vol. **9**, *Galaxies and the Universe*, ed. A. Sandage, M. Sandage, and J. Kristian (Chicago:University of Chicago), p.211.

Scott, M.A., and Readhead, A.C.S. 1977, *M.N.R.A.S.*, **180**, 539.

Zensus, J.A. 1984, Ph.D. dissertation, Münster.

Table 1

Peak Brightness Temperatures

Source	z	Component	S(mJy)	ψ[1](mas)	T_b(10^9K)
3C207	0.684	A	320	<0.3	>29
		B	120	<0.5	>3.9
3C212	1.049	A	130	<0.2	>32
		B	---	----	----
3C245	1.029				
Epoch 1		A	586	<0.3	>63
		B	60	<1.5	>0.26
Epcoh 2		A	587	0.33	52
		B	69	<0.4	>4.2
Epoch 3		A1	224	<0.3	>24
		A2	175	<0.3	>19
		B	106	<3	>0.11
3C249.1	0.311	A	35	<0.15	>9.8
		B	14	<0.3	>0.97
3C263	0.656				
Epoch 1		A	95	<0.2	>19
		B	74	<0.3	>6.5
Epoch 2		A	86	<0.2	>17
		B	45	<0.3	>4.0
Epoch 3		A	103	<0.1	>81
		B	52	0.5	1.6
3C334	0.555	A	54	<0.3	>4.5
		B	36	<0.5	>1.1

1. FWHM of gaussian component; in all calculations, this value is multiplied by 1.8 to approximate the diameter of a homogeneous sphere.

Table 2

Equipartition and Minimum Energy Results

Source	Component	L_R[1]	V[2]	U_{eq}[3]	B_{eq}[4]	P_{min}[5]	t[6]
3C207	A	22	3.6	15	.072	2.5	17
	B	6.9	17	19	.038	0.36	44
3C212	A	18	1.3	8.8	.091	4.1	12
	B	---	---	---	----	---	--
3C245							
Epoch 1	A	80	4.5	34	.098	4.7	11
	B	7.4	560	88	.014	0.096	204
Epoch 2	A	80	6.0	39	.091	4.0	12
	B	8.5	11	17	.045	1.0	34
Epoch 3	A1	31	4.5	20	.074	2.7	17
	A2	22	4.5	20	.076	2.8	16
	B	13	4480	296	.0091	0.041	388
3C249.1	A	0.56	0.16	0.48	.062	1.9	21
	B	0.18	1.3	0.77	.027	0.37	75
3C263							
Epoch 1	A	5.9	1.0	4.1	.071	2.5	18
	B	3.9	3.5	6.9	.050	1.2	30
Epoch 2	A	5.4	1.0	3.9	.070	2.4	19
	B	2.4	3.5	5.2	.043	0.92	38
Epoch 3	A	6.4	0.13	1.8	.13	8.4	7
	B	2.8	16	11	.029	0.42	68
3C334	A	2.5	2.9	3.9	.041	0.82	40
	B	1.4	14	6.8	.025	0.31	85

Notes:

1. Radio luminosity in units of 10^{43} erg/sec.
2. Volume in units of 10^{56} cm^3, upper limit.
3. Equipartition energy in units of 10^{52} ergs, upper limit.
4. Equipartition magnetic field, Gauss, lower limit.
5. Minimum pressure, in units of 10^{-4} dynes/cm^2.
6. Synchrotron lifetime, years, upper limit.

Table 3

Synchrotron Self-absorption Results

Source	Ψ_{eq}(mas)	$\eta=1.8\,\Psi / \Psi_{eq}$
3C207	0.20	<2.7
3C212	0.14	<2.6
3C245		
Epoch 1	0.28	<1.9
Epoch 2	0.28	<2.1
Epoch 3	0.18	<3.0
3C249.1	0.06	<4.5
3C263		
Epoch 1	0.11	<3.2
Epoch 2	0.11	<3.2
Epoch 3	0.11	<1.6
3C334	0.08	<6.7

Appendix A

Error Analysis in Model Fitting

It is very important to have reliable estimates of errors in the parameters used in model fitting to visibility data, especially when attempting to measure small temporal changes in a parameter such as relative separation. Unfortunately, there is not a straightforward, rigorous manner in which to determine these errors because they are not strictly random. Most often systematic discrepancies between a model prediction and the observations dominate the errors.

It is possible to assign errors by visual inspection, although there is admittedly a degree of subjectivity in this method. Nevertheless one can examine fits to data and estimate the error in a given parameter from sections of the fit where the model line runs systematically high or low. It is certainly plausible that one can obtain ~1-~2σ errors in this way, and it depends on the individual and his "feel" for the data what size the errors will be.

The technique of assigning errors visually involves offsetting the parameter to be tested, and then reoptimizing all other parameters to see if an acceptable fit can still be obtained. The error is determined by the point where the fit is judged no longer acceptable.

In practice, there are other considerations which complicate matters. The best-fitting model may not provide a spectacular fit to the data because the source structure is too complicated and/or because of calibration errors. Thus some sections of data may have marginal fits to begin with, and discrepancies appearing at other points in the course of the analysis must be viewed with this in mind. One also arrives at different error estimates if absolute calibration errors are applied in the model fitting.

For the model errors in Chapters 2 and 3, a record was kept of the change in agreement factor (reduced chi-square value) from its optimum value at the point where each parameter was assigned its error. The percentage change is consistently ~5-10 per cent, indicating that the errors are consistently at the same level of significance. It still remains uncertain how to calibrate this level.

Finally, we compared the results from an algorithm for calculating formal errors devised by Giovanni Comoretto (ERRFIT) with those from visual inspection. The formal method requires an estimate of the number of degrees of freedom in the data, which must be something like the number of independent calibration closure errors. If we choose ~2-4 degrees of freedom per station, then the formal and visual errors can generally be made to agree fairly well. This seems a reasonable number of calibration errors per station, as opposed to >~10 suggested for use in the ERRFIT program.

Appendix B

Super-resolution Techniques

There is no question that we can probe the structure in compact radio sources below the conventional resolution limit of ~λ/D. The full width at half maximum of the synthesized beam for VLBI arrays is typically ~0.7λ/D, and this is commonly adopted as a reliable level of resolution. There is no reason to abruptly stop here; structure on still smaller scales will reveal itself in the visibility data. The problem comes in determining how far one can go below the beam size before the potential for misleading results becomes significant.

In hybrid mapping, the CLEAN delta-functions can be convolved with any selected beam. Thus if CLEAN has acted to form distinct peaks of delta-functions on a scale below the standard beam size, convolution with a somewhat smaller beam can reveal that structure. Such "super-resolution" is not universally trustworthy, but with strong signal-to-noise ratios and good (u,v) coverage it can often be trusted down to ~half the conventional beam size. We have not presented any results using a greater super-resolution factor than this in Chapters 2 and 3.

But CLEAN does have failure modes. For instance, it can take a truly smooth jet structure and turn it into a series of knots corresponding to a missing spatial frequency (T. Cornwell, private communication). Thus a super-resolved double might actually be a smooth feature.

Such problems call for an alternative method to check the super-resolving hybrid results.

Maximum entropy is a completely different method which produces super-resolution by taking advantage of the signal-to-noise ratio in high brightness regions. It is often said that MEM maps are difficult to interpret because the resolution varies across the map. But for very compact objects in which one is only trying to delineate a very simple structure, MEM seems ideal for the task. It can thus be used in conjunction with hybrid mapping to confirm the nature of any structure seen below a beam size.

From the MEM mapping runs done for Chapters 2 and 3, several points have become clear about when MEM can fail to converge to a satisfactory solution, and how it can be coaxed to give an excellent fit in other situations. Calibration errors (e.g., gain curve poorly determined) cause difficulties because the current package (S.F. Gull's) has no amplitude correction step; many times corrected data from hybrid mapping were used with success as the input data for MEM. Poor (u,v) coverage (large gaps from missing data) also posed problems which were not easily overcome.

Windowing would often eliminate spurious surrounding features and speed convergence. Windows also helped to achieve good fits on large closure phase triangles that were not obtained otherwise. The price paid sometimes was that low-level spurious features formed at the window edges.

It is true that any mapping technique might find, e.g., a double structure when super-resolving, which is the correct solution if the double is actually in the sky. However, it could be that a different real structure mimics the effect of a simple double, no matter what method is used (M. Cohen, private communication). A series of systematic tests using both the hybrid and maximum entropy mapping techniques is planned for the near future.

Appendix C

Fits of Hybrid Mapping CLEAN Models to the Visibilities

In this appendix, we present fits to the data of the CLEAN delta-functions used in the hybrid maps in Chapters 2 and 3. Fits to the correlated flux density (a), in Jy, and closure phase (b), as a function of Greenwich Sidereal Time (hours), are represented by solid lines in the figures. The vertical segments indicate random errors, except where a "C" indicates that a 5 percent calibration error has been added in quadrature to the noise error. A "G" denotes a case where amplitudes using gain corrections from AMPHI have been plotted. The starting model for the first iteration of mapping is identified by a "P" for a point source and a "D" for a double model. The station symbols are: B=Effelsberg, L=Medicina, K=Haystack, G=Green Bank, F=Fort Davis, and O=Owens Valley.

Fig. 1 - 3C207: G, D.

Fig. 2 - 3C212: G, P.

Fig. 3 - 3C245, Epoch 1: C, G, D.

Fig. 4 - 3C245, Epoch 2: C, D.

Fig. 5 - 3C245, Epoch 3: C, G, D.

Fig. 6 - 3C249.1: G, D.

Fig. 7 - 3C263, Epoch 1: G, D.

Fig. 8 - 3C263, Epoch 2: D.

Fig. 9 - 3C263, Epoch 3: G, P.

Fig. 10 - 3C334: D.

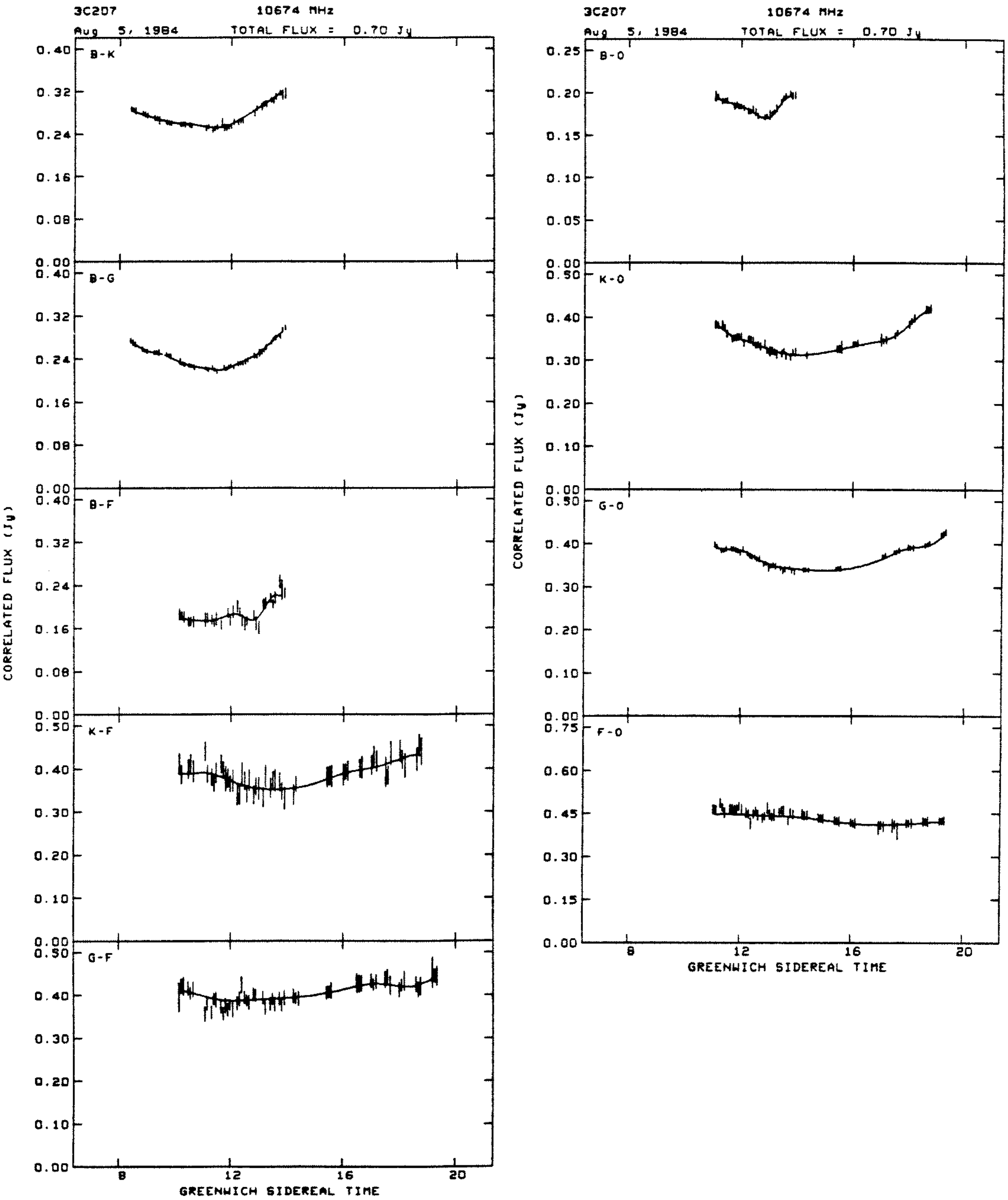
3C207
10674 MHz
Aug 5, 1984
TOTAL FLUX = 0.70 Jy
B-K
B-G
B-F
K-F
G-F
CORRELATED FLUX (Jy)
0.00
0.08
0.16
0.24
0.32
0.40
0.10
0.20
0.30
0.50
8
12
16
20
GREENWICH SIDEREAL TIME
3C207
10674 MHz
Aug 5, 1984
TOTAL FLUX = 0.70 Jy
B-O
K-O
G-O
F-O
CORRELATED FLUX (Jy)
0.05
0.15
0.25
0.45
0.60
0.75
GREENWICH SIDEREAL TIME

Figure 1a

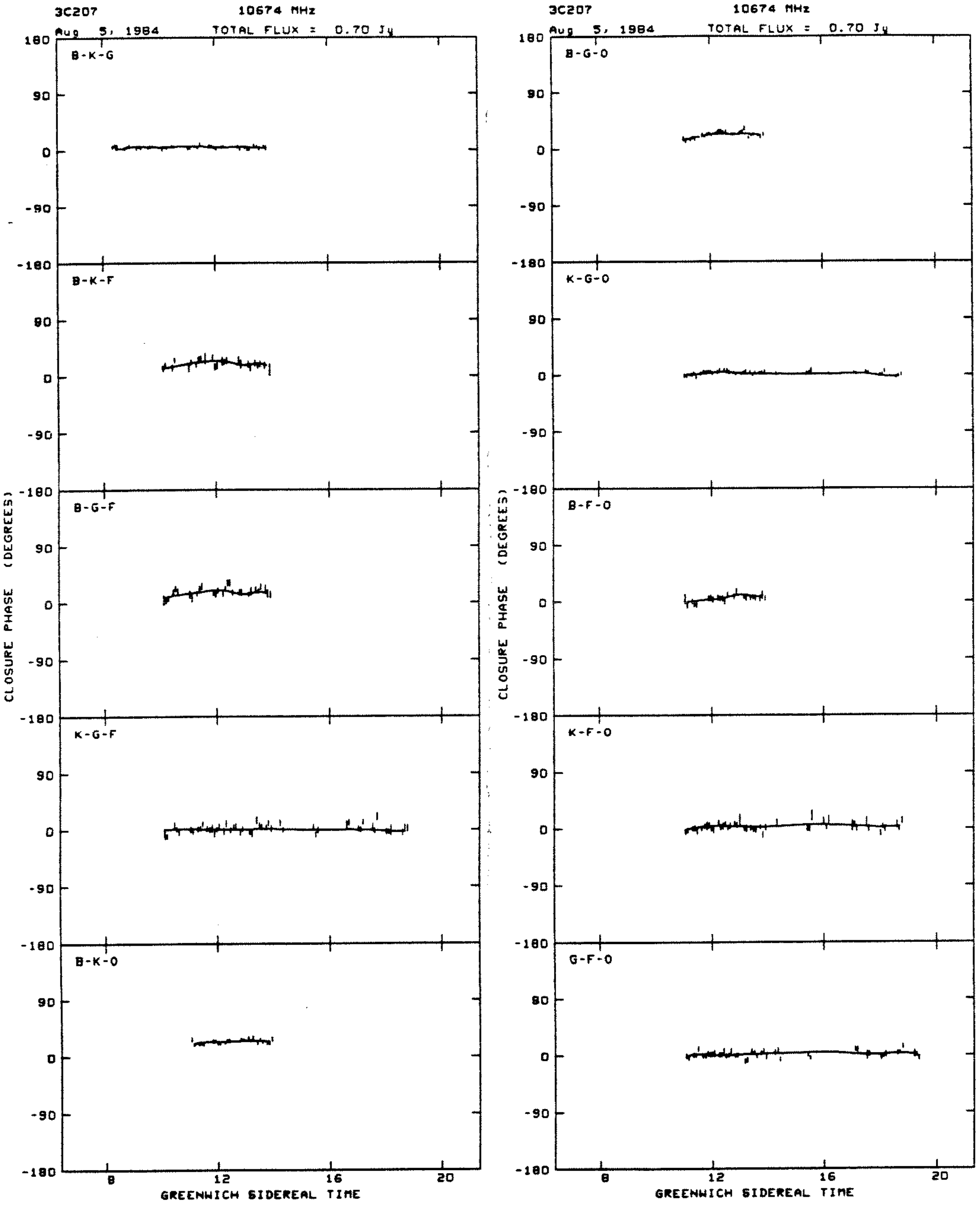
3C207
10674 MHz
Aug 5, 1984
TOTAL FLUX = 0.70 Jy
B-K-G
B-K-F
B-G-F
K-G-F
B-K-O
B-G-O
K-G-O
B-F-O
K-F-O
G-F-O
180
90
0
-90
-180
CLOSURE PHASE (DEGREES)
8
12
16
20
GREENWICH SIDEREAL TIME

Figure 1b

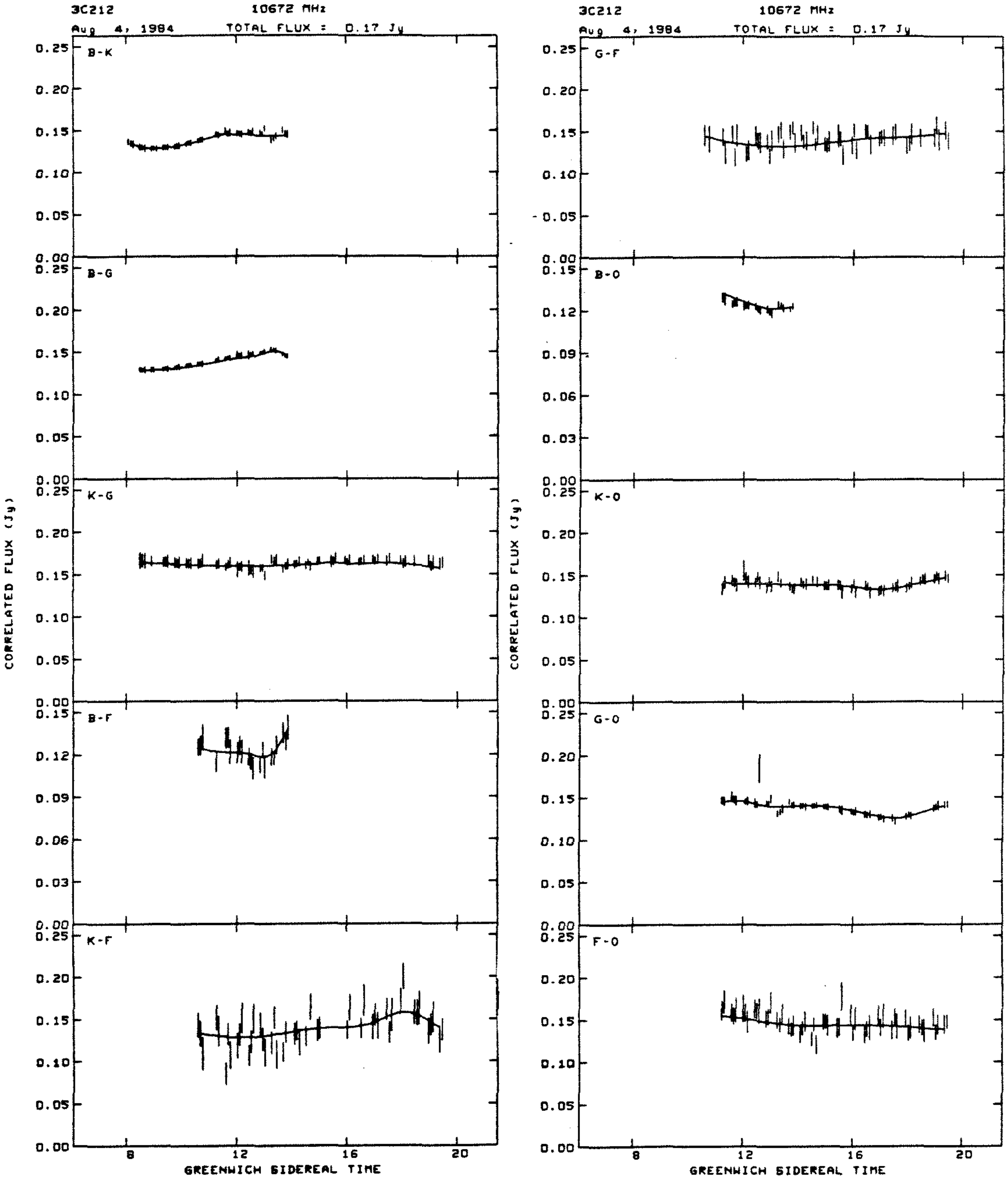
3C212
10672 MHz
Aug 4, 1984
TOTAL FLUX = 0.17 Jy
B-K
B-G
K-G
B-F
K-F
G-F
B-O
K-O
G-O
F-O
CORRELATED FLUX (Jy)
GREENWICH SIDEREAL TIME
8
12
16
20
0.00
0.05
0.10
0.15
0.20
0.25
0.03
0.06
0.09
0.12

Figure 2a

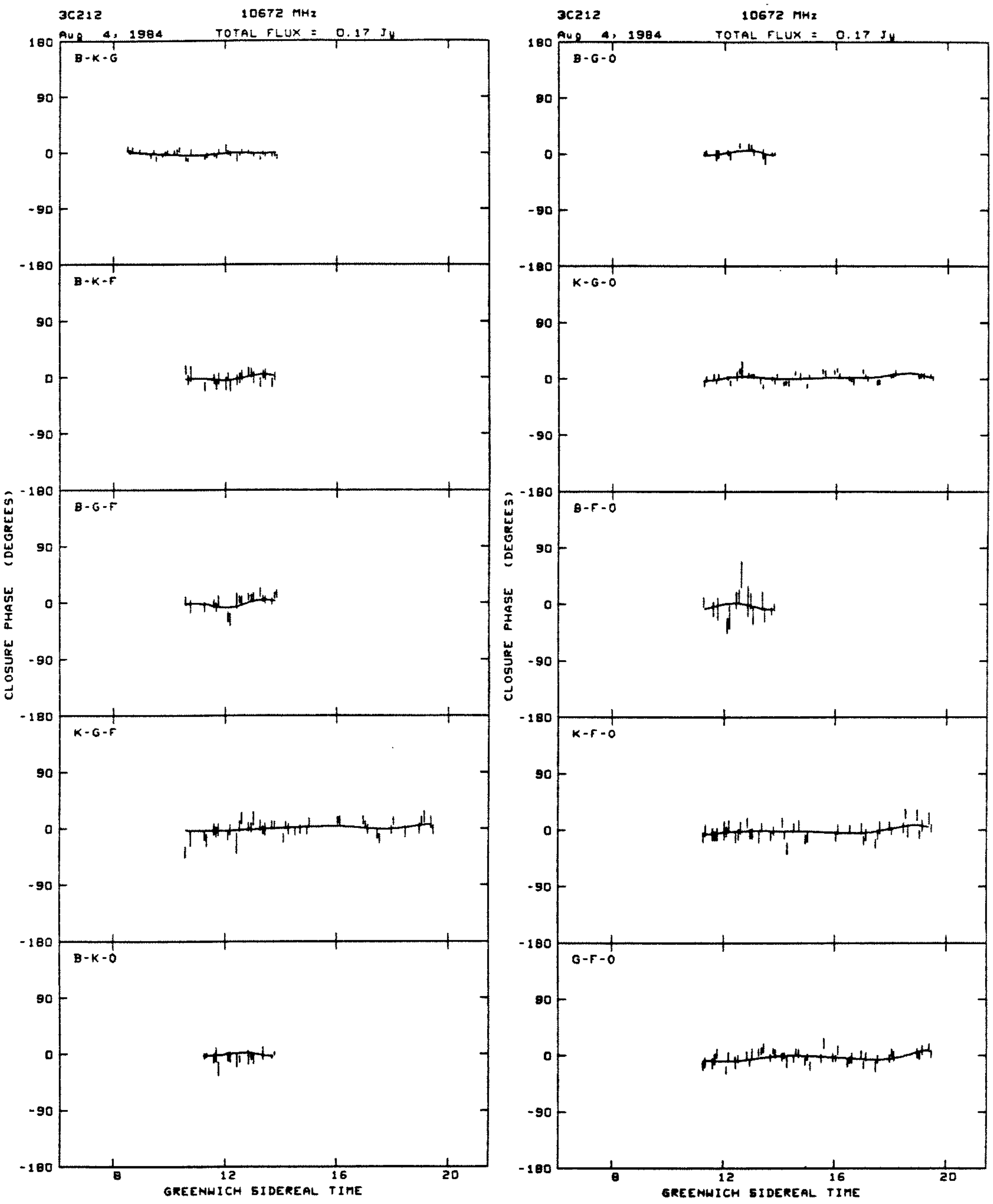
3C212
10672 MHz
Aug 4, 1984
TOTAL FLUX = 0.17 Jy
3C212
10672 MHz
Aug 4, 1984
TOTAL FLUX = 0.17 Jy
B-K-G
B-K-F
B-G-F
K-G-F
B-K-O
B-G-O
K-G-O
B-F-O
K-F-O
G-F-O
CLOSURE PHASE (DEGREES)
CLOSURE PHASE (DEGREES)
180
90
0
-90
-180
8
12
16
20
GREENWICH SIDEREAL TIME
GREENWICH SIDEREAL TIME

Figure 2b

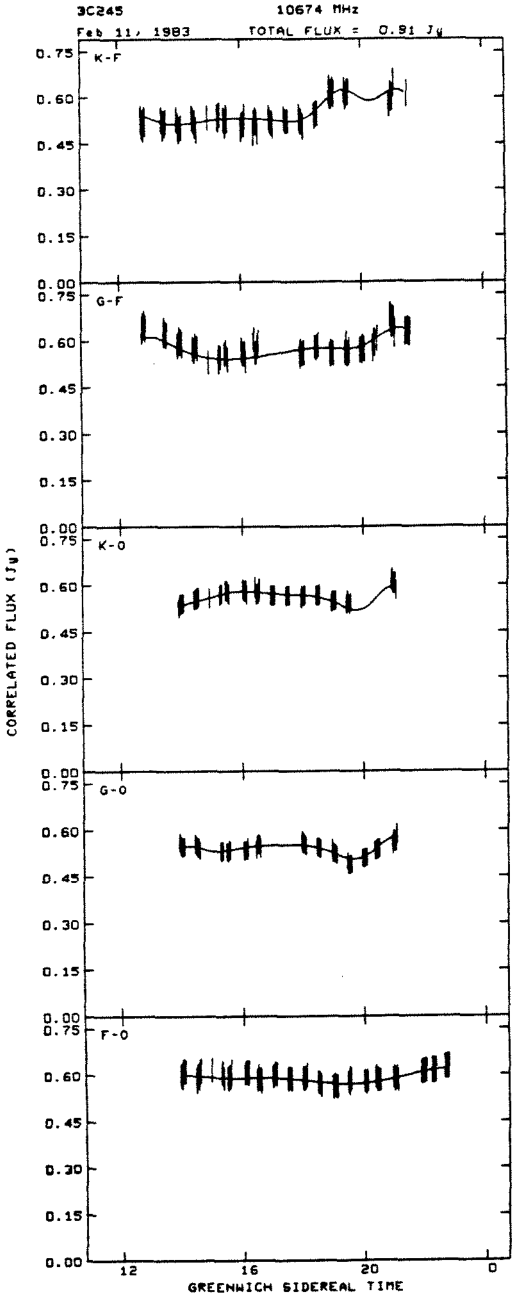

Figure 3a

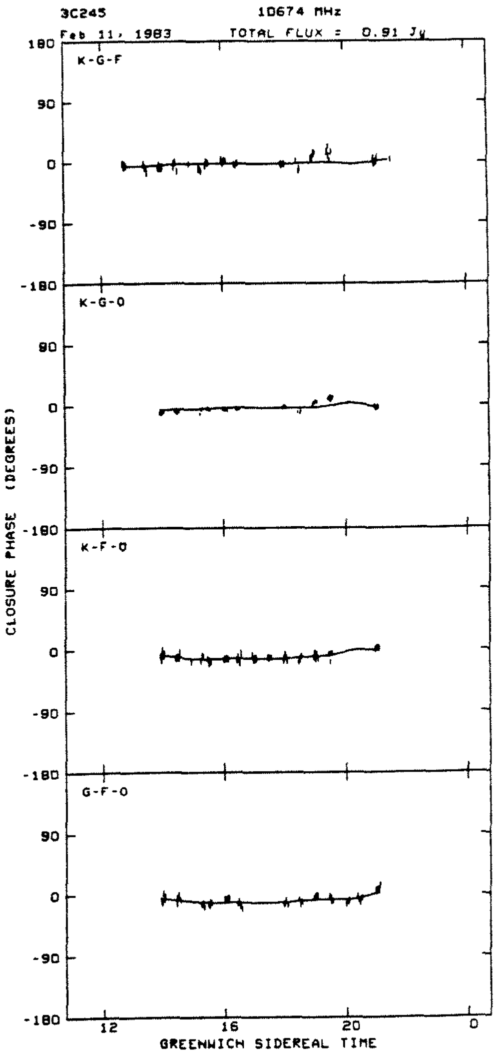

Figure 3b

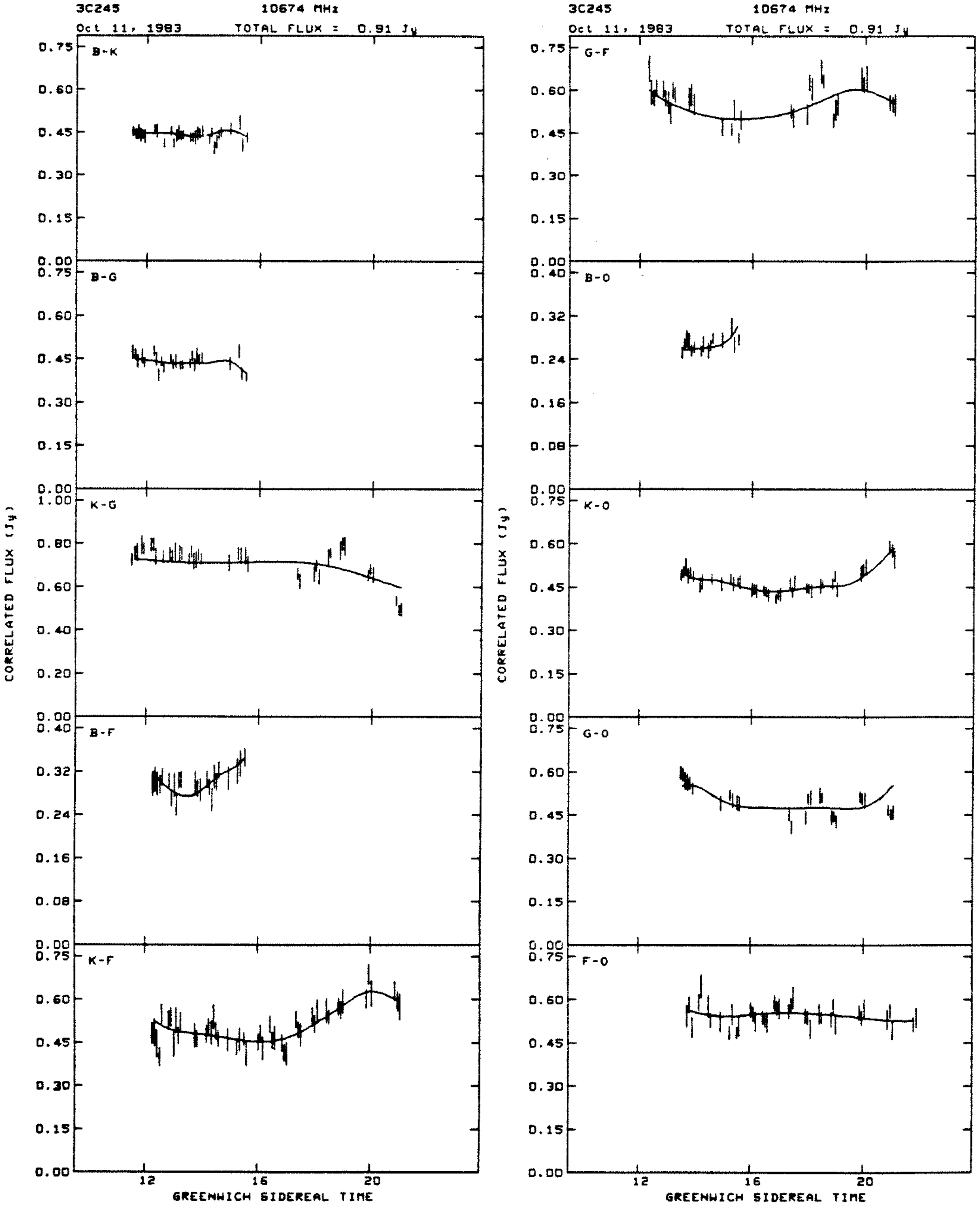
3C245
10674 MHz
Oct 11, 1983
TOTAL FLUX = 0.91 Jy
B-K
B-G
K-G
B-F
K-F
G-F
B-O
K-O
G-O
F-O
CORRELATED FLUX (Jy)
0.00
0.15
0.30
0.45
0.60
0.75
0.08
0.16
0.24
0.32
0.40
0.20
0.40
0.60
0.80
1.00
12
16
20
GREENWICH SIDEREAL TIME

Figure 4a

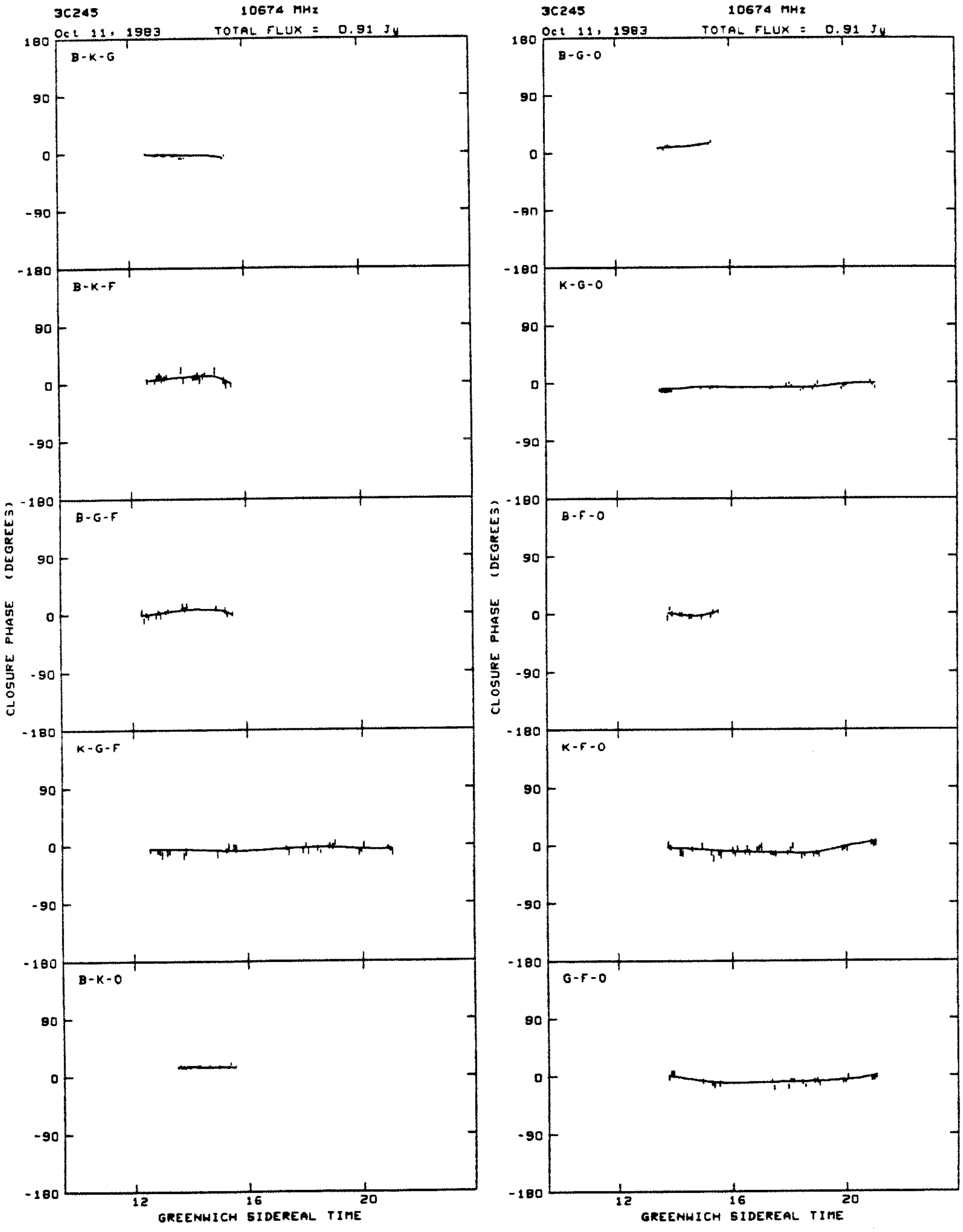
3C245
10674 MHz
Oct 11, 1983
TOTAL FLUX = 0.91 Jy
B-K-G
B-K-F
B-G-F
K-G-F
B-K-O
3C245
10674 MHz
Oct 11, 1983
TOTAL FLUX = 0.91 Jy
B-G-O
K-G-O
B-F-O
K-F-O
G-F-O
180
90
0
-90
-180
CLOSURE PHASE (DEGREES)
12
16
20
GREENWICH SIDEREAL TIME

Figure 4b

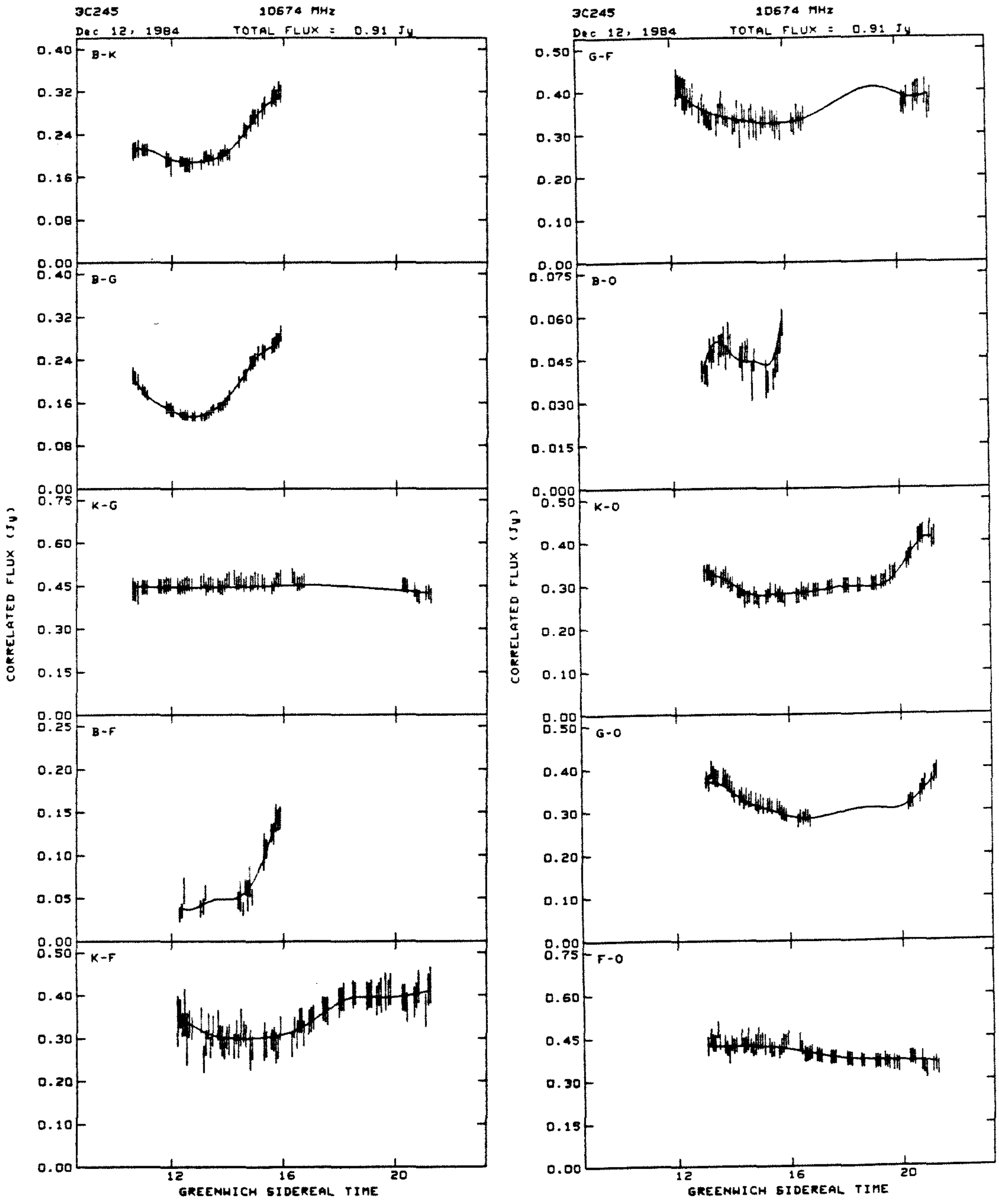
3C245
10674 MHz
Dec 12, 1984
TOTAL FLUX = 0.91 Jy
B-K
B-G
K-G
B-F
K-F
G-F
B-O
K-O
G-O
F-O
CORRELATED FLUX (Jy)
GREENWICH SIDEREAL TIME
12
16
20
0.00
0.08
0.16
0.24
0.32
0.40
0.15
0.30
0.45
0.60
0.75
0.05
0.10
0.20
0.25
0.50
0.015
0.030
0.045
0.060
0.075

Figure 5a

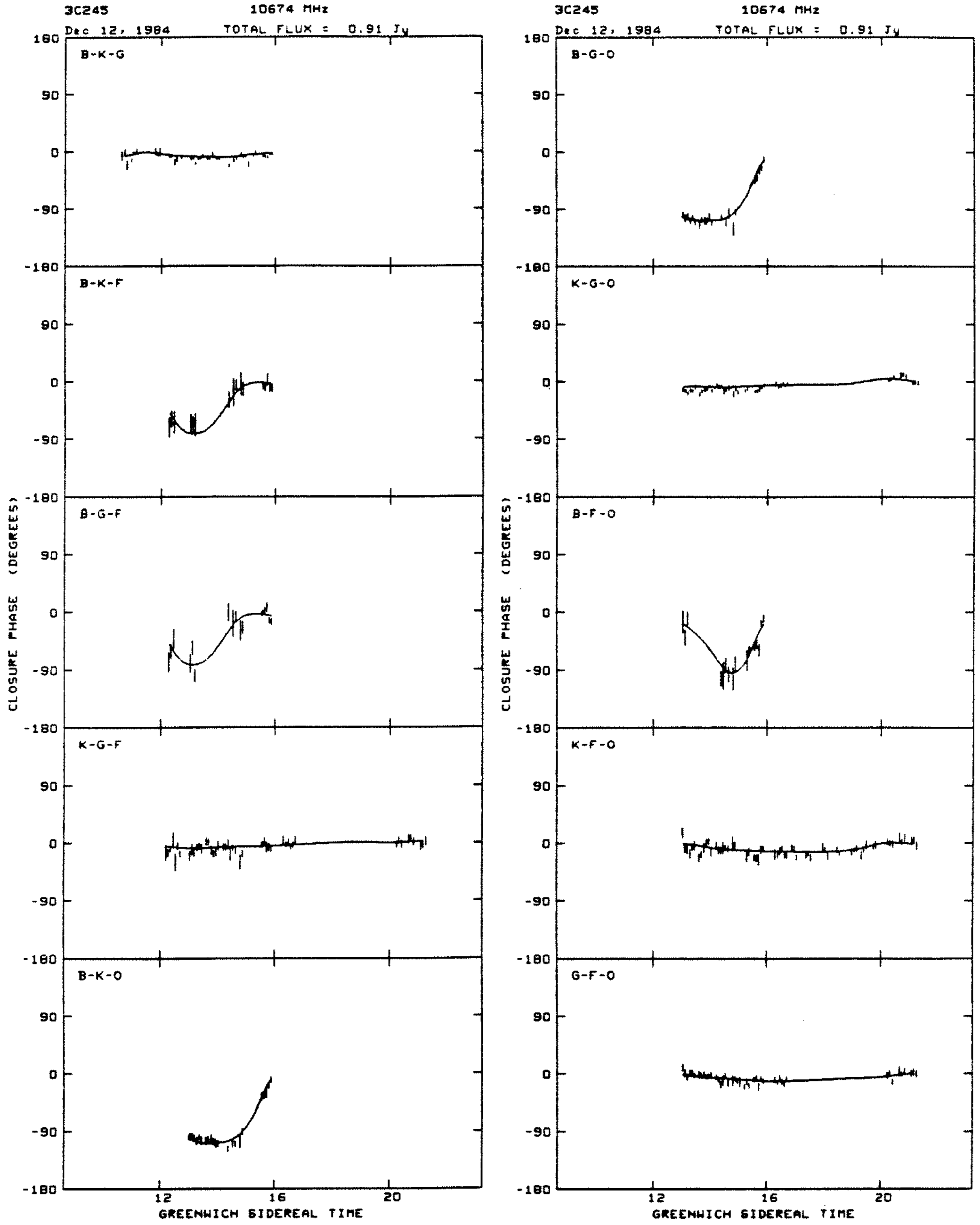
3C245
10674 MHz
Dec 12, 1984
TOTAL FLUX = 0.91 Jy
B-K-G
B-K-F
B-G-F
K-G-F
B-K-O
B-G-O
K-G-O
B-F-O
K-F-O
G-F-O
180
90
0
-90
-180
CLOSURE PHASE (DEGREES)
12
16
20
GREENWICH SIDEREAL TIME

Figure 5b

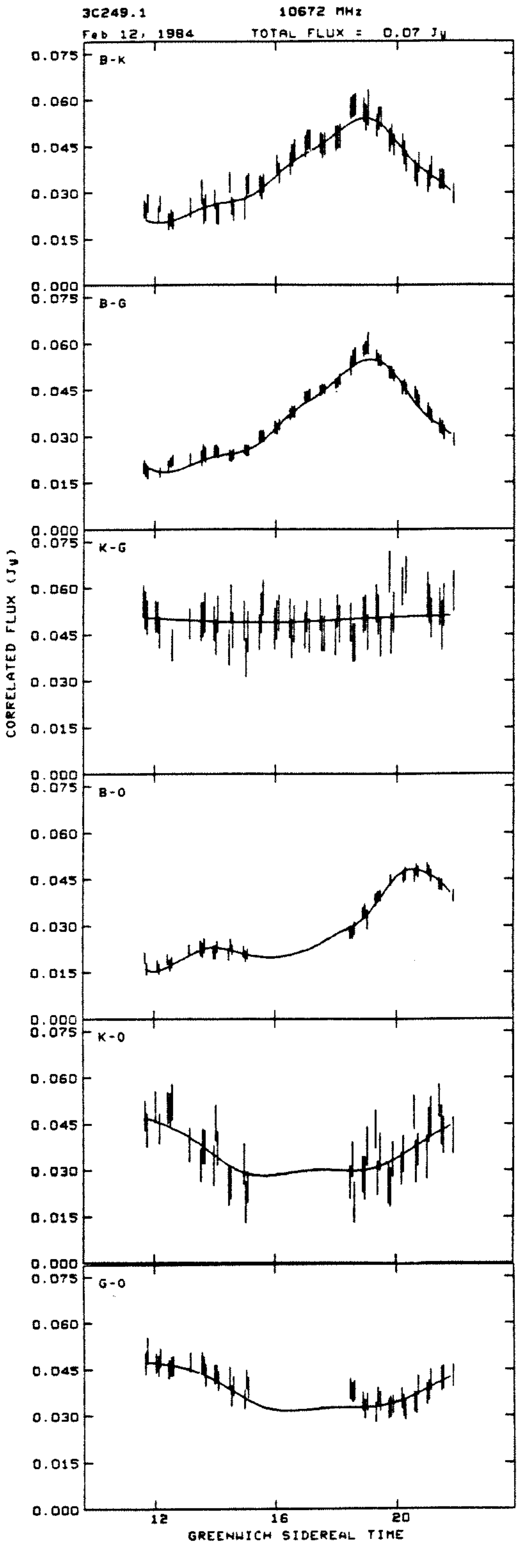

Figure 6a

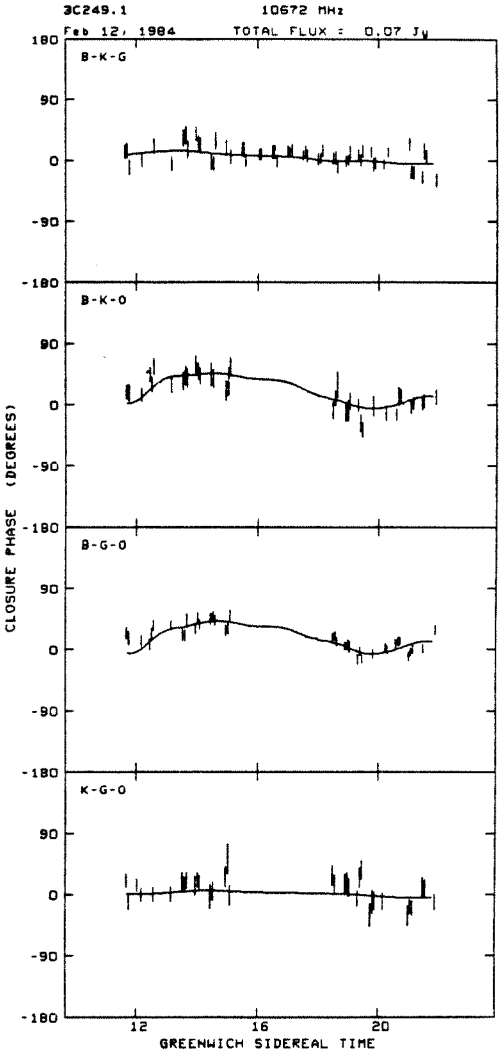

Figure 6b

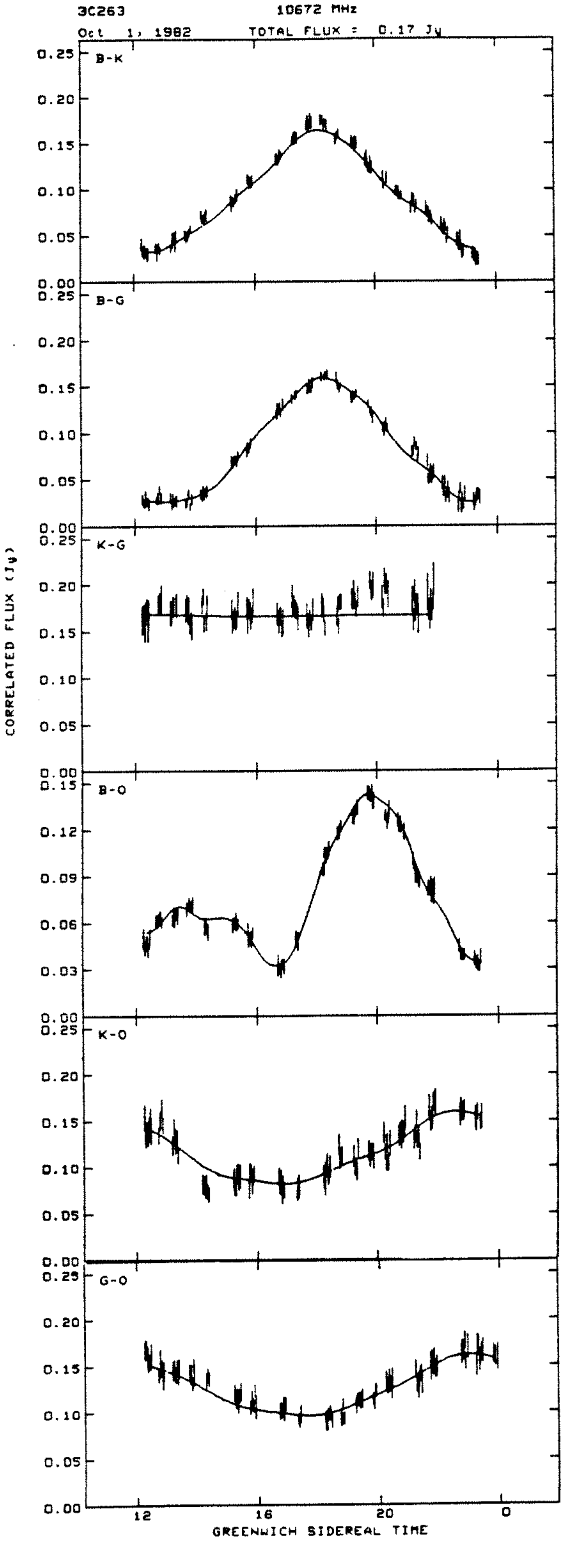

Figure 7a

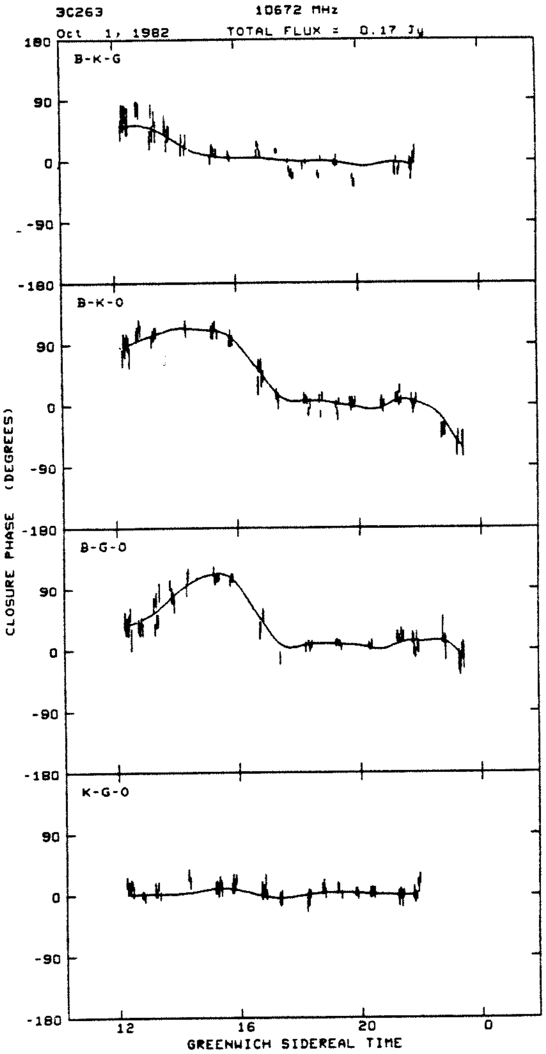

Figure 7b

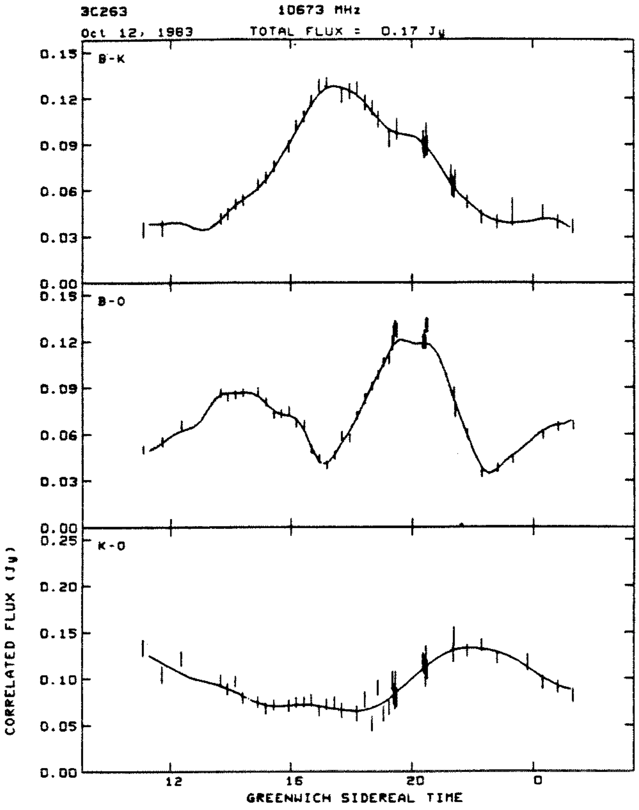

Figure 8a

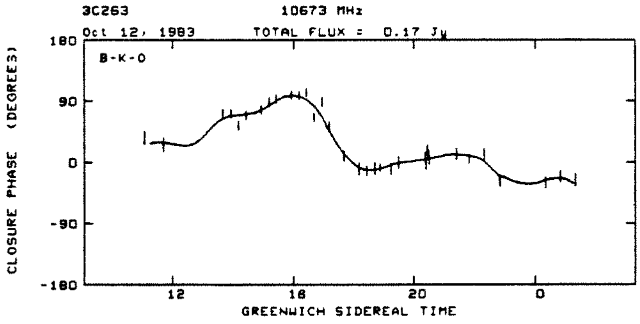

Figure 8b

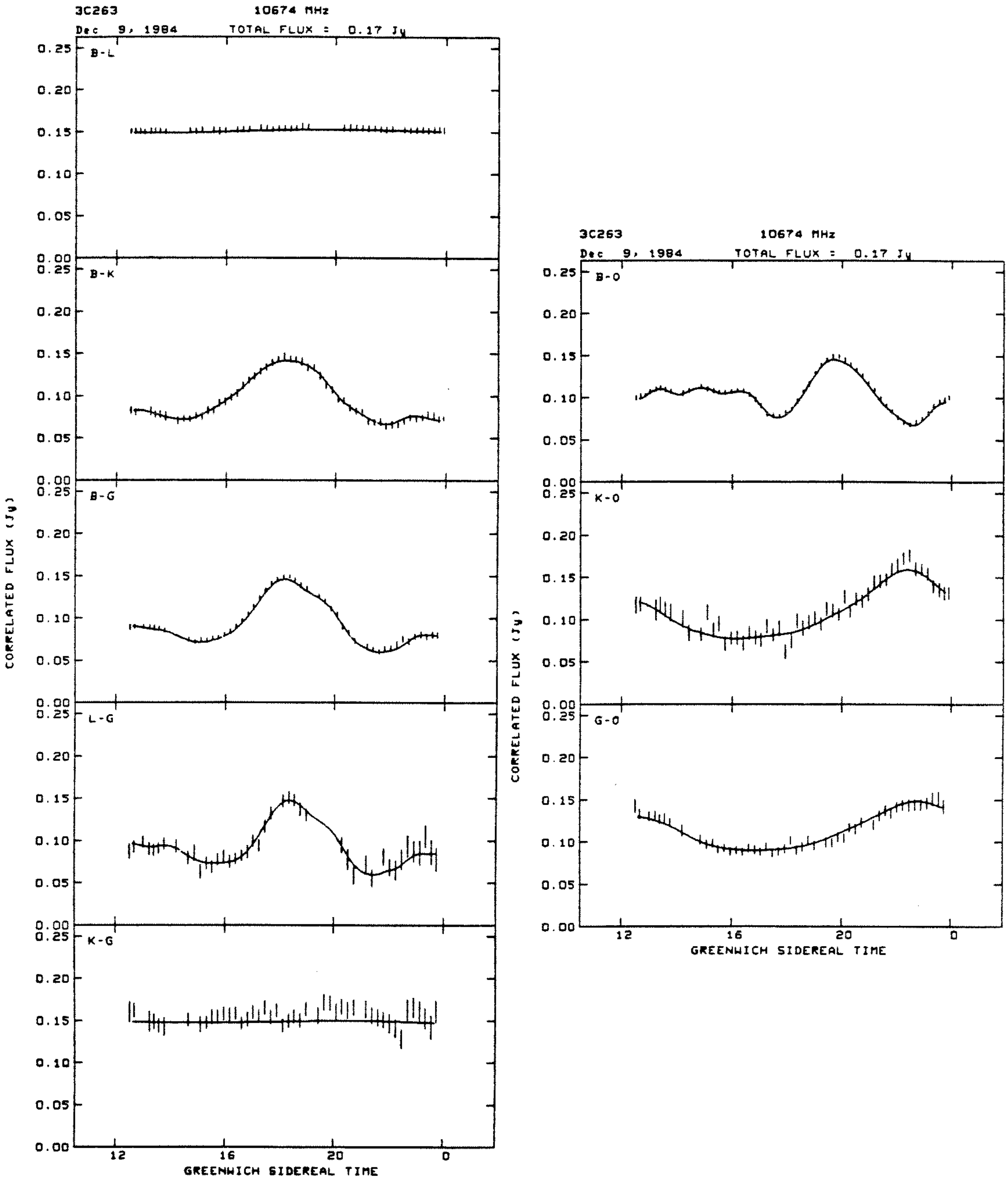
3C263
10674 MHz
Dec 9, 1984
TOTAL FLUX = 0.17 Jy
B-L
B-K
B-G
L-G
K-G
CORRELATED FLUX (Jy)
0.25
0.20
0.15
0.10
0.05
0.00
12
16
20
0
GREENWICH SIDEREAL TIME
3C263
10674 MHz
Dec 9, 1984
TOTAL FLUX = 0.17 Jy
B-O
K-O
G-O
CORRELATED FLUX (Jy)
GREENWICH SIDEREAL TIME

Figure 9a

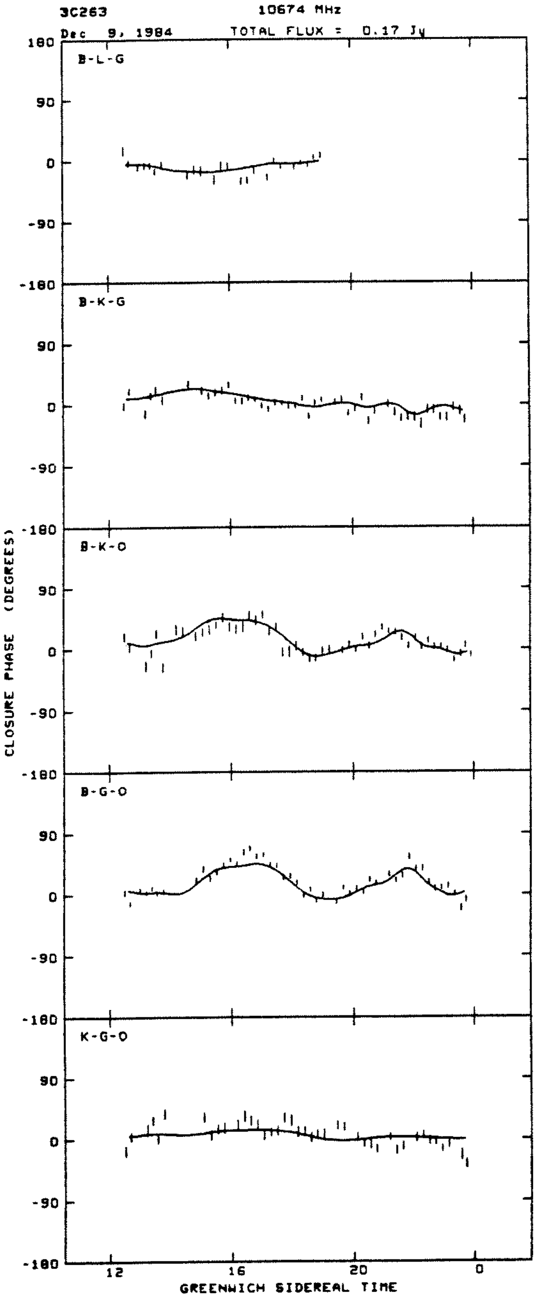
3C263
10674 MHz
Dec 9, 1984
TOTAL FLUX = 0.17 Jy
B-L-G
B-K-G
B-K-O
B-G-O
K-G-O
180
90
0
-90
-180
CLOSURE PHASE (DEGREES)
12
16
20
0
GREENWICH SIDEREAL TIME

Figure 9b

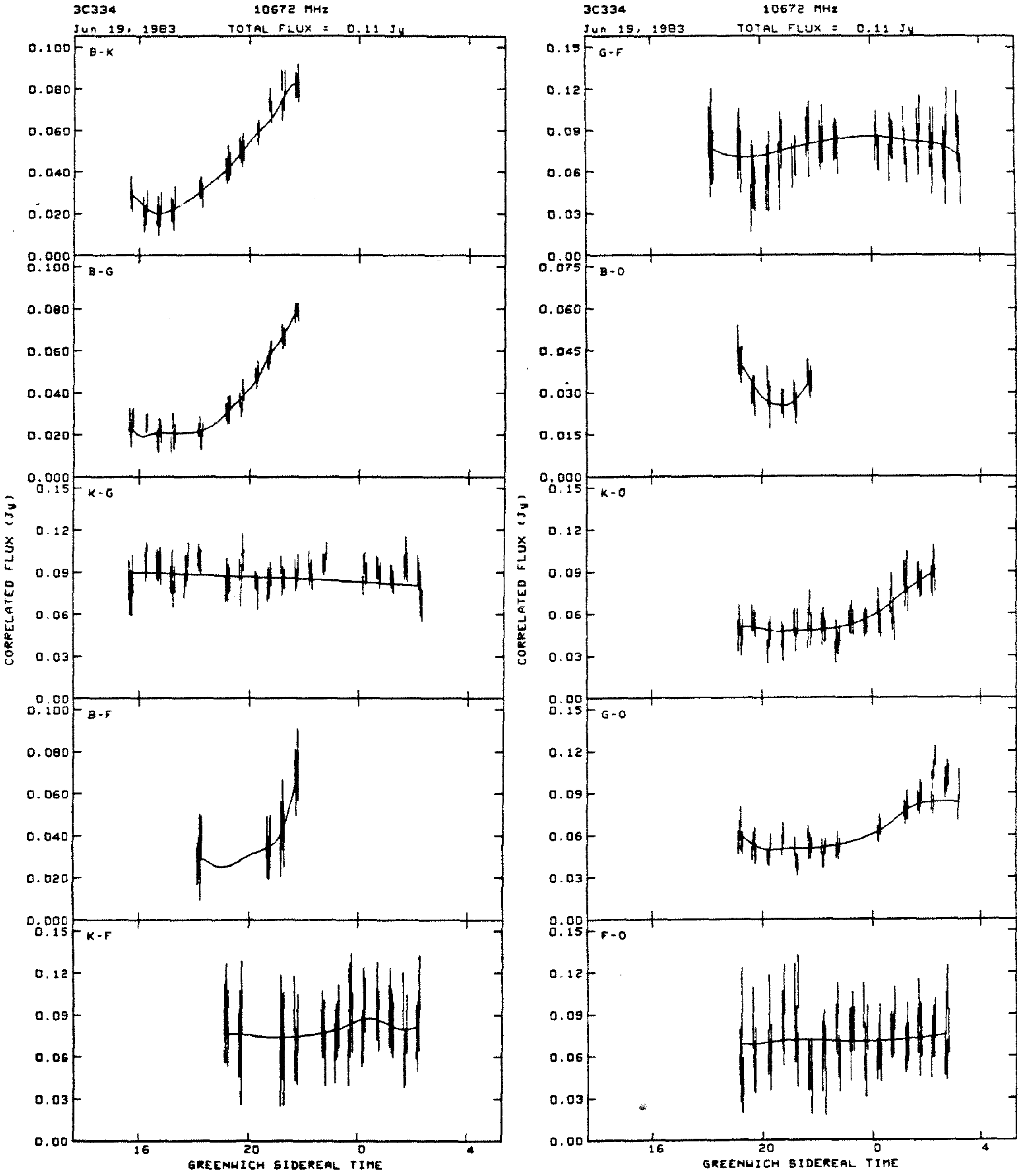
3C334
10672 MHz
Jun 19, 1983
TOTAL FLUX = 0.11 Jy
B-K
B-G
K-G
B-F
K-F
G-F
B-O
K-O
G-O
F-O
CORRELATED FLUX (Jy)
0.000
0.020
0.040
0.060
0.080
0.100
0.00
0.03
0.06
0.09
0.12
0.15
0.015
0.030
0.045
0.060
0.075
16
20
0
4
GREENWICH SIDEREAL TIME

Figure 10a

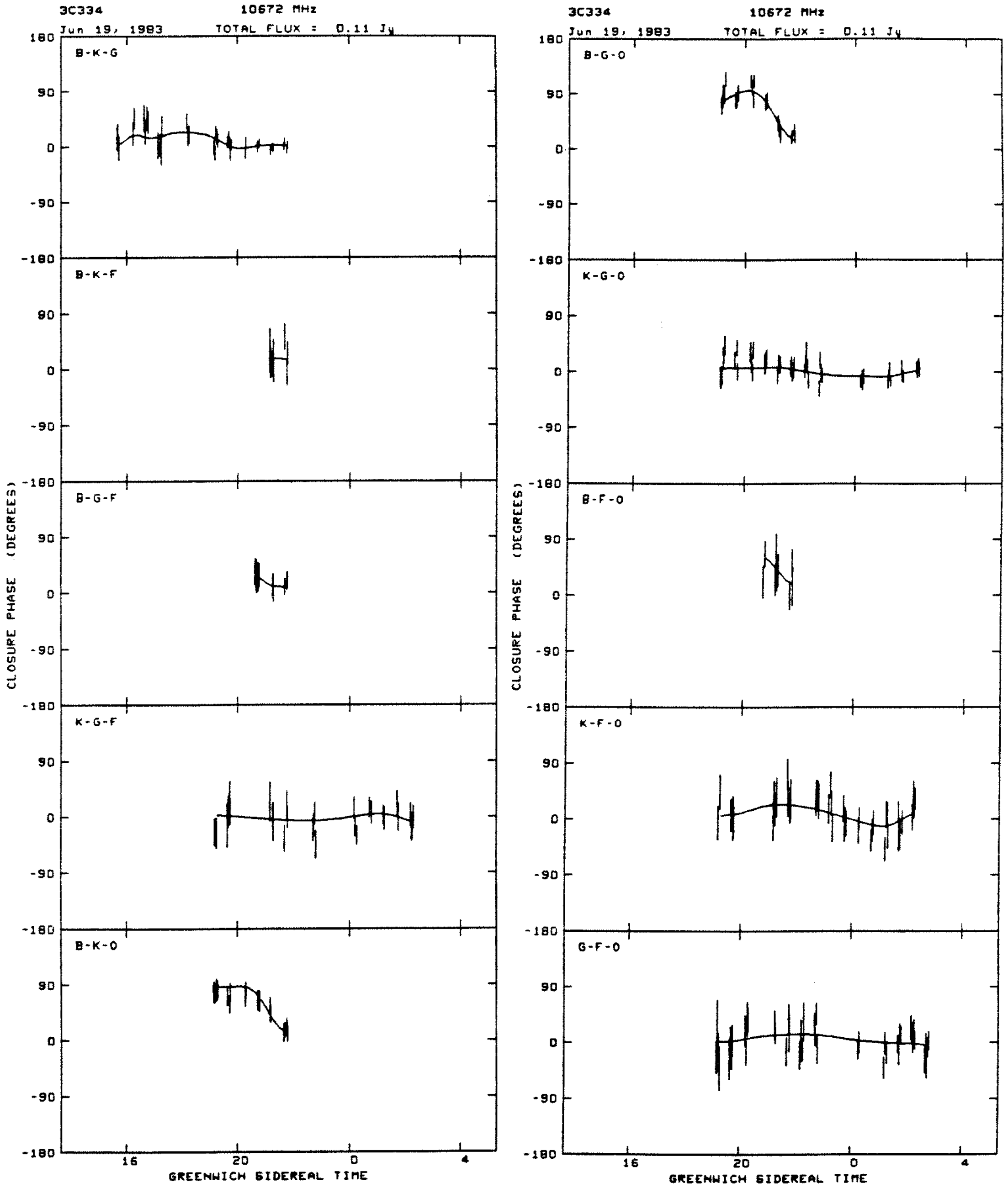
3C334
10672 MHz
Jun 19, 1983
TOTAL FLUX = 0.11 Jy
B-K-G
B-K-F
B-G-F
K-G-F
B-K-O
B-G-O
K-G-O
B-F-O
K-F-O
G-F-O
180
90
0
-90
-180
CLOSURE PHASE (DEGREES)
16
20
0
4
GREENWICH SIDEREAL TIME

Figure 10b